UNIVERSITY OF OKLAHOMA

GRADUATE COLLEGE

MICROWAVE AND SURFACE ELECTROMETRY WITH RYDBERG ATOMS

A DISSERTATION

SUBMITTED TO THE GRADUATE FACULTY

in partial fullfillment of the requirements for the

Degree of

DOCTOR OF PHILOSOPHY

By

JONATHON A. SEDLACEK
Norman, Oklahoma
2016

MICROWAVE AND SURFACE ELECTROMETRY WITH RYDBERG ATOMS

A DISSERTATION APPROVED FOR THE
HOMER L. DODGE DEPARTMENT OF PHYSICS AND ASTRONOMY

BY

Dr. James P. Shaffer, Chair

Dr. Alberto Marino Valle

Dr. Gregory Parker

Dr. Michael Santos

Dr. Rui Yang

Table of Contents

List of Tables

List of Figures

Abstract

Measurements of microwave electric fields in rubidium vapor cells, and of static electric fields near quartz with cold rubidium are presented. The measurements are performed using electromagnetically induced transparency (EIT) with Rydberg atoms. The theoretical basics of Rydberg atoms and EIT are discussed. An electric field perturbs the energy levels of Rydberg states, and Rydberg atom EIT is used to measure the perturbation. Experimental and theoretical results are presented, demonstrating the ability to measure the amplitude and polarization of microwave electric fields. These measurements are done using room temperature vapor cells, providing a pathway for portable atom based sensing of microwave electric fields. A second set of experiments is done with cold rubidium atoms in a magnetic trap near the (0001) surface of single crystal quartz. The experimental apparatus and lasers used in the experiments are described in detail. Electric fields due to Rb adsorbates on the surface are measured. The thermal desorption of Rb from the surface is characterized and theoretically analyzed using a Langmuir isobar. Blackbody ionization of Rydberg atoms produces electrons with low kinetic energy. The blackbody electrons bind to the surface and reduce the overall electric field. Electric fields as small as 30 mV/cm have been measured 20 μm from the surface. These results open up possibilities for using Rydberg atoms in hybrid quantum systems. Some of these possibilities are discussed.

Chapter 1

Introduction

This thesis describes measurements of static and microwave electric fields using Rydberg atoms. The chapter begins with an introduction to Rydberg atoms and electromagnetically induced transparency, the main tools used throughout the thesis. Then a general overview of atom based sensing and quantum hybrid systems are discussed in general as well as in the context of Rydberg atoms.

1.1 Rydberg Atoms

A common theme throughout this thesis and our lab is Rydberg atoms. Rydberg atoms have an electron in a highly excited electronic state. For example, in the following experiments, Rydberg atoms with principal quantum number n between 40 and 100 are used.

Due to the valence electron being loosely bound to the atom, Rydberg states have exaggerated properties compared to those of ground or low-lying states. In many Rydberg atom experiments, at least one of these exaggerated properties is exploited. A few of these properties include effective size, lifetimes and Rydberg-Rydberg interaction. In the following experiments, the properties of large transition dipole moments between states and high dc polarizability are used.

For ground state Rb atoms, optical frequencies are needed to drive electric

dipole transitions. However, as n increases, the spacing between adjacent energy levels decreases and transitions between Rydberg states can be driven with microwave fields, as illustrated in Fig. 1.1a. The wavefunctions for Rydberg states are long ranged, and there is tremendous overlap between wavefunctions of adjacent states, which leads to large transition dipole moments. With the Rydberg electron far away from the nucleus, the effect from the Coulomb potential is relatively small, allowing for the atom to become easily polarized in an external electric field. Compared to ground states, Rydberg states are much more sensitive to dc electric fields, as illustrated in Fig. 1.1b.

1.2 EIT

A main component of the following experiments is electromagnetically induced transparency (EIT) in an atomic medium. EIT is a quantum interference effect, where the absorption of one frequency of light can be canceled by the presence of a second frequency of light. Although EIT is a quantum effect [1], it can be explained using a classical analog with masses and springs [2, 3].

A two level atom can be described classically as a Lorentz oscillator [4]. The system is a harmonic oscillator, with the electron bound to the nucleus by a spring. The nucleus is assumed to have an infinite mass and the system has a resonance frequency, ω_0. An incident classical light field, $E_0 \cos(\omega t)$ drives the electron. When $\omega = \omega_0$ the system is driven into oscillation, which is the analog

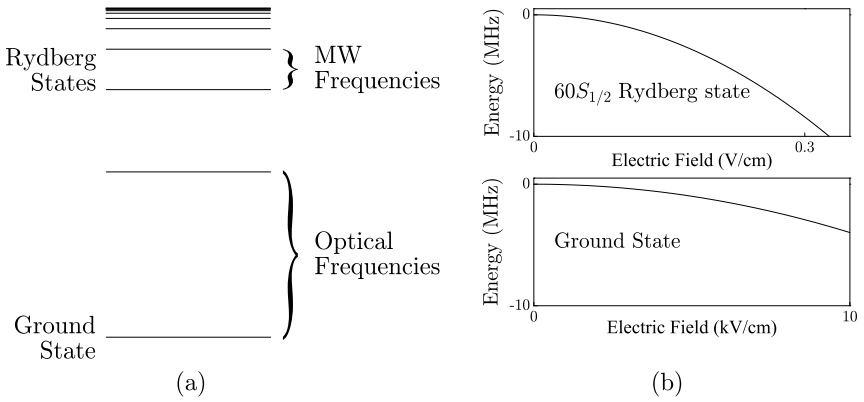

Figure 1.1: Illustration of the two properties of Rydberg atoms that are utilized in this work. (a) Electric dipole transitions between Rydberg states are in the microwave regime, while transitions between the ground state and low-lying states are in the optical regime. (b) The energy shifts as function of electric field (Stark shifts) are plotted for the $5S_{1/2}$ ground state and the $60S_{1/2}$ state. Unlike ground states, Rydberg states are extremely sensitive to external electric fields. The polarizability of the $5S_{1/2}$ ground state of Rb is $\sim 10^9$ times smaller than the polarizability of the $60S_{1/2}$ state.

of atomic absorption. The analogy can be extended to model a 3 level atom, with a system of three springs and two masses.

The addition of the second mass alters the frequency response of the system. At the resonance frequency of the two level system, the oscillations of the second mass can prevent the first mass from moving. The quantum analog is the addition of a second frequency of resonant light, which can prevent the absorption of the first frequency of light. EIT has been observed in many types of systems [1, 5].

1.3 Atom Based Sensing

Atom based sensors have had a tremendous impact across many areas of science and everyday life. Most notably atomics clocks, with applications of timing, GPS, and navigation. The main advantage of atom based sensors is repeatability. There is no known difference of properties between different atoms of the same species [6]. An illustration of this point, is that the definition of the second is based on one these properties, the spacing between energy levels of the ground state of cesium [6]. Combining the repeatability of atomic systems with narrow linewidth lasers and measurement techniques, leads to accurate and precise measurements.

Recently, many amazing results are being produced in the areas of atomic clocks and magnetometery. At the time of writing, atomic clocks have an uncertainty as low as 2×10^{-18} [7]. Magnetometers can reach sensitivities of 0.5 $\mathrm{fT/Hz^{1/2}}$ [8]. There are many other exciting areas in atomic sensing including atom interferometers [9], gyroscopes [10], and accelerometers. These devices do not always remain bulky laboratory equipment. Recently, atomic clocks and magnetometers have been miniaturized to the point that they can fit in the palm of your hand [11, 12]. Over the coming years more quantum devices are poised to make their way out of the laboratory, and into the field with many commercial applications [13, 14].

Most of these atoms based sensing methods use ground state atoms, however

atoms with an electron in a highly excited state, Rydberg atoms, can also be used. Although receiving much less attention, Rydberg atoms have been used as atomic sensors. Some of the first works in this area were done in the 1980's to measure dc electric fields in plasmas with spatial [15, 16] and vector resolution [17]. Recently attention has turned to measuring microwave electric fields with Rydberg atoms. Unlike ground state atoms, Rydberg atoms have electric dipole transitions in the microwave regime. Several experiments developing microwave measurement techniques in rubidium vapor cells will be described. A fourth level is added to Rydberg EIT, with the upper two levels being Rydberg states resonantly coupled together by microwaves.

1.4 Quantum Hybrid Systems

Another area of interest is using Rydberg atoms as dc electric field sensors in quantum hybrid systems. While the term quantum hybrid systems is not well defined, the basic idea in these systems is to combine traditionally disparate systems, and use the advantages of each system to achieve something not possible with each component. Many quantum hybrid systems have been proposed to achieve outstanding goals in quantum physics. Quantum hybrid systems designed for realizing advances in quantum information, communication, sensing, and computing have been proposed [18]. Due to the enormous number of possibilities and experimental complexities of combining multiple quantum

systems, experimental progress in this area has been slow. Some areas that have yielded encouraging results are atoms and ions [19], atom-membrane systems [20], and atom-photonic crystal waveguide systems [21].

Rydberg atoms are an attractive component to use in quantum hybrid systems due to having strong transitions in the microwave and millimeter regime, long lifetimes and coherence times [22]. For example, there is a proposal to use Rydberg atoms as a quantum memory in a hybrid system [23]. There have been a host of other theoretical proposals recently for utilizing Rydberg atoms near surfaces [24, 25, 26, 27, 28]. The experimental realization of these ideas has been hampered by uncertainties in characterizing interactions of atoms with surfaces, although some recent results are noteworthy [29, 30, 31].

To realize many of these Rydberg atom hybrid systems, a more complete understanding of surfaces is needed. One problem is the ionization of Rydberg atoms incident upon metal surfaces [32, 33]. Another major hurdle is the background electric fields caused by adsorbates [34, 35, 36, 37, 38, 39]. Rydberg states are sensitive to adsorbate electric fields because they are highly polarizable [40]. Adsorbate electric fields have caused problems in non-Rydberg atom experiments as well, including Casimir-Polder measurements [41], and surface ion traps [42].

The experiments in the second half of the thesis describe research aimed at establishing a better picture of atom-surface interactions, as well as constructing an apparatus capable of achieving some of these long-term goals for quantum

hybrid systems. In this thesis, the dc electric field near a Rb-quartz surface is investigated. Quartz was chosen as the surface because of its extensive use in the semiconductor and optics industries. The (0001) surface has been the subject of recent theoretical interest, partially due to its stability and low surface energy [43, 44, 45, 46, 47]. Despite numerous theoretical and experimental studies of bulk SiO_2 [48, 49, 50], the surface properties are not well understood.

1.5 Thesis Outline

This thesis describes experiments done in two different environments, vapor cells and an ultra high vacuum chamber. In Chapter 2, the theoretical principles used throughout are discussed. In Chapter 3, microwave measurements in rubidium vapor cells are detailed. Expanding of the theory in Chapter 2, Rydberg EIT in the context of resonant microwaves is discussed. Experimental data and theoretical calculations on the measurement of the amplitude and polarization of microwave fields are presented.

In the second part, experiments measuring electric fields near the surface of single crystal quartz using cold atoms is detailed. The experimental apparatus required in these experiments is more extensive than for the vapor cell experiments. Chapter 4 details the different pieces of the apparatus. The basics of the experimental techniques used in these experiments are outlined in Chapter 5. The method for trapping cold atoms and transporting them near the surface is

discussed. Absorption imaging, the main method of data acquisition is described. The results of these experiments are shown in Chapter 6. These results include the measurement of the activation energy of rubidium on a quartz surface, and the reduction of measured electric field in the presence of Rydberg atoms.

The details of several theoretical and experimental parts of the experiment are in the Appendices. Appendix A contains the details of the calculation of transition dipole moments, Stark shifts and Zeeman shifts of Rydberg atoms used throughout the thesis. The details of alignment of the home built bowtie cavity used for generating 480 nm are given in Appendix B.

Chapter 2

Theoretical Background

2.1 Rydberg Atoms

Atoms with an electron in a highly excited state are named Rydberg atoms. In this thesis, Rydberg atoms with principal quantum numbers n, in rubidium 87 (^{87}Rb) are studied. A pictorial representation of a Rydberg atom is shown in Fig. 2.1. The valence electron is in a highly excited state and loosely bound to the atom. At the center is a positively charged core containing the nucleus and electrons from the full inner shells.

2.1.1 Energies

Electronic states and energies of alkali Rydberg atoms such as Rb resemble those of hydrogen, but differ because of the interaction between the outer electron and the core electrons. The outer electron can penetrate into the inner cloud of the electrons, and can also polarize the core electrons. Far away from the nucleus, the outer electron experiences a Coulomb potential. When the electron is inside the ionic core the nuclear charge is no longer fully screened, and the potential is no longer a pure Coulomb one. The screening of the nuclear charge by the other electrons is different depending on the principal quantum number n, the orbital angular momentum, L, and total angular momentum J of the state.

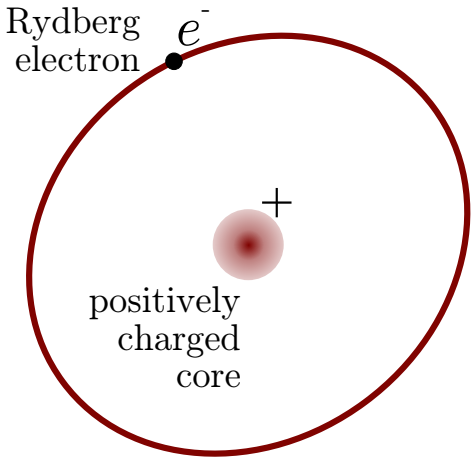

Figure 2.1: A simplified illustration of a Rb Ryberg atom. The highly excited Rydberg electron is bound to the atom, but orbits far away from the ionic core. The core contains the nucleus of the atom as well as the 36 electrons from the inner electron shells.

The energy levels of alkali Rydberg atoms are perturbed from those of hydrogen and are expressed as,

$$E = -\frac{1}{n^{*2}}, \tag{2.1}$$

where n^* is the effective principal quantum number. n^* is written as,

$$n^* = n - \delta_{nLJ}. \tag{2.2}$$

The quantity δ_{nLJ} is known as the quantum defect, and accounts for the difference in energies due to the presence of the ionic core. The quantum defects are derived from experimental measurements. Energy levels are measured experimentally, and fit to Eq. 2.1 with the expansion,

$$\delta_{nLJ} = \delta_0 + \frac{\delta_2}{(n-\delta_0)^2}. \tag{2.3}$$

Table 2.1: List of quantum defects for Rb used in this thesis.

State	Parameter	Value	Source
$nS_{1/2}$	δ_0	3.1311807	[51]
	δ_2	0.1787	[51]
$nP_{1/2}$	δ_0	2.6548849	[52]
	δ_2	0.2900	[52]
$nP_{3/2}$	δ_0	2.6416737	[52]
	δ_2	0.2950	[52]
$nD_{3/2}$	δ_0	1.3480948	[51]
	δ_2	-0.6054	[51]
$nD_{5/2}$	δ_0	1.3464622	[51]
	δ_2	-0.5940	[51]
$nF_{5/2}$	δ_0	0.0165192	[53]
	δ_2	-0.085	[53]
$nF_{7/2}$	δ_0	0.0165437	[53]
	δ_2	-0.086	[53]

The values for δ_0 and δ_2 used in this thesis are given in Table 2.1. To provide an example, the $53D_{5/2}$ state is used through this thesis, and its effective principal quantum number is, $n^* = 51.65$. In Rb, nF states are the highest L-states to exhibit core penetration [40]. The valence electron can still polarize the ionic core. However its effect on the energy levels is small, so for $L > 3$, the energies effectively become degenerate with those of hydrogen.

2.1.2 Wavefunctions

In order to carry out calculations of Rydberg atom properties and behavior, such as Stark shifts and transition dipole moments, the wavefunctions for Rydberg states are needed. Due to the similarities between Rydberg atoms and hydrogen,

the wavefunctions are calculated in a similar manner by solving the Schrödinger equation,

$$\left(-\frac{1}{2}\nabla^2 - V(r)\right)\psi(\mathbf{r}) = E\psi(\mathbf{r}). \tag{2.4}$$

$V(r)$ is a central potential. In the case of hydrogen, it is the Coulomb potential. The Schrödinger equation can be separated into radial and angular parts and solved independently, with solutions of radial and angular wavefunctions, $\psi(\mathbf{r}) = R_{n,L}(r)Y_{L,m}(\theta,\phi)$. By looking at different δ_{nLJ}, it is clear that electron core interaction mainly depends on L. This leads to using a modified L-dependent Coulomb potential, $V_{\text{eff}}(r,L)$ to model the interaction [54],

$$V_{\text{eff}}(r,L) = -2\left(\frac{Z_{\text{eff}}(r,L)}{r} + V_{\text{pol}}(r,L)\right), \tag{2.5}$$

with,

$$Z_{\text{eff}}(r,L) = 1 + (Z-1)e^{-ra_1(L)} - re^{-ra_2(L)}\left(a_3(L) + ra_4(L)\right), \tag{2.6}$$

and,

$$V_{\text{pol}}(r,L) = \frac{\alpha_c}{2}\frac{1 - e^{-(r/r_c(L))^6}}{r^4}. \tag{2.7}$$

The constants called $\alpha_1, \alpha_2, \alpha_3, \alpha_4$ in Eq. 2.6 and α_c and r_c in Eq. 2.7 for Rb are fit to reproduce experimentally measured energies [54], and their values are listed in Table 2.2. For $L = 1, 2$ (P and D states), spin-orbit interaction is taken into account following the approach of [55]. With the total potential $V_{\text{tot}}(r,L,J)$,

$$V_{\text{tot}}(r,L,J) = \begin{cases} V_{\text{eff}}(r,L) & \text{if } 0 \le r \le r_{\text{so}}(L), \\ V_{\text{eff}}(r,L) + V_{\text{so}}(r,L,J) & \text{if } r > r_{\text{so}}(L), \end{cases} \tag{2.8}$$

where $V_{\rm so}(r, L, J)$ is,

$$V_{\rm so}(r, L, J) = \alpha^2 \frac{1}{r} \frac{\partial V_{\rm eff}(r, L)}{\partial r} \frac{J(J+1) - L(L+1) - \frac{3}{4}}{2}, \tag{2.9}$$

where α is the fine-structure constant. Since $V_{\rm so}$ does not accurately describe the motion of the outer electron near the inner core, a cut-off radius $r_{\rm so}(L)$ is introduced. The values for $r_{\rm so}(L)$ are chosen to reproduce the experimentally measured fine structure splittings, and are listed in Table 2.2.

Using this potential, the radial Schrödinger equation is solved using a Fortran program called `RADIAL` [56]. The program uses a power series expansion to numerically approximate a solution to the radial Schrödinger equation. The calculated radial wavefunctions, $R_{n,L}(r)$ are used for calculating transition dipole moments and Stark shifts of Rydberg states. Just as the quantum defects vanish for $L > 3$, $V_{\rm eff}(r, L)$ also approaches a Coulomb potential because the electron orbits at large r and does not penetrate the inner core. For $L > 3$, $R_{n,L}(r)$ for hydrogenic states are used.

The inner electron shells are completely filled and do not contribute to the angular momentum of the atom, so alkali atoms and hydrogen both have spin $S = 1/2$. Since all of the interaction of the outer electron with the inner core was accounted for in the central potential, the solutions of $Y_{L,m}$ remain unchanged. In calculations, the solutions of $Y_{L,m}$ for the hydrogen atom are used.

Table 2.2: List of constants used for calculating the Rydberg atom wavefunctions.

L	0	1	2	3
a_1	3.69628474	4.44088978	3.78717363	2.39848933
a_2	1.64915255	1.92828831	1.57027864	1.76810544
a_3	-9.86069196	-16.79597770	-11.65588970	-12.07106780
a_4	0.19579987	-0.81633314	0.52942835	0.77256589
r_c	1.66242117	1.50195124	4.86851938	4.79831327
r_{so}	-	0.0442825	0.2495720	-
$\alpha_c = 9.0760$				

2.1.3 Lifetimes and Blackbody Radiation

The lifetimes of Rydberg states are relatively long compared to those of low-lying excited states. For example, the lifetime of the $5P_{3/2}$ state is 26 ns [57], while the lifetimes for Rb Rydberg atoms with $n \sim 40 - 80$ range from $40 - 250\,\mu$s [58].

While the lifetime of low-lying states is primarily due to spontaneous emission, the lifetimes of Rydberg atoms are strongly affected by blackbody radiation. There is a large frequency overlap of the blackbody spectrum at room temperature, and transitions between Rydberg states. The largest effect is coupling to, and driving transitions to nearby energy levels, reducing the lifetimes of Rydberg states from the values of their radiative lifetimes.

Besides driving transitions to nearby energy levels, Rydberg atoms can also be ionized due to blackbody radiation [59]. There are two types of ionization that can occur, direct and indirect ionization. The direct process occurs when a Rydberg atom absorbs a single blackbody photon, and the electron is excited to the continuum. An indirect process is the result of the absorption of several

blackbody photons. Ionization occurs in a stepwise fashion. At 300 K, the direct process accounts for $\sim 99\%$ of the ionization, thus the indirect processes are ignored in this thesis.

The combination of these effects contribute to the effective lifetime of Rydberg states. The total decay rate (1/lifetime), Γ_{TOT} is broken up into three parts,

$$\Gamma_{\mathrm{TOT}} = \Gamma_0 + \Gamma_{\mathrm{BBT}} + \Gamma_{\mathrm{BBI}}, \tag{2.10}$$

with Γ_0, the radiative decay rate, Γ_{BBT}, the decay rate from blackbody transitions, and Γ_{BBI}, the decay rate due to direct blackbody ionization. Although the underlying calculations are involved, the three different decay rates can be described with semi-empirical equations [58, 59],

$$\Gamma_0 = \frac{1}{\tau_s n^{*\delta}} \tag{2.11a}$$

$$\Gamma_{\mathrm{BBT}} = \frac{A}{n^{*D}} \frac{2.14 \times 10^{10}}{\exp(315780B/n^{*C}T) - 1} \tag{2.11b}$$

$$\Gamma_{\mathrm{BBI}} = C_L T \left(\frac{14423}{n^{*7/3}} + \frac{10770L^2}{n^{*11/3}} \right) \times \log \left(\frac{1}{1 - \exp\left(-\frac{157890}{Tn^{*2}}\right)} \right). \tag{2.11c}$$

The constants C_L, A, B, C, D, τ_s and δ are listed in Table 2.3, n^* is the effective quantum number as defined in Eq. 2.2 and T is the temperature of the surrounding environment.

2.1.4 Scaling Laws

Many properties of Rydberg atoms have straightforward scaling as n is increased, and scaling laws can be derived. Some of the properties are listed in Table 2.4.

Table 2.3: List of constants for calculating the decay rates of Rb Rydberg states. The constants are taken from [58, 59]

	S	P		D	
C_L	0.2	0.15		0.3	
A	0.134	0.053		0.033	
B	0.251	0.128		0.084	
C	2.567	2.183		1.912	
D	4.426	3.989		3.716	
	$S_{1/2}$	$P_{1/2}$	$P_{3/2}$	$D_{3/2}$	$D_{5/2}$
τ_s	1.368	2.4360	2.5341	1.0761	1.0687
δ	3.0008	2.9989	3.0019	2.9898	2.9897

These scaling laws are important for several reasons. First, the differences from ground state atoms can easily be seen. For example, the effective radius scales $\sim n^2$, demonstrating the large spatial extent of Rydberg atoms. Another benefit of the scalings is that they aid in choosing a suitable Rydberg state for a given experiment, without the need run exact calculations for every state. For example, if the polarizability or the Stark shift of the $60S_{1/2}$ state is known (Fig. 1.1b), the shift for other S states can be obtained by multiplying the y-axis in Fig. 1.1b, or α, by $(n'/60)^7$. The scaling laws also help to identify tradeoffs that are made when changing n. For example, in an experiment involving interactions between Rydberg atoms, choosing an extremely high n state might seem advantageous. However, high n states are more sensitive to background dc electric fields ($\alpha \sim n^7$) and the coupling strength for exciting atoms into these states decreases ($\langle 5P_{3/2}|er|nL'\rangle \sim n^{-3/2}$).

Table 2.4: List of scaling laws for alkali Rydberg atoms.

Quantity	Symbol	Scaling	Ref.
Radius	$\langle r \rangle$	n^2	[40]
Transition Dipole	$\langle nL \vert er \vert nL' \rangle$	n^2	[40]
Rydberg Excitation Dipole	$\langle 5P_{3/2} \vert er \vert nL' \rangle$	$n^{-3/2}$	[60]
Binding Energy	E_b	n^{-2}	[40]
Polarizability	α	n^7	[40]
Dipole - Dipole Interaction	C_3	n^4	[61]
van der Waals Interaction	C_6	n^{11}	[61]
Radiative Lifetimes (low-L)	τ	n^3	[40]

2.2 Rydberg EIT

Since the first observation in 2007 [62], Rydberg atom electromagnetically induced transparency (EIT) has been used to investigate Rydberg-Rydberg interactions [63], optical nonlinearities [64] and measure quantum defects [51]. In this thesis, Rydberg EIT is used to measure the amplitudes of static (dc) electric fields and resonant microwave (MW) fields. As introduced in Section 1.2, EIT is a quantum phenomena, where a medium, in this case an atomic medium, can be made transparent for a certain frequency of light, by using a second frequency of light. Rydberg EIT is done in a ladder system as shown in Fig. 2.2, with the top of the ladder being a Rydberg state. Three atomic states are coupled together by two lasers. In the figure, the ground state, $|1\rangle$, $5S_{1/2}$ is coupled to the intermediate $5P_{3/2}$ state, $|2\rangle$, with a laser at 780 nm, referred to as the probe laser. The third state, $|3\rangle$, in the system is a Rydberg state. The intermediate state and the Rydberg state are coupled together by a laser ~ 480 nm, named

the coupling laser. When the coupling laser is on resonance with states $|2\rangle$ and $|3\rangle$, the atom no longer absorbs light on the probe transition. This is illustrated in Fig. 2.3a and b. First, considering only the probe laser in a two level system, the absorption profile as the frequency of the probe laser is swept across resonance is shown in Fig. 2.3a. The result is an absorption dip with a Lorentzian profile, and a full width at half maximum (FWHM) that is equal to the rate of spontaneous emission of the $5P_{3/2}$. Adding the resonant coupling laser into the system modifies the absorption spectrum as shown in Fig. 2.3b. The appearance of the narrow transmission window near probe resonance is the hallmark of EIT.

2.2.1 Hamiltonian

In order to theoretically describe the system, the Hamiltonian of the system shown in Fig. 2.2 is constructed. The Hamiltonian of the atom-light system is

$$H = H_a + H_E, \tag{2.12}$$

where H_a is the atomic Hamiltonian in the absence of any external fields,

$$H_a = 0|1\rangle\langle 1| + \hbar\omega_2|2\rangle\langle 2| + \hbar\omega_3|3\rangle\langle 3|, \tag{2.13}$$

and H_E is the electric dipole Hamiltonian, accounting for the atom-light interaction. $H_E = -e\vec{r}\cdot\vec{E}$, where e is the magnitude of the electron charge, and $\vec{E}$ is the external electric field. This is a semiclassical treatment, where atoms are treated quantum mechanically, but the electric field of the incident radiation is

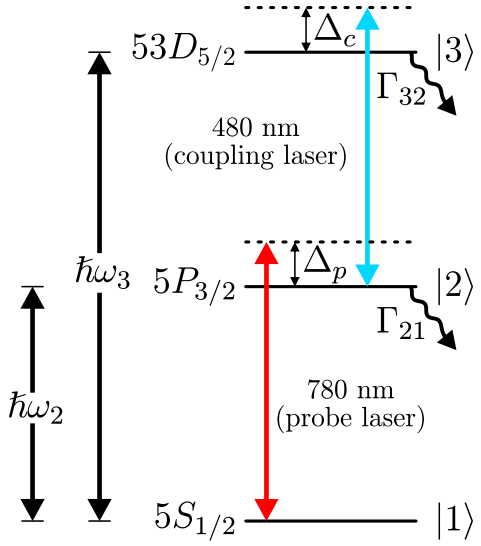

Figure 2.2: Diagram of the energy levels used in the 3 level EIT ladder system. Relative to state $|1\rangle$, the energies of states $|2\rangle$ and $|3\rangle$ are $\hbar\omega_2$ and $\hbar\omega_3$ respectively. The Δ's are the detunings of the lasers from the atomic transitions. Radiative decay from each excited states is represented by Γ.

considered classically. Classically an electric field oscillating at angular frequency ω is written as,

$$\vec{E}(\omega,t) = \vec{E_0}\cos(\omega t) = \frac{E_0}{2}\left(\hat{\epsilon}e^{-i\omega t} + \hat{\epsilon}^* e^{i\omega t}\right), \tag{2.14}$$

where E_0 is the amplitude of the field, and $\hat{\epsilon}$ are spherical unit vectors. The external light field is composed of light at the probe and coupling frequencies,

$$\begin{aligned}\vec{E}_{\text{tot}}(t) &= \vec{E}(\omega_p,t) + \vec{E}(\omega_c,t) \\ &= \frac{E_p}{2}\left(\hat{\epsilon}_p e^{-i\omega_p t} + \hat{\epsilon}_p^* e^{i\omega_p t}\right) + \frac{E_c}{2}\left(\hat{\epsilon}_c e^{-i\omega_c t} + \hat{\epsilon}_c^* e^{i\omega_c t}\right).\end{aligned} \tag{2.15}$$

The total Hamiltonian can be constructed in matrix form using Eq. 2.12, 2.13, and 2.15,

$$H = \frac{\hbar}{2}\begin{pmatrix} 0 & \left(\Omega_p^* e^{i\omega_p t} + \Omega_p e^{-i\omega_p t}\right) & 0 \\ \left(\Omega_p^* e^{i\omega_p t} + \Omega_p e^{-i\omega_p t}\right) & 2\omega_2 & \left(\Omega_c^* e^{i\omega_c t} + \Omega_c e^{-i\omega_c t}\right) \\ 0 & \left(\Omega_c^* e^{i\omega_c t} + \Omega_c e^{-i\omega_c t}\right) & 2\omega_3 \end{pmatrix}. \tag{2.16}$$

In this notation the Rabi frequencies, Ω_i, are defined as,

$$\begin{aligned} \Omega_p &= \frac{E_p}{\hbar}\langle 2|\hat{\epsilon}_p \cdot e\mathbf{r}|1\rangle &&= \frac{E_p}{\hbar}\langle 1|\hat{\epsilon}_p^* \cdot e\mathbf{r}|2\rangle^* \\ \Omega_p^* &= \frac{E_p}{\hbar}\langle 2|\hat{\epsilon}_p \cdot e\mathbf{r}|1\rangle^* &&= \frac{E_p}{\hbar}\langle 1|\hat{\epsilon}_p^* \cdot e\mathbf{r}|2\rangle \\ \Omega_c &= \frac{E_c}{\hbar}\langle 3|\hat{\epsilon}_c \cdot e\mathbf{r}|2\rangle &&= \frac{E_c}{\hbar}\langle 2|\hat{\epsilon}_c^* \cdot e\mathbf{r}|3\rangle^* \\ \Omega_c^* &= \frac{E_c}{\hbar}\langle 3|\hat{\epsilon}_c \cdot e\mathbf{r}|2\rangle^* &&= \frac{E_c}{\hbar}\langle 2|\hat{\epsilon}_c^* \cdot e\mathbf{r}|3\rangle \end{aligned} \tag{2.17}$$

The quantities $\mu_{jk} = \langle j|\hat{\epsilon} \cdot \mathbf{r}|k\rangle$ are transition dipole moments between states $|k\rangle$ and $|j\rangle$, and are a measure of transition strength. The details necessary to calculate the transition dipole moments are found in Appendix A.

To make the calculations more tractable the time dependence of the Hamiltonian can be removed. The basis states can be rotated by a time dependent unitary transformation,

$$|\psi_{\text{new}}(t)\rangle = U(t)|\psi(t)\rangle. \tag{2.18}$$

such that the new Hamiltonian will be time independent. The basis states will be rotated through a unitary transformation to a reference frame that is co-rotating with the applied electric fields,

$$U(t) = \begin{pmatrix} 1 & 0 & 0 \\ 0 & e^{-i\omega_p t} & 0 \\ 0 & 0 & e^{-i(\omega_p+\omega_c)t} \end{pmatrix}. \tag{2.19}$$

For any time dependent unitary transformation the new Hamiltonian is [65],

$$H_{\text{new}} = i\hbar \frac{\mathrm{d}U^\dagger}{\mathrm{d}t} U + U^\dagger H U \tag{2.20}$$

Combining Eq. 2.16, 2.19, and 2.20 the Hamiltonian in the new reference frame becomes,

$$H_{\text{new}} = \frac{\hbar}{2} \begin{pmatrix} 0 & \left(\Omega_p^* + \Omega_p e^{-2i\omega_p t}\right) & 0 \\ \left(\Omega_p + \Omega_p^* e^{2i\omega_p t}\right) & -2\Delta_p & \left(\Omega_c^* + \Omega_c e^{-2i\omega_c t}\right) \\ 0 & \left(\Omega_c + \Omega_c^* e^{2i\omega_c t}\right) & -2(\Delta_p + \Delta_c) \end{pmatrix}. \tag{2.21}$$

The quantities $\Delta_{p,c}$ are the detunings of the probe and coupling laser from resonance,

$$\begin{aligned} \Delta_p &= \omega_p - \omega_2 \\ \Delta_c &= \omega_c - (\omega_3 - \omega_2) \end{aligned} \tag{2.22}$$

By applying the rotating wave approximation the Hamiltonian can be made time independent. In the rotating wave approximation the terms that oscillate at twice the frequency of the electric field are neglected. This approximation is valid when $\Omega \ll \omega$ [65]. The final Hamiltonian is,

$$H' = \frac{\hbar}{2} \begin{pmatrix} 0 & \Omega_p^* & 0 \\ \Omega_p & -2\Delta_p & \Omega_c^* \\ 0 & \Omega_c & -2(\Delta_p + \Delta_c) \end{pmatrix}. \tag{2.23}$$

2.2.2 Theoretical Results

Using the time independent Hamiltonian, the time independent Schrödinger equation can be solved to obtain the new states and energies. To see the origin of EIT, it is instructive to look at the new eigenstates when the detunings of

both lasers are 0 ($\Delta_p = \Delta_c = 0$),

$$\begin{aligned} |1'\rangle &= -\Omega_c^*|1\rangle + \Omega_p|3\rangle \\ |2'\rangle &= \Omega_p^*|1\rangle - \sqrt{|\Omega_p|^2 + |\Omega_c|^2}|2\rangle + \Omega_c|3\rangle \\ |3'\rangle &= \Omega_p^*|1\rangle + \sqrt{|\Omega_p|^2 + |\Omega_c|^2}|2\rangle + \Omega_c|3\rangle. \end{aligned} \tag{2.24}$$

States $|2'\rangle$ and $|3'\rangle$ have components of all three bare atomic states. However, $|1'\rangle$ does not have a component of state $|2\rangle$. Since the lasers couple states $|1\rangle$ and $|3\rangle$ to state $|2\rangle$, atoms in state $|1'\rangle$ do not interact with the optical fields. $|1'\rangle$ is called a *dark state*. Atoms in a dark state are transparent to the optical fields. This dark state is present in the three level system with two optical fields present, however if the coupling field is not present there is no dark state. The presence of the coupling field renders the medium transparent to the probe field, this is the reasoning behind the moniker *electromagnetically induced transparency*.

Another instructive case to consider is the weak probe regime, $|\Omega_p| \ll |\Omega_c|$. In this situation the effect of the probe laser on the system can be neglected, $\Omega_p = 0$. Diagonalizing the Hamiltonian yields the eigenenergies,

$$\begin{aligned} E_1' &= 0 \\ E_2' &= -\hbar\Delta_p - \frac{\hbar|\Omega_c|}{2} \\ E_3' &= -\hbar\Delta_p + \frac{\hbar|\Omega_c|}{2}. \end{aligned} \tag{2.25}$$

The energy of $|1'\rangle$ remains unchanged from the energy of $|1\rangle$ in the uncoupled basis. However, the energies of states $|2'\rangle$ and $|3'\rangle$ are shifted $\pm\frac{\hbar}{2}|\Omega_c|$ from the uncoupled energy of $|2\rangle$. This is illustrated in Fig. 2.4. In the diagonalized basis,

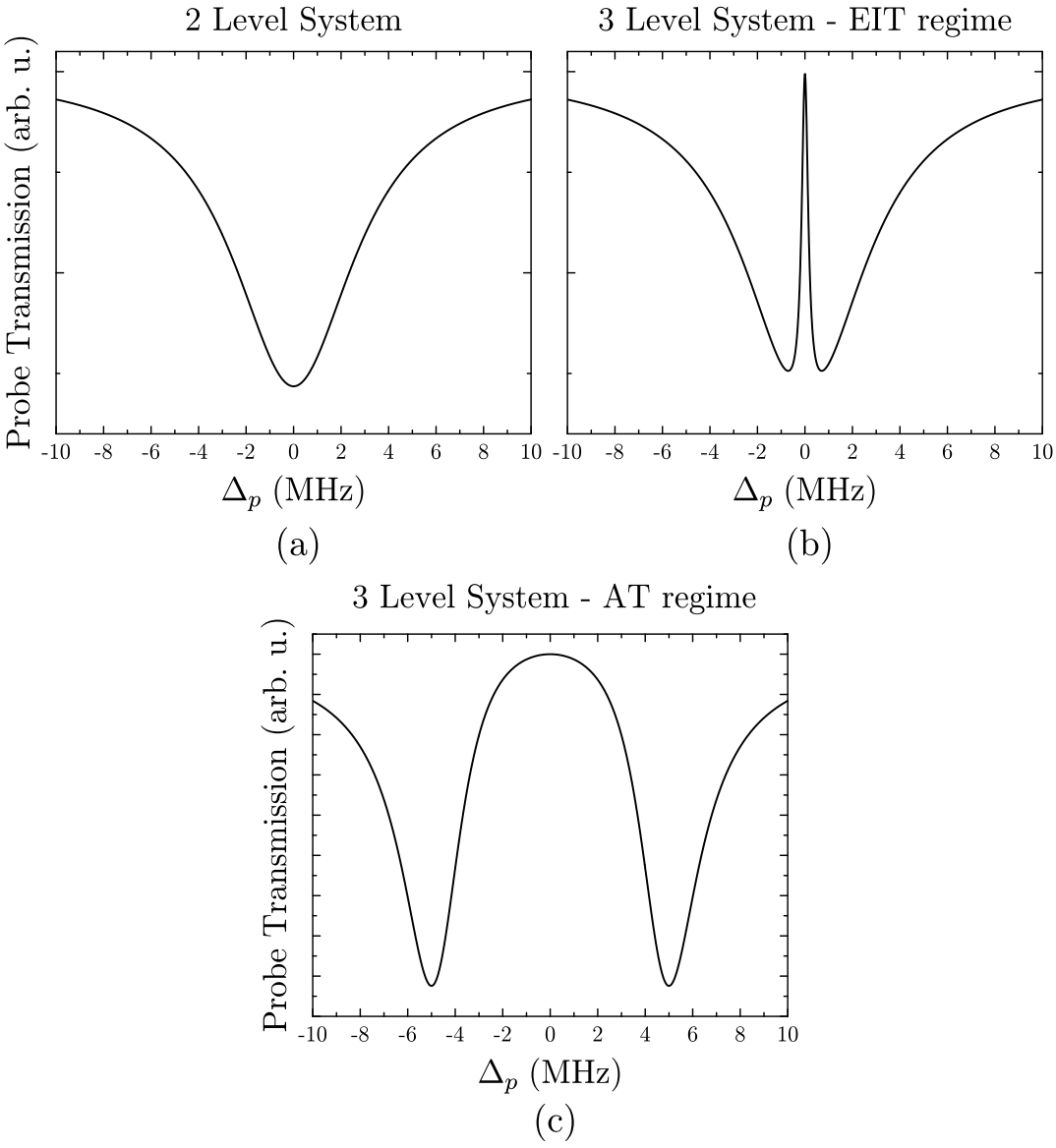

Figure 2.3: Theoretical calculations for the transmission of the probe laser for three different cases, (a) two level atom, (b) EIT regime, and (c) Autler-Townes regime.

also known as the dressed atom basis, it appears that $|2\rangle$ is split into two different states that are separated by the energy $\hbar|\Omega_c|$, this is known as Autler-Townes splitting [66]. The energy separation can be controlled by changing the intensity

of the coupling laser.

Solving the Schrödinger equation is adequate when a single wave function can describe all of the atoms in the system. However, in the following experiments this is not the case, and the density matrix formalism is used. The density matrix is suitable for dealing with *mixed states*, where atoms are in different states at the same time. In this formalism the analogue of the Schrödinger equation is the Liouville-von Neumann equation,

$$\frac{\mathrm{d}\rho(t)}{\mathrm{d}t} = \frac{1}{i\hbar}[H(t), \rho(t)] + L. \tag{2.26}$$

ρ is the density operator, and L is the decay and decoherence operator, introduced to account for spontaneous emission and other relaxation phenomena [67],

$$L_{ij} = \frac{\Gamma_{ij}}{2}\left(2\sigma_{ji}\rho\sigma_{ij} - \sigma_{ii}\rho - \rho\sigma_{ii}\right), \tag{2.27}$$

where σ is the projection operator $\sigma_{ij} = |i\rangle\langle j|$, and Γ_{ij} is the decay rate from state $|i\rangle$ to state $|j\rangle$. Evaluating Eq. 2.26 for the described systems results in a set of coupled differential equations. The coupled differential equations in Eq. 2.26 can be solved either time dependently, or in the steady state by setting $\dot{\rho}(t) = 0$. For most cases in this thesis, this equation is solved in the steady state, the exceptions will be noted. Evaluation results in nine coupled differential

equations,

$$
\begin{aligned}
\dot{\rho}_{11}(t) &= \Gamma_{21}\rho_{22}(t) - \frac{i\rho_{21}(t)\Omega_p^*}{2} + \frac{i\rho_{12}(t)\Omega_p}{2} \\
\dot{\rho}_{21}(t) &= \frac{1}{2}\left(2\Delta_p\rho_{21}(t) - \rho_{31}(t)\Omega_c^* + \Omega_p(\rho_{22}(t) - \rho_{11}(t)) + i\rho_{21}(t)\Gamma_{21}\right) \\
\dot{\rho}_{31}(t) &= \frac{i}{2}\left(2\rho_{31}(t)(\Delta_p + \Delta_c) - \rho_{21}(t)\Omega_c + \rho_{32}(t)\Omega_p + i\rho_{31}(t)\Gamma_{32}\right) \\
\dot{\rho}_{22}(t) &= \frac{i}{2}\left(\rho_{23}(t)\Omega_c - \rho_{32}(t)\Omega_c^* - \rho_{12}(t)\Omega_p + \rho_{21}(t)\Omega_p^*\right) + \rho_{33}(t)\Gamma_{32} - \rho_{22}(t)\Gamma_{21} \\
\dot{\rho}_{12}(t) &= -\frac{i}{2}\left(2\Delta_p\rho_{12}(t) - \rho_{13}(t)\Omega_c + \Omega_p^*(\rho_{22}(t) - \rho_{11}(t)) - i\rho_{12}(t)\right) \\
\dot{\rho}_{13}(t) &= -\frac{i}{2}\left(2\rho_{13}(t)(\Delta_p + \Delta_c - \frac{i}{2}\Gamma_{32}) - \rho_{12}(t)\Omega_c^* + \rho_{23}(t)\Omega_p^*\right) \\
\dot{\rho}_{23}(t) &= -\frac{i}{2}\left(2\Delta_c\rho_{23}(t) + \Omega_c^*(\rho_{33}(t) - \rho_{22}(t)) + \rho_{13}(t)\Omega_p - i\rho_{23}(t)\Gamma_{32}\right) \\
\dot{\rho}_{33}(t) &= -\frac{i}{2}\left(\rho_{23}(t)\Omega_c - \rho_{32}(t)\Omega_c^* - 2i\rho_{33}(t)\Gamma_{32}\right) \\
\dot{\rho}_{32}(t) &= \frac{i}{2}\left(2\Delta_c\rho_{32}(t) + \Omega_c(\rho_{33}(t) - \rho_{22}(t)) + \rho_{31}(t)\Omega_p^* + i\rho_{32}\Gamma_{32}\right).
\end{aligned}
\tag{2.28}
$$

The coupled differential equations can be solved for ρ_{ij}. The diagonal matrix elements ρ_{ii} are the populations in state $|i\rangle$. The off-diagonal elements ρ_{ij} are coherences between states $|i\rangle$ and $|j\rangle$. The theoretical quantity of interest is the imaginary part of ρ_{12}, as it is proportional to the absorption of the probe laser [68].

$$
\alpha(\omega_p) = \frac{2N\omega_p\mu_{21}^2}{c\epsilon_0\hbar\Omega_p}\mathrm{Im}(\rho_{12}), \tag{2.29}
$$

where N is the density of atoms, ω_p is the frequency of the probe field and μ_{21} is the transition dipole moment between state $|2\rangle$ and $|1\rangle$. α is the absorption coefficient in Beer's law [69],

$$
I(\omega_p, \ell) = I_0 e^{-\alpha(\omega_p)\ell}, \tag{2.30}
$$

where $I(\omega_p, \ell)$ is the intensity of the probe light after passing through the atoms, I_0 is the incident intensity, and ℓ is the length of the atomic sample.

The equations are solved for numerical parameters specific to this system. $\Gamma_{21} = 2\pi \times 6.07\,\text{MHz}$ is the decay rate of the $5P_{3/2}$ state. $\Gamma_{32} = 2\pi \times 1.1\,\text{kHz}$ is the inverse of the radiative lifetime of the $53D_{5/2}$ state calculated from Eq. 2.11a. Blackbody decay and ionization are small compared to the radiative lifetime and are ignored to keep the three level system closed. For experimental realizable Rabi frequences of probe and coupling lasers the system is solved for $\text{Im}(\rho_{12})$. The probe transmission in arbitrary units for several different cases is shown in Fig. 2.3. Case (a) is a two level system with $\Omega_p = 2\pi \times 1.0\,\text{MHz}$ and $\Omega_c = 0$. In case (b) both probe and coupling light is present with $\Omega_p = \Omega_c = 2\pi \times 1.0\,\text{MHz}$ and the coupling light is on resonance, $\Delta_c = 0$. A small window of transparency appears in this case around $\Delta_p = 0$. The width of transparency is much less that the linewidth of the two level transition. This is known as the EIT regime because $\Omega_c < \Gamma_{21}$. Case (c) illustrates the Autler-Townes regime with $\Omega_p = 2\pi \times 1\,\text{kHz}$ and $\Omega_c = 2\pi \times 10\,\text{MHz}$. In the Autler-Townes regime $\Omega_p \ll \Gamma_{21} \ll \Omega_c$. The narrow window of transparency is replaced with two separate resonances for the probe laser, and the frequency spacing is directly proportional to the Rabi frequency of the coupling laser. This is illustrated in Fig. 2.3c, $\Omega_c = 10\,\text{MHz}$, and the two absorption peaks have a minimum at $\pm 5\,\text{MHz}$.

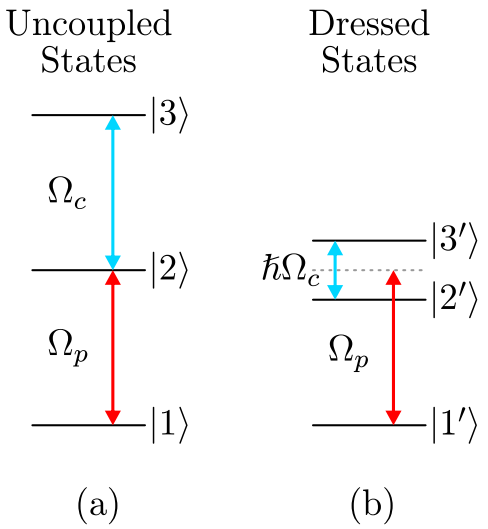

Figure 2.4: Energy level diagram for the three level system in the weak probe regime. (a) Energy levels in the uncoupled basis. (b) Energy levels in the atom-field *dressed atom* basis. This picture illustrates Autler-Townes splitting. State $|2\rangle$ is effectively split into two states, with the amount of splitting dependent on $|\Omega_c|$.

2.2.3 Doppler Averaging

Some of the experiments in this thesis are carried out in a vapor cells near room temperature. The atoms in the cell have a Maxwell-Boltzmann distribution of velocities,

$$f(v) = \frac{1}{u\sqrt{\pi}} e^{\frac{-v^2}{u^2}}, \tag{2.31}$$

where $u = \sqrt{2k_BT/M}$ is the most probable speed of atoms with mass M in a gas at a temperature T. Atoms with different velocities parallel to the direction of propagation of the laser beams will see a different laser frequency of light.

The detunings Δ become velocity dependent,

$$\begin{aligned} \Delta_p &= \omega_p - (\omega_2 - \omega_1) - \frac{\omega_p}{c} v \\ \Delta_c &= \omega_c - (\omega_3 - \omega_2) + \frac{\omega_c}{c} v. \end{aligned} \tag{2.32}$$

The Doppler shifts for the probe and coupling frequencies are not the same. To minimize Doppler broadening of the signal, the experiment is set up with the probe and coupling beams counter-propagating. The sign difference in the above equations is because the two laser beams are counter-propagating. Solving the density matrix equations for atoms in a thermal vapor requires summing up the contributions from all velocity classes. The value of ρ_{12} is evaluated at a particular velocity, and is weighted with the Maxwell-Boltzmann distribution,

$$\rho_{12\text{tot}} = \sum_v \rho_{12}(v) \frac{1}{u\sqrt{\pi}} e^{\frac{-v^2}{u^2}}. \tag{2.33}$$

2.2.4 Transit-Time Broadening

Another effect from atoms in a thermal vapor is transit-time broadening. Atoms in a thermal vapor do not interact with the laser fields continuously. Due to their velocities, atoms are constantly entering and leaving the interaction region. The interaction region is the area of overlap of the two lasers. The atoms that are entering the interaction region will be in the ground state, while atoms that are exiting can be in the ground state or an excited state. Any exiting excited state atoms will be replaced by ground state atoms, so this effect is modeled as an increase in decay rate (decrease in lifetime). The decay rates of the excited

Table 2.5: List of decay rates of relevant atomic states due to radiative decay and transit time broadening.

$5P_{3/2}$ state	Transit-time Broadening	Rydberg states
$\Gamma_{21} = 6.07\,\mathrm{MHz}$	$\Gamma_{ttb} = 150 - 300\,\mathrm{kHz}$	$\Gamma_{32} = 0.5 - 5\,\mathrm{kHz}$

states become [70],

$$\Gamma_{total} = \Gamma_{rad} + \frac{\sqrt{2}u}{D}, \tag{2.34}$$

where D is the $1/e$ diameter of the intensity of the Gaussian laser beam, and u is the most probable speed of atoms in the gas. This has the largest effect on the Rydberg state because the radiative decay rate is small compared to the experimental transit-time broadening rates, as can be seen in Table 2.5.

Chapter 3

Measuring Microwave Amplitudes with Rydberg EIT

As outlined in Section 1.3 the development of atomic measurements and standards has historically been very successful, however very little progress has been made in the area of microwave electric fields. Recently there has been some work done with measuring microwave magnetic fields in atomic vapor [71, 72, 73, 74]. These approaches use microwaves to drive magnetic dipole transitions between ground states in Rb. This approach can only be used with a handful a hyperfine splittings of alkali atoms, and its sensitivity is limited by the strength of the magnetic dipole transition.

In the following experiments, microwaves drive electric dipole transitions between Rydberg atoms. Driving Rydberg-Rydberg transitions with microwaves has been done for decades, [40, 75, 76, 77, 78]. The novel idea of these experiments is to combine resonant microwaves with the recent developments of Rydberg atom EIT [62]. One of the big advantages of this approach is the optical readout of the signal. The detection can be done far away from the atoms being studied. Traditionally, Rydberg atom experiments are carried out in large apparatuses involving an ultra high vacuum environment and metal vacuum chambers. Additionally, data is usually taken by detecting ions after pulsed field ionization. These methods introduce large masses of metal in the atomic region

causing large perturbations of an incident microwave field. Here, experiments are done in a glass vapor cell, and the signal is detected on a photodiode far away from the cell alleviating these problems. Unlike dipole antennas which have traditionally been used for microwave electric field measurement, the size of vapor cell can be $\ll \lambda_{MW}$. Miniaturizing the vapor cell minimizes the perturbation of field due to the vapor cell.

3.1 Amplitude Measurement

The microwave measurement is performed using a modified version of the Rydberg atom EIT presented in Section 2.2. A second Rydberg state is added to the system, and the two Rydberg states are coupled together by microwaves as illustrated in Fig. 3.1a. Calculations are performed using the same theoretical tools as the 3-level system, however a fourth level is added. The Hamiltonian is,

$$H' = \frac{\hbar}{2}\begin{pmatrix} 0 & \Omega_p^* & 0 & 0 \\ \Omega_p & -2\Delta_p & \Omega_c^* & 0 \\ 0 & \Omega_c & -2(\Delta_p+\Delta_c) & \Omega_{MW}^* \\ 0 & 0 & \Omega_{MW} & -2(\Delta_p+\Delta_c-\Delta_{MW}) \end{pmatrix}. \tag{3.1}$$

The quantities Ω_{MW} and Δ_{MW} are defined following the definitions for the probe and coupling fields in Eq. 2.17 and Eq. 2.22 respectively,

$$\begin{aligned} \Omega_{MW} &= \frac{E_{MW}}{\hbar}\langle 4|\hat{\epsilon}_{MW}\cdot e\mathbf{r}|3\rangle \\ \Delta_{MW} &= \omega_{MW} - (\omega_4 - \omega_3)\,. \end{aligned} \tag{3.2}$$

Transit time broadening of the second Rydberg state is included in the calculation. Doppler shifts of the microwave frequencies are ignored because they are 4-5

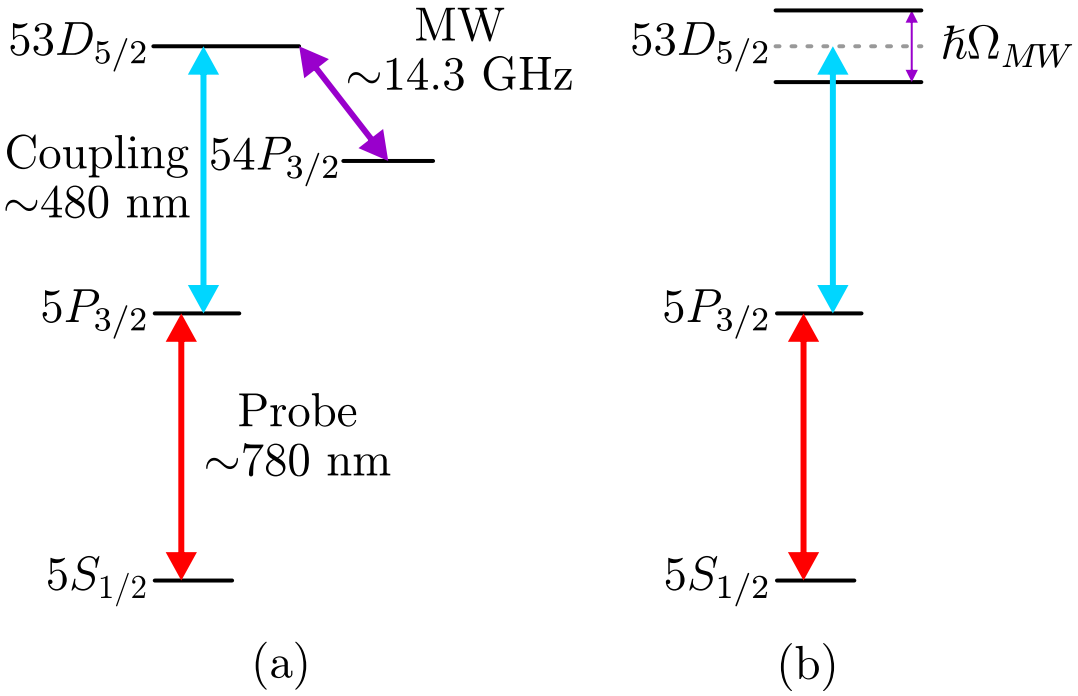

Figure 3.1: Energy level diagrams of the 4-level system used to measure MW electric fields. (a) Bare atom energy level diagram. (b) Energy level diagram in the dressed state picture for large Ω_{MW}, which shows the Autler-Townes splitting of the $53D_{5/2}$ state.

orders of magnitude smaller than the shifts at optical frequencies, and are too small to be observed.

The Rydberg EIT system converts the amplitude of the microwave electric field into an optical frequency measurement, as can be seen in Fig. 3.1b. In this situation there is Autler-Townes splitting of the $53D_{5/2}$ state due to the microwaves. Similar to the Autler-Townes splitting on the $5P_{3/2}$ state detailed in Section 2.2.2, H' can be diagonalized with the conditions, $\Omega_{MW} \gg \Omega_p, \Omega_c$ and

$\Delta_{MW} = 0$. The resulting eigenenergies are,

$$\begin{aligned} E_1' &= 0 \\ E_2' &= -\hbar\Delta_p \\ E_3' &= -\hbar\Delta_p - \hbar\Delta_c - \frac{\hbar|\Omega_{MW}|}{2} \\ E_4' &= -\hbar\Delta_p - \hbar\Delta_c + \frac{\hbar|\Omega_{MW}|}{2}. \end{aligned} \tag{3.3}$$

The dark state from the 3-level system is now split into two states E_3' and E_4' with an energy spacing of $\hbar|\Omega_{MW}|$, and the medium absorbs the probe laser on resonance. The difference in probe transmission between a non-Doppler 3 and 4-level system is shown in Fig. 3.2. The Rabi frequencies used in the calculation are $\Omega_p = \Omega_c = \Omega_{MW} = 2\pi \times 1\,\text{MHz}$, except for the 3-level case when $\Omega_{MW} = 0$. The window of transparency is split into two and the peak separation is equal to $\Omega_{MW}/2\pi$.

3.1.1 Doppler Mismatch

When the probe laser is scanned in a Doppler medium, the energy of the Autler-Townes splitting of the Rydberg state is not equal to the frequency separation of the two transparency peaks. Rather, the observed splitting is multiplied by a factor of λ_c/λ_p. This is illustrated in Fig. 3.3, where the coupling laser is fixed and the probe laser is scanned. The experimentally measured splitting is Δ_{split}. The two sets of arrows in the level diagram of Fig. 3.3a show the resonance condition for each transmission peak. The two transparency peaks appear when both lasers are on resonance with the same velocity class of atoms. Since the

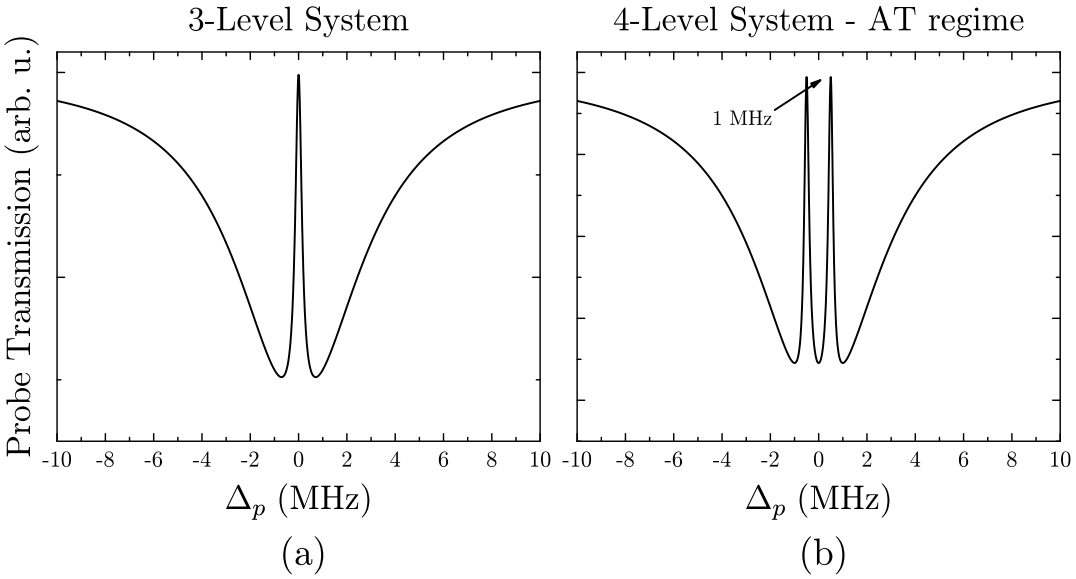

Figure 3.2: Theoretical calculations of the probe transmission for 3 (a) and 4-level (b) systems. No Doppler averaging or transit-time broadening is included. The transmission window is split into two different windows in the 4-level case. The splitting of the peaks is 1 MHz, which is equal to the Rabi frequency of the microwaves, Ω_{MW}.

coupling laser is fixed, each peak is a result of satisfying the $\Delta_p + \Delta_c = 0$ condition, with atoms having different velocities, v_1 and v_2. The relative Doppler shift of the coupling frequency between the two velocities of atoms is,

$$\Delta_{\text{Ryd}} = \frac{2\pi}{\lambda_c}\left(v_2 - v_1\right). \tag{3.4}$$

The corresponding shift of the probe frequency for atoms with velocities v_1 and v_2 is,

$$\Delta_{\text{split}} = \frac{2\pi}{\lambda_p}\left(v_2 - v_1\right). \tag{3.5}$$

Combining Eq. 3.4 and 3.5, Δ_{split} becomes,

$$\Delta_{\text{split}} = \frac{\lambda_c}{\lambda_p}\Delta_{\text{Ryd}}. \tag{3.6}$$

The measured Δ_{split} is less than the splitting between Rydberg states Δ_{Ryd}. The result is general for a ladder system and also applies to splitting between fine structure Rydberg states [62]. If the probe laser is fixed and the coupling laser is scanned, then $\Delta_{\text{Ryd}} = \Delta_{\text{split}}$. In this case, the probe laser will always be on resonance with the same velocity atoms, so the position of the intermediate state will remain the same. The coupling laser detuning is then equal to the energy splitting.

3.1.2 Experimental Setup and Results

The measurements take place in a glass vapor cell at or slightly above room temperature, where two lasers and the microwaves interact with ^{87}Rb atoms. A schematic of the experimental setup is shown in Fig. 3.4. The probe laser ($\sim 780\,\text{nm}$) is resonant with the $5S_{1/2}(F = 2) \leftrightarrow 5P_{3/2}(F = 3)$ transition and is overlapped inside the cell with a counter propagating coupling laser ($\sim 480\,\text{nm}$) resonant with the $5P_{3/2}(F = 3) \leftrightarrow 53D_{5/2}$ transition inside of a vapor cell. The coupling light is derived from a homebuilt frequency doubling system described in Section 4.6.5. A microwave field resonant with the $53D_{5/2} \leftrightarrow 54P_{3/2}$ is also incident upon the cell. From the microwave source (HP 8341B), microwaves are coupled into a waveguide and horn antenna, which directs them toward the

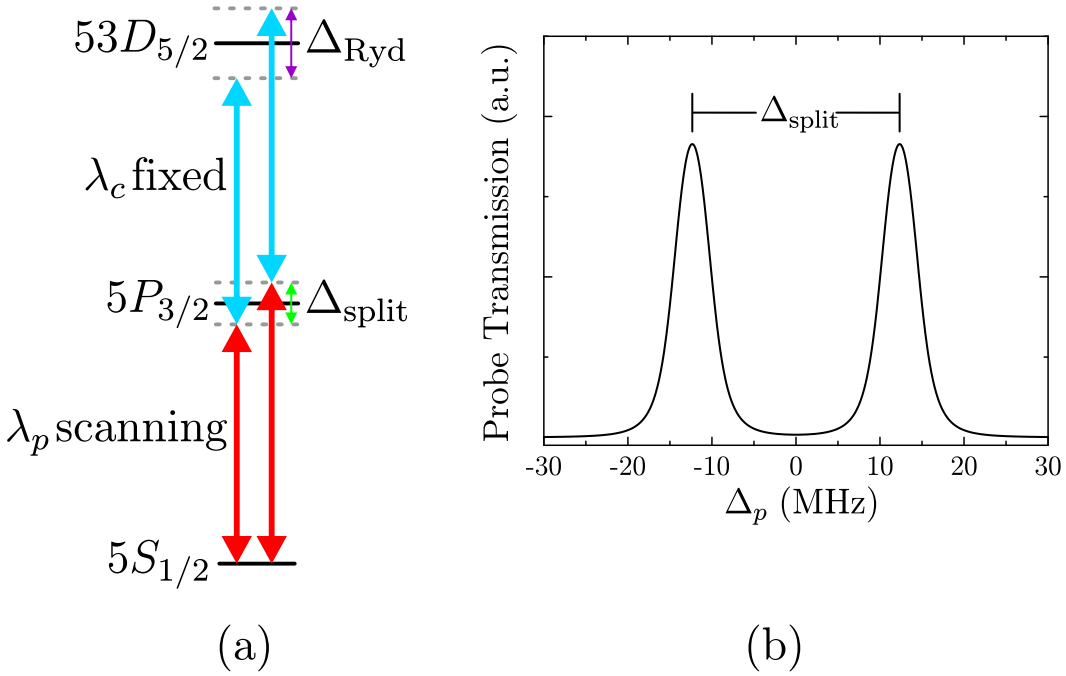

Figure 3.3: Effects of Doppler averaging the 4-level system. (a) The splitting of the Rydberg state is mapped onto the splitting measured by scanning the probe laser. The arrows on the left and right correspond to resonance conditions for atoms of different velocities. (b) Results of the Doppler averaged calculation for $\Omega_{MW} = 2\pi \times 40\,\mathrm{MHz}$. The peaks in the figure are split by $\Delta_{\mathrm{split}} = 40\frac{480}{780}\,\mathrm{MHz} = 24.6\,\mathrm{MHz}$.

vapor cell. The propagation direction of the microwaves is orthogonal that of both laser beams. All three fields are polarized along the x-direction.

The measurement is done optically by detecting the transmission of the probe light on a photodiode. This allows for detection electronics and other metal objects to be positioned far away from the detector. The observed signal is

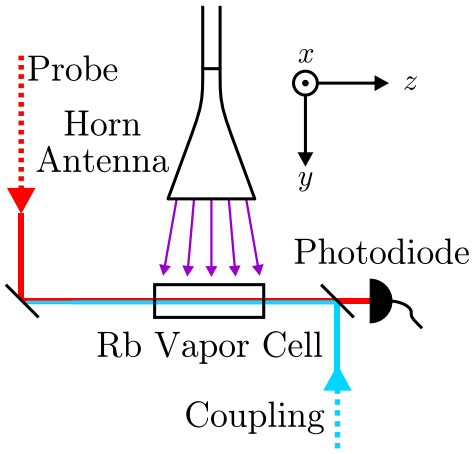

Figure 3.4: A schematic of the experimental setup.

small, so, to increase the signal-to-noise ratio, the coupling light is amplitude modulated by using an acousto-optic modulator and the signal is processed using a lock-in amplifier.

Experimental results for no microwaves and increasing microwave powers, while scanning the probe laser frequency are shown in Fig. 3.5a. For no microwaves a single peak is observed. As the microwave power is increased the peak starts to split into two separate peaks. According to Eq. 3.7, Δ_{split} scales linearly with the applied E_{MW}. Testing this experimentally, EIT spectra are taken for many different microwave powers P_{MW} by changing the power of the front panel of the microwave generator. To determine the position of the peaks, the spectra are fit to a function of two Gaussians. The results are plotted in black in Fig. 3.5b. The red line is a linear fit to the data, confirming the experimental results are consistent theoretical expectations.

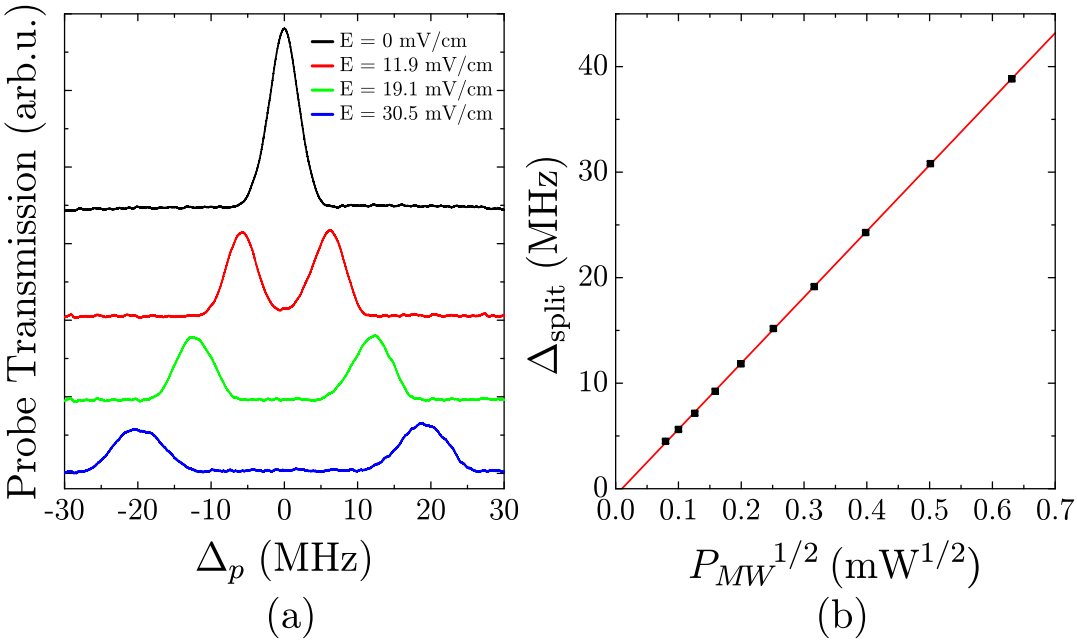

Figure 3.5: Experimental lineshapes for 3-level EIT (black) and 4-level EIT for increasing MW powers. (b) Plot of the experimental measured splittings as a function of the square root of microwave power. The vertical error bars, ±200 kHz, are due to the experimental uncertainty in the frequency of the splitting, and are smaller than the points. The red line is a linear fit to the data.

3.1.3 Calculating Electric Field Amplitude

The electric field can be calculated using the formula,

$$E_{MW} = \frac{h\Delta_{\text{split}}\lambda_p}{\mu_{MW}\lambda_c}. \tag{3.7}$$

For the blue curve in Fig. 3.5a, $\Delta_{\text{split}} = 38.8 \pm 0.2$ MHz. $\lambda_p = 780.246$ nm and $\lambda_c = 480.005$ nm are measured with a commercial wavemeter with an uncertainty of ±0.001 nm. λ_c agrees with quantum defect calculations, and

Table 3.1: Relative uncertainties in the calculation of the electric field. The uncertainty in the Planck constant is from the 2014 CODATA [80]. Experimental uncertainties of the wavelengths and Δ_{split} are calculated using numbers in the text. The estimated uncertainty of the wavefunctions is the source of the uncertainty in μ_{43}.

Quantity	Relative Uncertainty
h	1.2×10^{-8}
λ_p	1×10^{-6}
λ_c	2×10^{-6}
μ_{43}	0.01
Δ_{split}	0.01-0.04

λ_p is consistent with more precise experimental values [57]. In principle, the wavelengths can be measured with more precision using frequency combs yielding relative uncertainties of 2×10^{-14} [79]. The transition dipole moment is calculated to be $\mu_{MW} = 1619ea_0$, the details of the calculation are in Appendix A. Using all of these values the calculated electric field is $E_{MW} = 30.4 \pm 0.2\,\text{mV/cm}$. The uncertainties in the calculation are detailed in Table 3.1. This list does not consider systematic errors present in the experiment. The largest systematic error is due to a background magnetic field, which will shift the states and change μ_{MW} by $\sim 1\%$.

3.1.4 Small Fields

At electric fields of $\sim 10\,\mathrm{mV/cm}$ the measured splittings are used to calibrate the system, and smaller electric fields are measured when the system is not in the Autler-Townes regime. With the three fields on resonance the probe transmission is monitored as the strength of the MW field is varied, shown in Fig. 3.6a. The black curve is experimental data and the red curve is the result of the 4-level density matrix calculation. For these experimental parameters the probe transmission is increased until $\sim 1400\,\mu\mathrm{V/cm}$ with a maximum at $\sim 700\,\mu\mathrm{V/cm}$. The increase in transmission is counter-intuitive, but can be explained by looking at the probe transmission as a function of velocity, Fig. 3.6b. The total signal is the sum over all velocities. The MW electric field broadens the transmission in velocity space. The area under the red curve is larger that the black curve. For small MW fields the contribution from nonzero velocity atoms increases the signal. This effect is only present in a Doppler broadened sample of atoms.

To determine the smallest MW field we can detect, the probe and coupling lasers are kept on resonance while the MW frequency is scanned across resonance, as shown in Fig. 3.7a. The black curves are experimental data and the red curves are Gaussian fits to the data. Each experimental trace is an average of 9000 scans. The peak heights from the Gaussian fits are plotted (black squares) along with the theoretical expectations (black line) in Fig. 3.7b. The dashed red

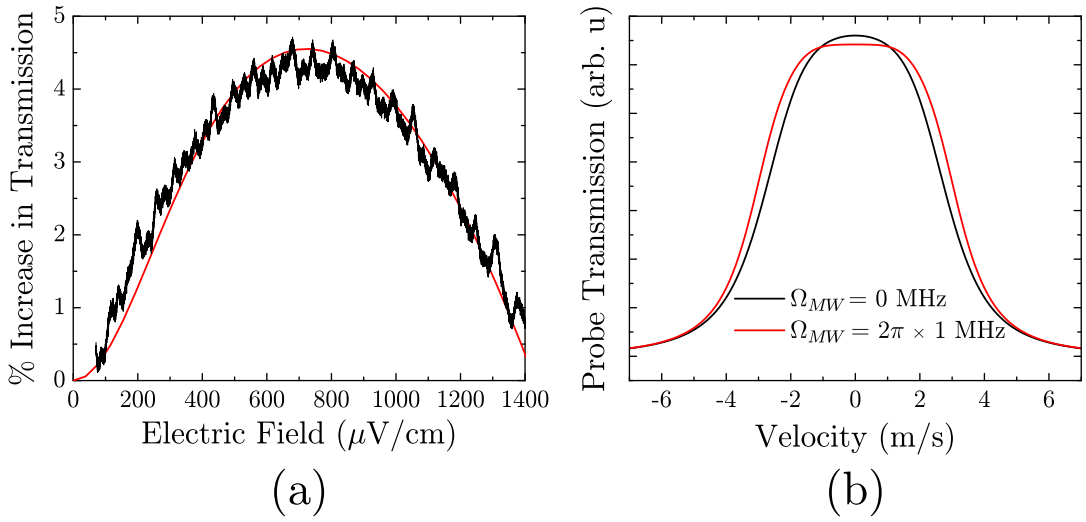

Figure 3.6: (a) Plot showing the increase of probe transmission for small E_{MW}. The black line is experimental data. The red line is the results of theoretical calculation. (b) Velocity contributions to the transmission signal.

(blue) lines show the theoretical variation for a change of $\pm 10\%$ of the coupling (probe) power.

The lowest detected MW electric field is $8.33 \pm 0.37\,\mu$V/cm. The error bars are mainly due to the technical noise and the uncertainty in the applied microwave field.

3.2 Polarization Measurement

In the previous section, the amplitude of the MW electric field was of interest. In addition, using the same system, the polarization of the MW electric field can also be measured. The polarization measurement uses the hyperfine structure of

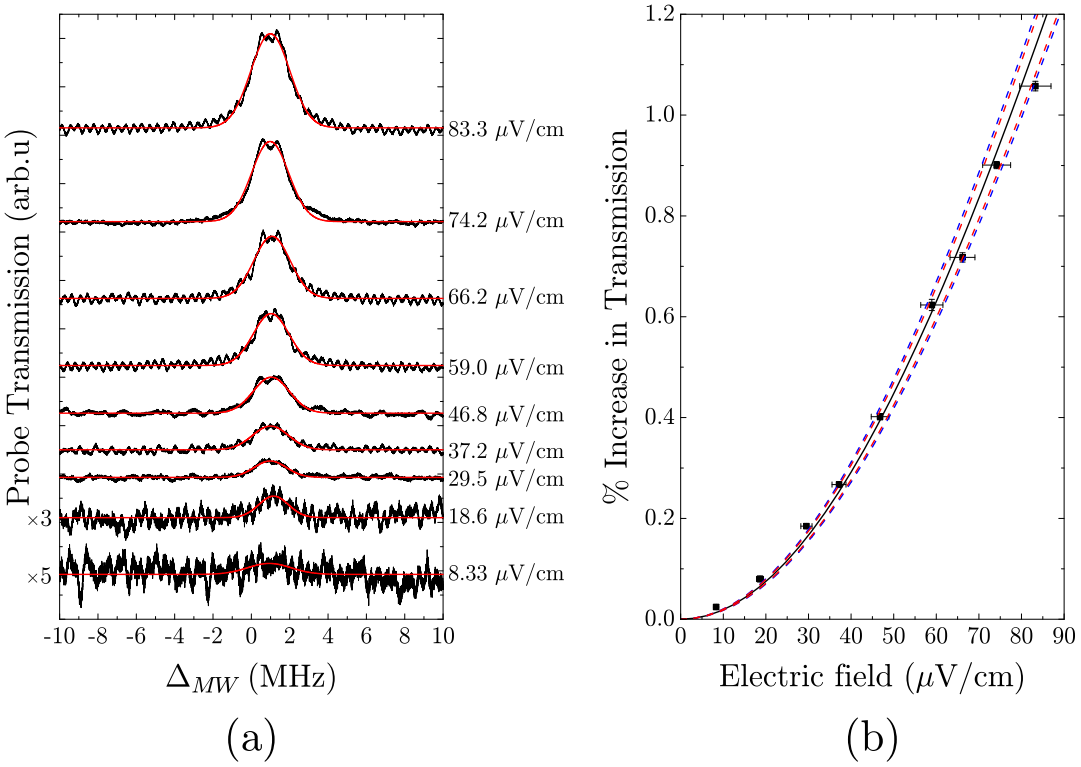

Figure 3.7: Increase in probe transmission for small MW fields. (a) Plot of the increased transmission as the MW are scanned across resonance, for various E_{MW} The black lines are experimental data, and the red lines are Gaussian fits to the data. (b) The maximum of the Gaussians in (a) are plotted in as black points. The vertical error bars are due to the uncertainty in the fit. The horizontal error bars are due to the uncertainty in the applied electric field. The black line is the theoretical calculation.

the 4 levels and the associated selection rules for the three fields. To understand the measurement, the simple 4 state model needs to be abandoned, and we have to consider the degenerate magnetic sublevels for each state as shown in

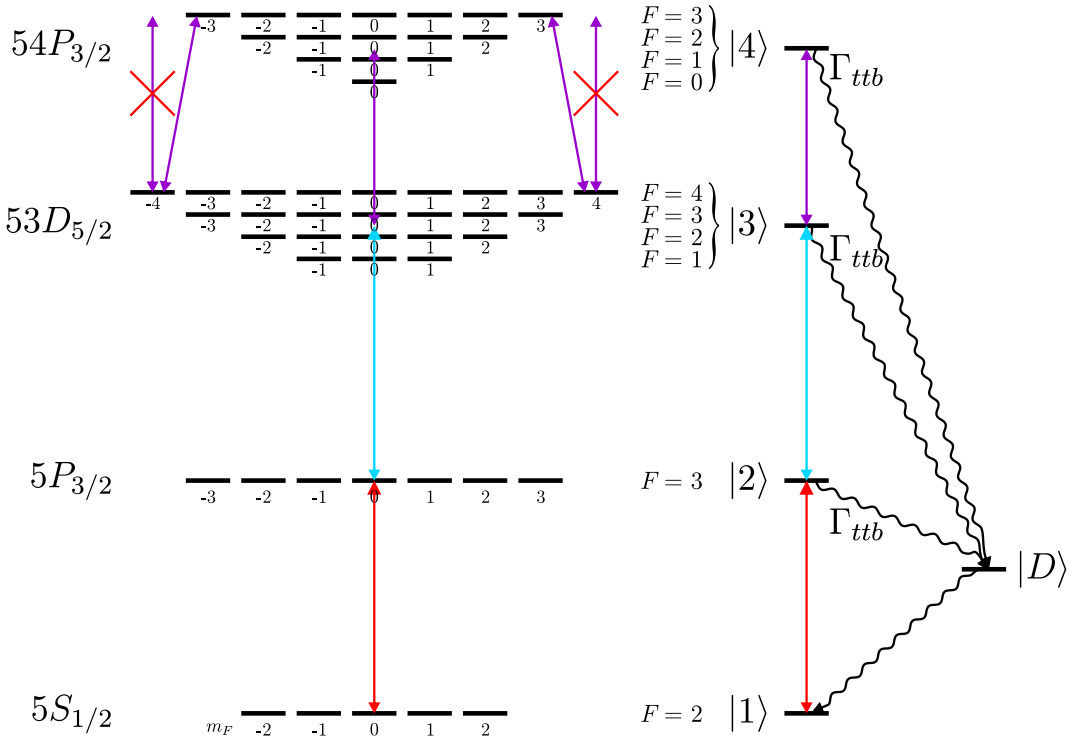

Figure 3.8: Complete energy level diagram of the system including hyperfine structure. Each set of states is degenerate, and is labeled by $|i\rangle$. A dummy state $|D\rangle$ is included in the calculation to simplify the decay due to transit time broadening of the excited states.

Fig. 3.8. The 4 states from the previous treatment, now become 52 states. For each level $|1\rangle - |4\rangle$ the states are degenerate in energy. The hyperfine splittings for the $5S_{1/2}$ and $5P_{3/2}$ states, 6.8 GHz and 266 MHz respectively, are easily resolved such that only a single F is considered. For the nP and nD Rydberg states, the hyperfine splitting is negligible [52] and the states are considered to be degenerate.

The sensitivity of the system to the MW polarization can be seen by looking

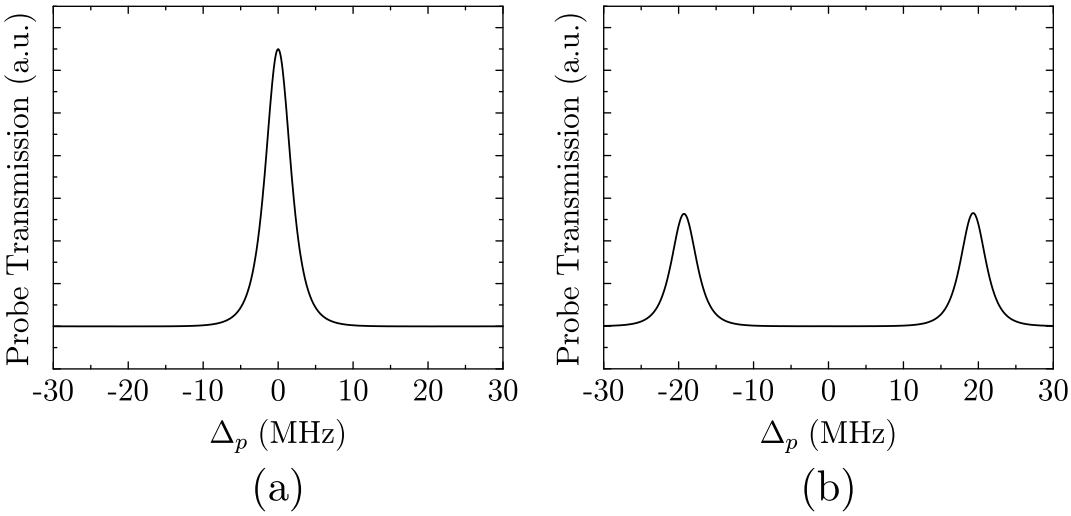

Figure 3.9: Theoretical probe transmission spectra of (a) 3 and (b) 4-level Rydberg atom EIT spectra. Lineshapes are polarization dependent combinations of each case.

at the allowed MW transitions. If the MWs are π polarized, they will drive $\Delta m_F = 0$ transitions. Any atoms that are coupled to the stretched $F = 4$ $m_F = \pm 4$ states in the $53D_{5/2}$ manifold will not be coupled to the $54P_{3/2}$ manifold, shown in purple. These atoms will not be affected by the microwaves and will effectively be in a 3-level system. Atoms that are coupled to the other states in the $53D_{5/2}$ manifold will be in a 4-level system. In an ensemble of atoms some will exhibit 3-level behavior others will have 4-level behavior, so experimental lineshapes can be characterized as combinations of three and four level EIT as shown in Fig. 3.9.

3.2.1 Theory

Calculations for the system shown in Fig. 3.8 were carried out. The basics of the calculation are the same as for the 4-level theory. However, there are some significant differences, which will be highlighted. Rabi frequencies and radiative decay between states depend on the quantum numbers of each state. States are numbered by i, j ranging from $1 - 52$ with $|i\rangle = |n_i, L_i, S_i, J_i, F_i, m_{Fi}\rangle$.

A set of coupled differential equations for $\dot{\rho}_{ij}$ are constructed similar to Eq. 2.28, but in this case there are 53×53 equations. 52 of the states correspond to the magnetic sublevels shown on the left side of Fig. 3.8. The last state is a dummy state $|D\rangle$ shown on the right side of Fig. 3.8, and is used for including transit-time broadening effects. The decay back to the ground state due to transit time broadening will equally populate the five ground states. Instead of having five separate decay rates for each excited state, they each have one decay rate into $|D\rangle$, then $|D\rangle$ decays equally into each of the 5 ground states. The total decay rate of both states is equal to Γ_{ttb}.

Rabi Frequencies

Resonant fields couple different magnetic sublevels, so a separate Rabi frequency is needed between each state,

$$\Omega_{ij} = \frac{E\mu_{ij}}{\hbar}. \tag{3.8}$$

Table 3.2: List of the coefficients needed to calculate Rabi frequencies for different polarization cases. The associated Δm_F selection rules are also listed.

Polarization direction	$\sum_{q=-1}^{1} A_q \epsilon_q$	Transitions
$\hat{x}$ (linear)	$\frac{1}{\sqrt{2}}(\epsilon_{-1} - \epsilon_1)$	$\Delta m_F = \pm 1$
$\hat{y}$ (linear)	$\frac{-i}{\sqrt{2}}(\epsilon_{-1} + \epsilon_1)$	$\Delta m_F = \pm 1$
$\hat{z}$ (linear)	ϵ_0	$\Delta m_F = 0$
$\frac{1}{\sqrt{2}}(\hat{x} - i\hat{y})$ (circular)	ϵ_1	$\Delta m_F = +1$
$\frac{-1}{\sqrt{2}}(\hat{x} + i\hat{y})$ (circular)	ϵ_{-1}	$\Delta m_F = -1$

The transition dipole moment $\mu_{ij} = \langle i|\hat{\epsilon} \cdot e\mathbf{r}|j\rangle$. $\hat{\epsilon}$ is the polarization unit vector of the electric field, E_p, E_c, or E_{MW}. The polarization of the three fields are either linearly or circularly polarized. In order to describe these polarizations, $\hat{\epsilon}$ is written in the spherical basis $\hat{\epsilon}_q$,

$$\begin{aligned} \hat{\epsilon}_{+1} &= -\frac{1}{\sqrt{2}}(\hat{x} + i\hat{y}) \\ \hat{\epsilon}_0 &= \hat{z} \\ \hat{\epsilon}_{-1} &= \frac{1}{\sqrt{2}}(\hat{x} - i\hat{y}). \end{aligned} \tag{3.9}$$

The value of $\hat{\epsilon} \cdot \hat{r}$ depends on the polarization of the electric field with,

$$\hat{\epsilon} \cdot \hat{r} = \sum_{q=-1}^{1} A_q \epsilon_q. \tag{3.10}$$

The values for several common polarizations are shown in Table 3.2. The dipole moment can be separated into radial and angular parts, $\mu_{ij} = \mu_{r_{ij}} \times \mu_{a_{ij}}$. The radial part is only dependent on n, n', L, and L', $\mu_{r_{ij}} = \langle nL|r|n'L'\rangle$. $\mu_{r_{ij}}$'s value is the same for every transition between the same two levels. $\mu_{a_{ij}}$ will differ

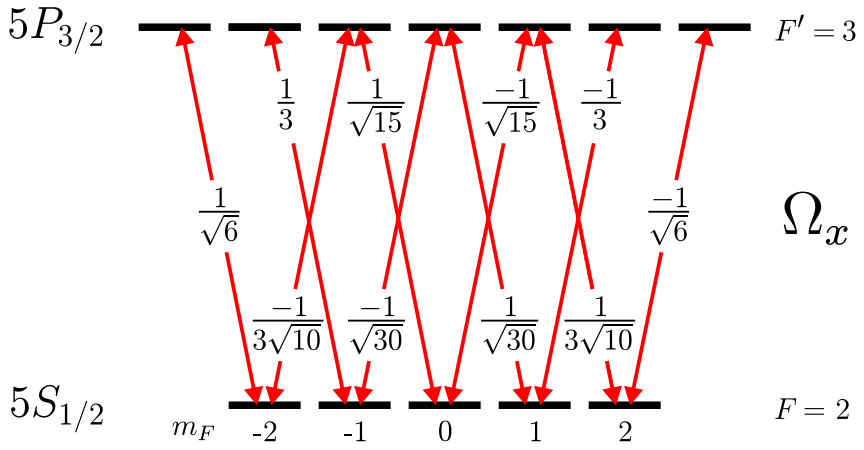

Figure 3.10: Angular parts of Ω_p coupling states on the $5S_{1/2}, (F = 2) \leftrightarrow 5P_{3/2}, (F' = 3)$ transition for probe light polarized along the x-direction. The selection rules for this case are $\Delta m_F = \pm 1$

for transitions between different magnetic sublevels, giving each transition a different dipole moment. As an example, the values of $\mu_{a_{ij}}$ for the probe laser polarized along the x-direction are shown in Fig. 3.10. Complete expressions for $\mu_{r_{ij}}$ and $\mu_{a_{ij}}$ are in Appendix A.

Radiative Decay

When considering magnetic sublevels, states no longer decay into only one state. A single upper state can decay into multiple lower energy states. It is necessary to specify a decay rate for state $|i\rangle$ to $|j\rangle$,

$$\Gamma_{ij} = \Gamma_0 \Gamma_{bij}, \tag{3.11}$$

where Γ_0 is the total decay rate as defined in Table 2.5, and Γ_{bij} is the branching ratio from initial state $|i\rangle$ to final state $|j\rangle$. Radiative decay follows dipole

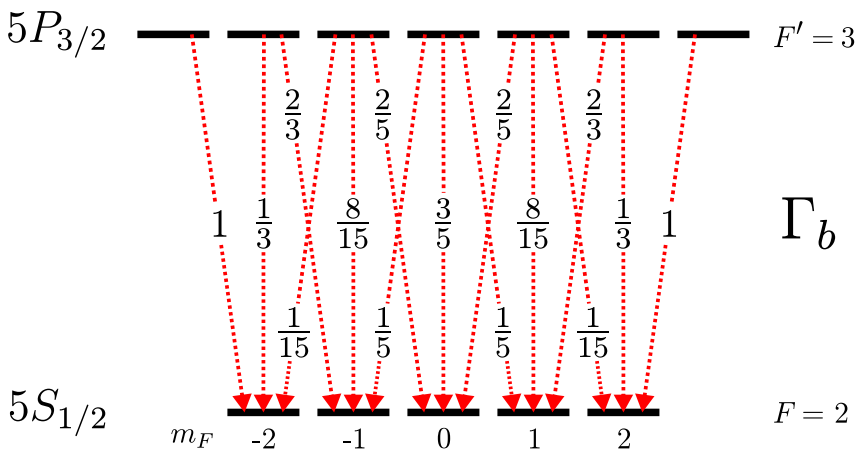

Figure 3.11: Branching ratios for radiative decay from $5P_{3/2}, (F' = 3) \rightarrow 5S_{1/2}, (F = 2)$. There is another hyperfine ground state, $5S_{1/2}, (F = 1)$, but because of selection rules ($\Delta F = \pm 1, 0$) there is no decay from $5P_{3/2}, (F' = 3)$. The branching ratios for each excited state sum to 1. For example the branching ratios for $5P_{3/2}, (F' = 3, m_F = 0)$ are $1/5 + 3/5 + 1/5 = 1$.

selection rules, which includes the condition that $\Delta m_F = 0, \pm 1$. The branching ratio for the transition between an upper level $|L, S, J, F, m_F\rangle$ and a lower state with $|L', S', J', F', m'_F\rangle$ is [81],

$$\begin{aligned}\Gamma_{bij} =& (2L+1)(2J+1)(2J'+1)(2F+1)(2F'+1)\times \\ & \begin{Bmatrix} L' & J' & S \\ J & L & 1 \end{Bmatrix}^2 \begin{Bmatrix} J' & F' & I \\ F & J & 1 \end{Bmatrix}^2 \begin{pmatrix} F' & 1 & F \\ -m'_F & m'_F - m_F & m_F \end{pmatrix}^2 .\end{aligned} \tag{3.12}$$

Radiative decay is only considered between levels $|2\rangle \rightarrow |1\rangle$, $|3\rangle \rightarrow |2\rangle$, and $|4\rangle \rightarrow |2\rangle$. An example of the branching ratios for the $|2\rangle \rightarrow |1\rangle$ transition is

shown in Fig. 3.11. For each excited state the total decay rate is equal to Γ_0,

$$\sum_j \Gamma_{bij} = 1. \tag{3.13}$$

Selection rules for radiative decay create coherences between ground states. Terms accounting for the coherence between multiple ground states need to be added to the decay and decoherence operator L_{ij}, Eq. 2.27. The decay and decoherence operator is redefined as,

$$L_{ij} = \frac{\Gamma_{ij}}{2}\left(2\sigma_{ji}\rho\sigma_{ij} - \sigma_{ii}\rho - \rho\sigma_{ii}\right) + Lg_{ij}. \tag{3.14}$$

The coherences between ground states with the same F are [82],

$$\begin{aligned} Lg_{ij} =& \Gamma_{21} \sum_{m'_{F1}=-F'}^{F'} \sum_{m'_{F2}=-F'}^{F'} \sum_{q=-1}^{1} (-1)^{m'_{F1}+m'_{F2}} \sqrt{(2F'+1)(2F'+1)} \\ & \times \begin{pmatrix} F & 1 & F_p \\ i-F+1 & q & -m'_{F1} \end{pmatrix} \begin{pmatrix} F & 1 & F_p \\ j-F+1 & q & -m'_{F2} \end{pmatrix} \\ & \times \rho_{m'_{F1}+2F+F'+2, m'_{F2}+2F+F'+2} \end{aligned} \tag{3.15}$$

where $\Gamma_{21} = 2\pi \times 6.07\,\mathrm{MHz}$ as defined in Table 2.5. In this case the excited states have only one F' and the sums are over different excited m'_F states. For $i = 1$ and $j = 2$, Lg_{12} depends on the coherences between excited states,

$$Lg_{12} = \Gamma_{21}\left(\sqrt{\frac{2}{3}}\rho_{67} + \frac{2}{3}\sqrt{\frac{2}{5}}\rho_{78} + \frac{1}{5\sqrt{3}}\rho_{89}\right). \tag{3.16}$$

Similar coherence terms were added for excited and Rydberg states, however the effect was negligible due to non zero radiative decay time of those states.

After calculating all of the needed terms, the resulting set of equations has 2500+ equations and variables. Due to the enormity of the system, Mathematica

is unable to algebraically solve the system in the steady state. The system is solved time dependently and evaluated at time $t = 6.4\,\mu$s, when the system is in the steady state. The solutions of interest are all of the ρ_{ij} between ground and first excited states, ρ_{ge}. The absorption of the probe laser is calculated by summing over all of the probe transitions,

$$\alpha(\omega_p) = \frac{2N\omega_p}{c\epsilon_0\hbar}\sum_{g,e}\frac{\mu_{eg}^2\mathrm{Im}(\rho_{ge})}{\Omega_{eg}}. \tag{3.17}$$

3.2.2 Analysis of Several Cases

To demonstrate the sensitivity of the system to polarizations, it is instructive to look at three different cases in detail. First, consider the case where all three fields are polarized along the x-direction, Fig. 3.12. This is the case that was used in the amplitude measurements. By looking at Fig. 3.12 all of the fields are coupling σ ($\Delta m_F = \pm 1$) transitions. Thus the line shape is from a purely 4 state system.

In the second case, both laser polarizations are rotated by 90° so that they are aligned along the y-axis, while the microwaves remain polarized along the x-axis. To simplify this explanation the quantization axis is considered to lie along the $\hat{x}$-direction. The lasers are σ polarized and couple $\Delta m_F = \pm 1$ transitions, while the microwaves are π polarized and couple $\Delta m_F = \pm 1$ transitions. Most of the ground state population will be optically pumped toward the $m_F = \pm 2$ states. Atoms in these stretched states will be strongly coupled to the stretched states in the $53D_{5/2}$ manifold, which are not coupled to the $54P_{3/2}$ manifold. Not all

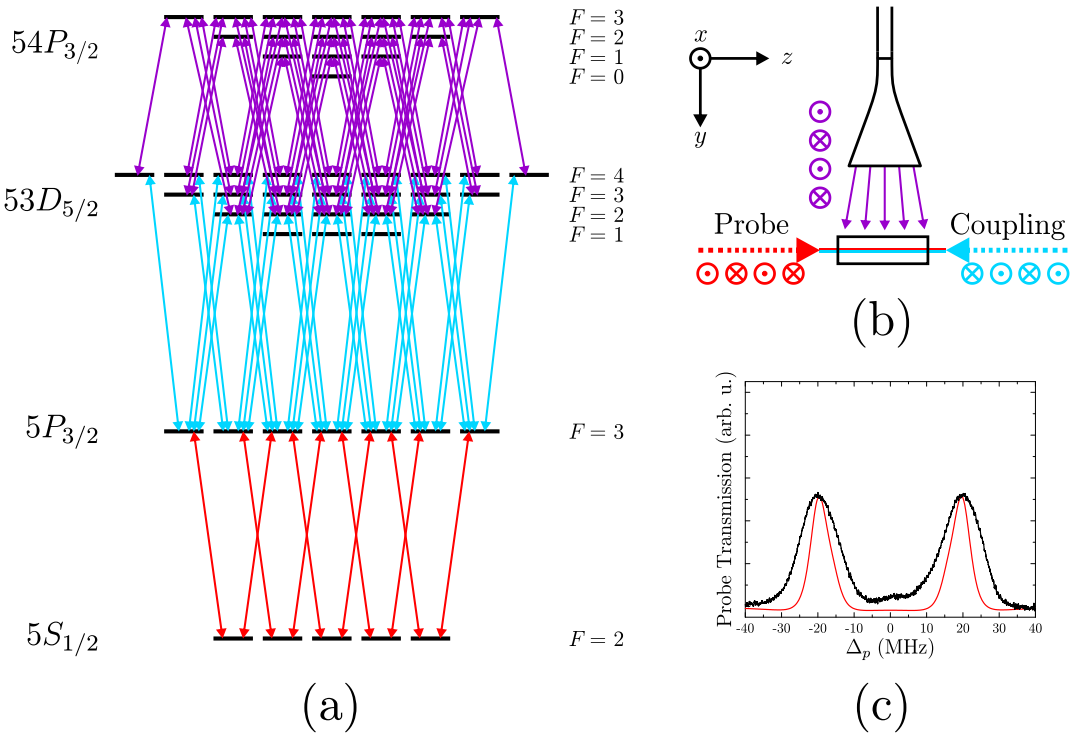

Figure 3.12: Case 1, $\hat{E}_p = \hat{E}_c = \hat{E}_{MW} = \hat{x}$. (a) Arrows show allowed transitions in the system, each field couples states together with $\Delta m_F = \pm 1$. All of the states in the $53D_{5/2}$ manifold are coupled to states in the $54P_{3/2}$ manifold. (b) Schematic of the experimental setup indicating polarization and propagation direction of the three fields. (c) Experimental (black) and theoretical (red) results.

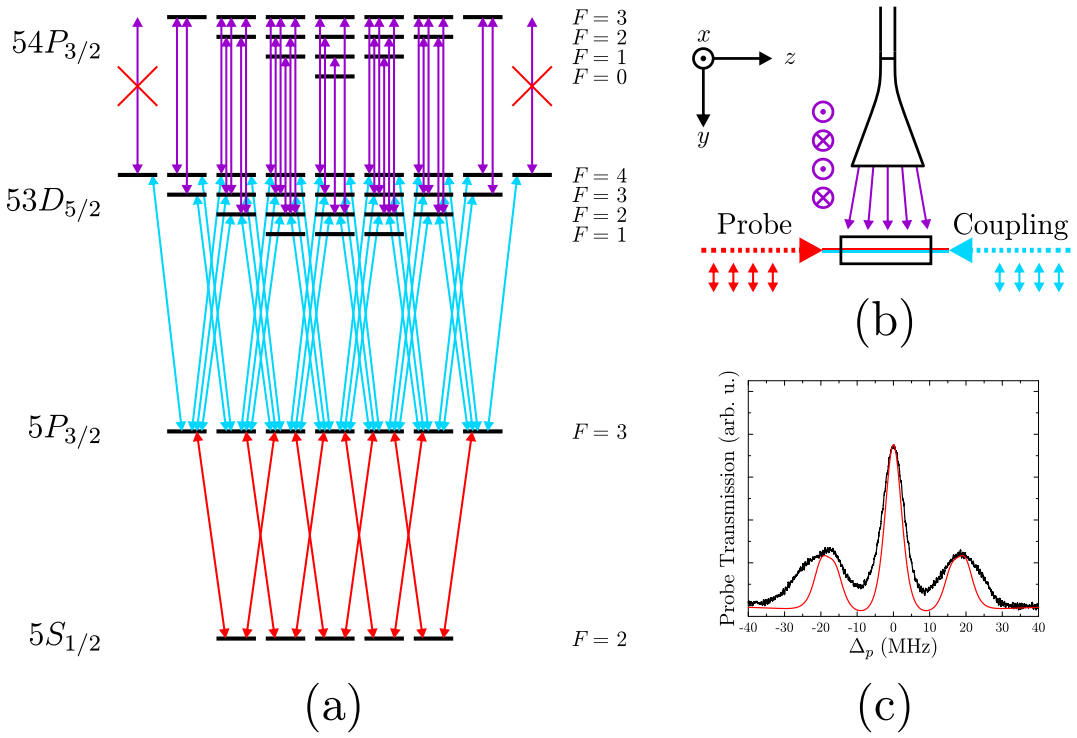

Figure 3.13: Case 2, $\hat{E}_p = \hat{E}_c = \hat{y}, \hat{E}_{MW} = \hat{x}$. (a) Arrows show allowed transitions in the system. For the simplicity of the explanation, the quantization axis for this case is considered to be in the $\hat{x}$-direction. Probe and coupling fields couple states with $\Delta m_F = \pm 1$, and MW couple states with $\Delta m_F = 0$. The stretched states in the $53D_{5/2}$ manifold are not coupled to the $54P_{3/2}$ manifold. (b) Schematic of the experimental setup indicating polarization and propagation direction of the three fields. (c) Experimental (black) and theoretical (red) results.

of the atoms are in these states, so the system exhibits both three and four level character. The comparison between experiment and theory is shown in Fig. 3.13.

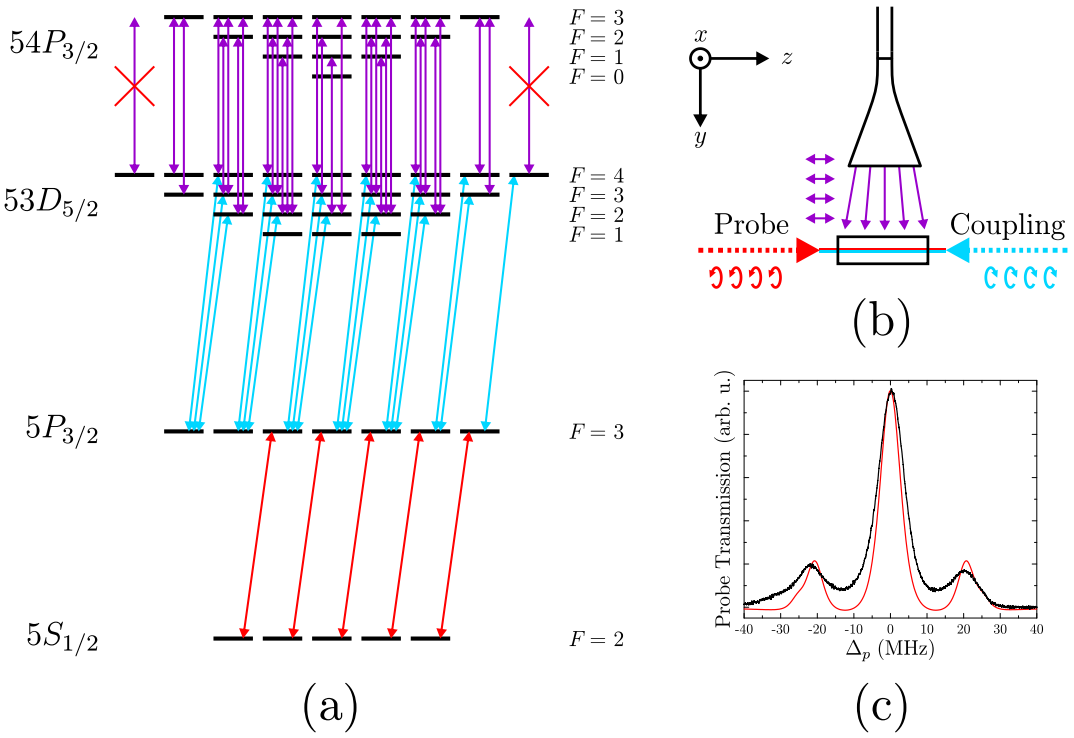

Figure 3.14: Case 3, $\hat{E}_p = \hat{E}_c = \frac{1}{\sqrt{2}}(\hat{x} - i\hat{y}), \hat{E}_{MW} = \hat{z}$. (a) Arrows show allowed transitions in the system. The probe and coupling fields couple states with $\Delta m_F = +1$. The MW field couple states with $\Delta m_F = 0$. The $53D_{5/2}, (F = 4, m_F = 4)$ state is not coupled to the $53P_{3/2}$ manifold. (b) Schematic of the experimental setup indicating polarization and propagation direction of the three fields. (c) Experimental (black) and theoretical (red) results.

In the third case, the system is almost entirely in a three level system. The lasers are both circularly polarized and couple σ^+ ($\Delta_m = +1$) transitions, while the microwaves are polarized along the z-direction coupling π transitions. By looking at Fig. 3.14, the lasers will optically pump most of the atoms

into the $F = 2, m_F = +2$ stretched ground state. The lasers will couple the $F = 2, m_F = +2$ ground state to the $53D_{5/2}, F = 3, m_F = 3$ state, which is not affected by the microwaves. The system has a large 3-level character but retains a small amount of 4-level character due to relative laser Rabi frequencies and transit-time broadening.

By analyzing these three cases, it is clear that the system is sensitive to the relative polarizations between the lasers and microwaves. The only difference between the results in Fig. 3.12 and Fig. 3.13 is that the polarization of both lasers is rotated 90°. Analyzing the signal for each case at $\Delta_p = 0$, the signal changes from 0 to a maximum value. The method for measuring the polarization of the microwaves is to analyze the probe transmission at $\Delta_p = 0$, as both lasers are rotated together with the same linear polarization.

3.2.3 Experiment and Results

The geometry needed to describe a measurement of the MW electric field polarization is shown in Fig. 3.15. The laser propagation direction is along the z-axis indicated by the red arrow. The microwave polarization is the purple arrow. The shadows are the projections of the microwave polarization onto the x-y plane on the left and the x-z plane in the back. Both lasers are linearly polarized along the direction of the blue arrow. During the measurement the polarizations of the laser are rotated together. The amount of rotation of the lasers from the x-axis is specified by angle ξ_z.

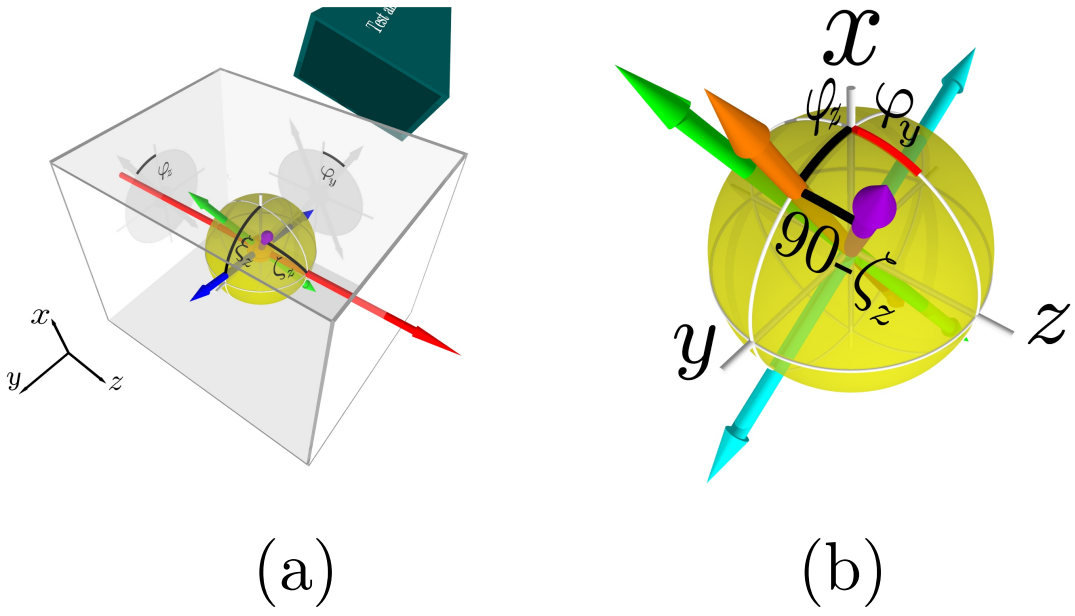

Figure 3.15: (a) Schematic of the experimental setup. The lasers propagate along the z-axis. From the horn antenna, the microwaves polarization is illustrated with the purple arrow. The laser polarization is indicated by the blue arrow. (b) Visualization of more polarization directions and angles needed to determine microwave polarization.

Any MW electric field can be split into two components. The first component lies along the laser propagation (z) axis, E_z. The second component is perpendicular to E_z, $E_{\perp z} = E_x + E_y$, and lies in the x-y plane, shown in orange. The angle between $E_{\perp z}$ and the x-axis is defined as φ_z. The angle between the microwave polarization and the z-axis is defined as ζ_z, and is a rotation around the axis shown in cyan, which is perpendicular to $E_{\perp z}$ in the x-y plane.

The experimental setup, as shown in Fig. 3.15, consists of the probe and

coupling lasers overlapped and counter-propagating inside a cuboidal atomic Rb cell with dimensions, $10\,\text{mm} \times 10\,\text{mm} \times 30\,\text{mm}$. Three pairs of orthogonal Helmholtz coils surround the cell to cancel the background geomagnetic field to a level of $< 0.1\,\text{G}$. The experiment is conducted at a Rb vapor cell temperature of 45°C. The temperature corresponds to a Rb vapor pressure of $2.6 \times 10^{-6}\,\text{Torr}$ which remains fixed throughout the experiments. The cell was heated to prevent significant condensation of Rb on the walls of the vapor cell. Condensation of Rb on the walls of the vapor cell causes reflections of the MWs leading to spurious signals.

The polarizations of the laser beams are adjusted and filtered using waveplates and Glan laser polarizers. The probe (coupling) laser spot size is 200 (65) μm and the power is 15 μW (11 mW). The corresponding probe (coupling) Rabi frequency is $2\pi \times 8.1 (2\pi \times 3.4)\,\text{MHz}$. Similar to the amplitude experiments, the intensity of the coupling laser is modulated at 40 kHz with an acousto-optic modulator and the probe transmission is detected on a photodiode. The photodiode signal is processed using a lock-in amplifier.

The MW electric field propagates along the y-axis ($\varphi_z = 0°$) and is linearly polarized. The polarization of the MW's is changed experimentally by rotating the antenna. Measurements are carried out for various laser and microwave polarizations. The results are shown in Fig. 3.16. The inset shows an example of the two of the measurements points with the microwaves polarized along $\zeta_z = 0°$. The points are experimental data, and are a result of 20 averages.

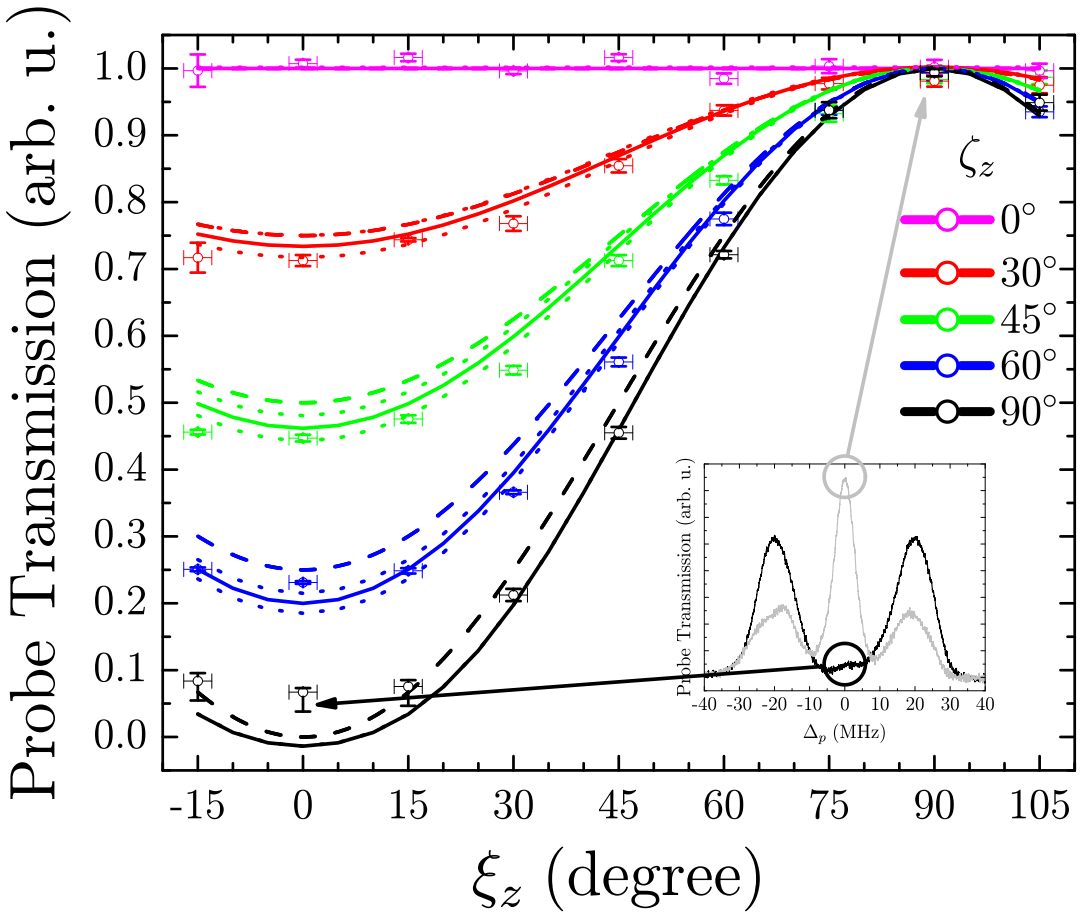

Figure 3.16: Probe transmission at zero detuning ($\Delta_p = \Delta_c = \Delta_{MW} = 0$), for varying laser and microwave polarizations. Each color represents data taken for the same microwave polarization. The inset shows the experimental traces for two of the measurements with $\zeta_z = 0$. The maximum transmission is normalized to 1, and all of the other values are scaled accordingly.

The vertical error bars for the experimental points are due to statistical errors in the measured peak height. The horizontal error bars are due to systematic uncertainty in ξ_z, i.e. the polarizations of the lasers. The solid lines are the result of the 53-state calculation, and the dotted lines are the result of the calculation with $\zeta \pm 1°$.

For each antenna polarization, the probe transmission oscillates between a minimum and maximum as the lasers are rotated. The minimum of a curve occurs when the system has the greatest 4-level character. This is the case when the laser polarization overlaps with $E_\perp$ (orange arrow). Therefore the position of the minimum of each curve determines φ_z. As the lasers are rotated the ratio of $E_{\perp z}/E_z$ changes, and the amplitude of the oscillation measures ζ_z. Measuring φ and ζ along all three cartesian coordinate axes yields the following information,

$$\begin{aligned}
\varphi_z &= \tan^{-1}\left(\frac{E_y}{E_x}\right), \qquad & \zeta_z &= \tan^{-1}\left(\frac{|E_{\perp z}|}{|E_z|}\right), \\
\varphi_x &= \tan^{-1}\left(\frac{E_z}{E_y}\right), \qquad & \zeta_x &= \tan^{-1}\left(\frac{|E_{\perp x}|}{|E_x|}\right), \\
\varphi_y &= \tan^{-1}\left(\frac{E_z}{E_x}\right), \qquad & \zeta_y &= \tan^{-1}\left(\frac{|E_{\perp y}|}{|E_y|}\right).
\end{aligned} \tag{3.18}$$

It is important to note that it is impossible to distinguish the angle ζ_i from $180° - \zeta_i$, e.g. the purple and green arrows in Fig. 3.15 for $i = z$, because these two cases differ only in the relative phase between E_i and $E_{\perp i}$. Measuring φ along another axis, e.g. φ_y, is theoretically sufficient to determine the MW electric field polarization, except for the case where the MW electric field polarization lies directly in the plane orthogonal to the 2 measurement axes. In this case,

the phase of E_z relative to E_y cannot be determined by referencing both to E_x, and measuring ζ_i provides no additional information. A measurement out of the plane determined by the 2 measurement axes is required. Additionally, the measurement becomes sensitive to noise if E_x is small and only φ_z and φ_y are used to determine the MW electric field polarization. As a consequence, it is best to measure φ_x, φ_y, and φ_z, provided no a priori knowledge of the MW electric field polarization is known. Note that in general, $\varphi_y \neq 90 - \zeta_z$ because the angles are rotations along different axes. The relationship between φ_y and ζ_z is,

$$\varphi_y = \tan^{-1}\left(\cot(\zeta_z)\sec(\varphi_z)\right). \tag{3.19}$$

A simplified model of the resonant probe transmission dependence on ξ and ζ can be obtained by considering the projection of the MW electric field vector $\vec{E}$ onto the probe and coupling laser polarization. From Fig. 3.15, the projection of the MW electric field on the laser polarization direction is $E_\parallel = |\vec{E}|\cos(\xi_z - \varphi_z)\sin(\zeta_z)$. Due to branching between the 3 and 4-level behavior, the resonant probe transmission can be approximated as,

$$T = 1 - (E_\parallel/|\vec{E}|)^2 = 1 - \cos^2(\xi_i - \varphi_i)\sin^2(\zeta_i). \tag{3.20}$$

$$T = 1 - \cos^2(\xi_z - \varphi_z)\sin^2(\zeta_z). \tag{3.21}$$

Curves using Eq. 3.21, with $\varphi_z = 0$ are shown as dashed lines in Fig. 3.16. The probe transmission is normalized such that the maximum theoretical transmission is one. The approximation neglects optical pumping and transit-time broadening

effects that occur in the full 53-state system and therefore does not completely reproduce the transmission amplitudes. However, the angular positions of the minima and maxima as ξ_z is varied are predicted accurately. The simplified model predicts the correct MW electric field polarization from a measurement of φ_i. To get the correct probe transmission amplitude, the full 53-state theory including optical pumping and Doppler averaging and transit time broadening needs to be used.

In order to unambiguously determine the MW polarization direction, measurements along multiple directions are needed. If the measurements are done along three orthogonal directions, the knowledge of φ_x, φ_y, and φ_z are enough to determine the direction of the polarization vector. The consequence of this is that the complex 53-state theory is not needed to analyze the results, only Eq. 3.21 is needed.

The maximum sensitivity of the measurement is when the 4-level peaks are completely split from the 3-level peak. For our experimental parameters this occurs at a MW electric field amplitude of $\sim 10\,\mathrm{mV/cm}$. Increasing the MW electric field strength has little effect on the central peak until $\sim 100\,\mathrm{mV/cm}$. At this point, the peak starts to shift and decrease in height, most likely due to multi-photon transitions. In the measurement, the maximum sensitivity of ζ_z is when $\zeta_z \sim 45°$. At this angle the angular resolution detected in the experiment is $\sim 0.5°$ in both ζ and φ. The angular resolution of $\sim 0.5°$ is derived from a least squares fit of each trace to the theory.

3.3 Conclusions

To summarize, the amplitude and polarization of microwave fields at 14.3 GHz were measured. Taking advantage of electric dipole transitions at MW frequencies in ^{87}Rb Rydberg atoms, improvements over traditional antenna measurements have been made. In traditional measurements with dipole antennas, the lowest measurable field is $\sim 1\,\mathrm{mV/cm}$ [83]. The experiments take place in vapor cells at room temperature in a setup that is conducive for miniaturization. Electric field amplitudes were measured in the range of $0.008 - 30\,\mathrm{mV/cm}$. The main source of error in these experiments is noise due to laser frequency and amplitude fluctuations, which in principle can be improved. With modest improvements in the experimental apparatus, the limiting factor in the measurements will be the determination of the dipole moments. Hopefully advances in microwave measurements will spur other researchers to extend the accuracy of the dipole moments.

In addition to the amplitude measurements, the polarization of the microwave field was also measured. The measurement takes advantage of the energy level structure when $|3\rangle \rightarrow |4\rangle$ is a $\Delta L = -1$ transition. The MW field is mapped onto the laser polarizations, and by taking data with different laser polarizations the direction of the microwave field can be determined.

The general methods used in this chapter can be extended to other atoms and other frequency ranges. Since these results, experiments have been carried out

with ^{85}Rb and ^{133}Cs over a range of frequencies from $2 - 100\,\mathrm{GHz}$ [83, 84, 85, 86]. Furthermore, using Rydberg atom EIT with MWs driving a two-photon transition electric fields up to $2300\,\mathrm{mV/cm}$ have been measured [87].

Chapter 4

Experimental Setup

In this chapter, the experimental apparatus for measuring the electric fields near a quartz surface is detailed.

4.1 Vacuum System

Surface experiments are performed in an ultra high vacuum (UHV) system shown in Fig. 4.1. The system consists of a main chamber where all of the experiments take place, and two pumps to achieve UHV pressures. The pressure in the chamber during experiments is 3×10^{-10} Torr. The two vacuum pumps are a 100 L ion pump (Gamma Vacuum), and a non-evaporable getter pump (CapaciTorr D 400-2). The ion pump is sufficiently far away from the chamber so that the magnetic fields from its magnets do not disturb experiments. Also, there no direct line of sight from the ion pump to the experimental chamber preventing ions from interacting with Rydberg atoms. The gate valve is used to connect a pumping station for initially pumping the system down from atmosphere.

4.2 Experimental Timing

The timing and control of the experiment is done using two PCI data acquisition boards, NI PCI-6254 and NI PCI-6723. The cards generate voltages at specific

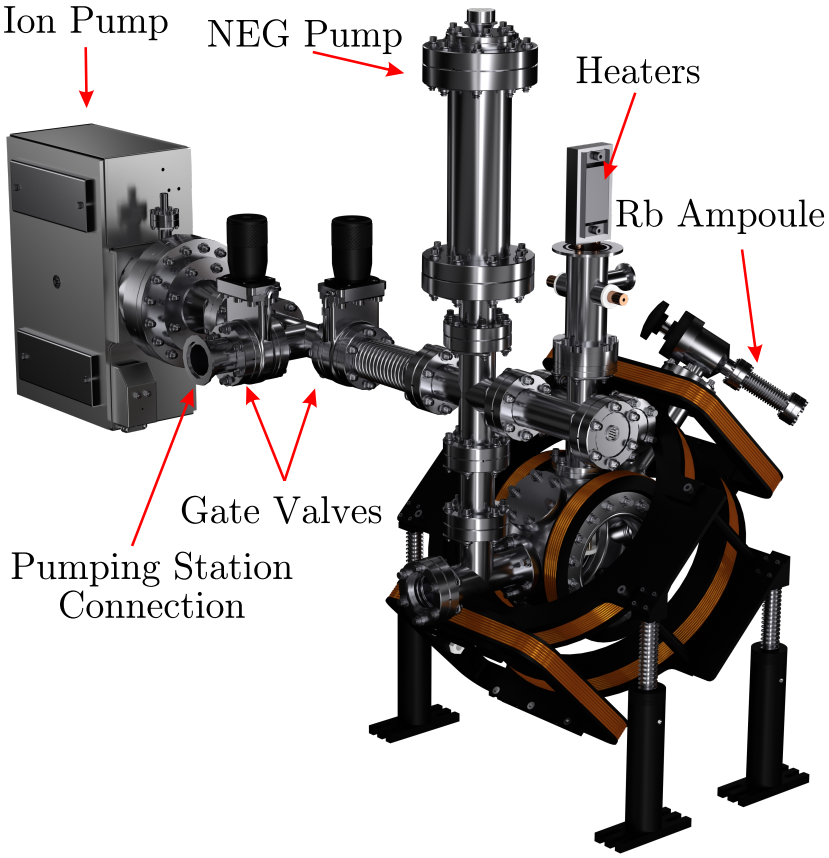

Figure 4.1: The vacuum system and experimental chamber used for surface experiments. An ion pump and non-evaporable getter (NEG) pump are continuously pumping on the system. The source of Rb for the experiments is an ampoule inside of a flexible coupling with a valve to control the Rb pressure inside the chamber. The gate valve on the left allows for the connection of a pumping station, which is used when first pumping down the system from an atmosphere of pressure.

times to control many aspects of the experiment including, changing magnetic fields, changing laser frequencies, shutters, etc. The experiment runs on a 10

second cycle.

The NI PCI-6254 outputs digital signals and the NI PCI-6723 card outputs analog signals. The output of the digital card is either 0 or 5 V, and the output of the analog board has a maximum of 10 V and a minimum of −10 V. The two cards are connected together with a ribbon cable and share the same clock. The clock runs at 100 kHz and the timing resolution of the output signals is 10 μs. The signals are routed from the back of the computer to custom made primary break out boards. From the primary breakout boards the signals are routed to the experiment using Cat 5 cables. With 4 twisted pairs each cable can carry up to 4 different signals. The ethernet cables are plugged into custom made secondary break out boards around the lab. On the secondary boards each signal can be routed to either a BNC bulkhead, a set of terminals capable of connecting a twisted pair, or both.

A program written in C++ is used to control both DAQ cards. The program is capable of loading and saving pulse sequences.

4.3 Magnetic Field Coils

The magnetic field coils surrounding the main chamber are shown in Fig. 4.2. There are three pairs of coil frames and 4 pairs of coils. Three sets of the coils are wound in a Helmholtz configuration and are labeled x, y, and z. The magnetic fields generated from these coils are orthogonal to each other, so any arbitrary

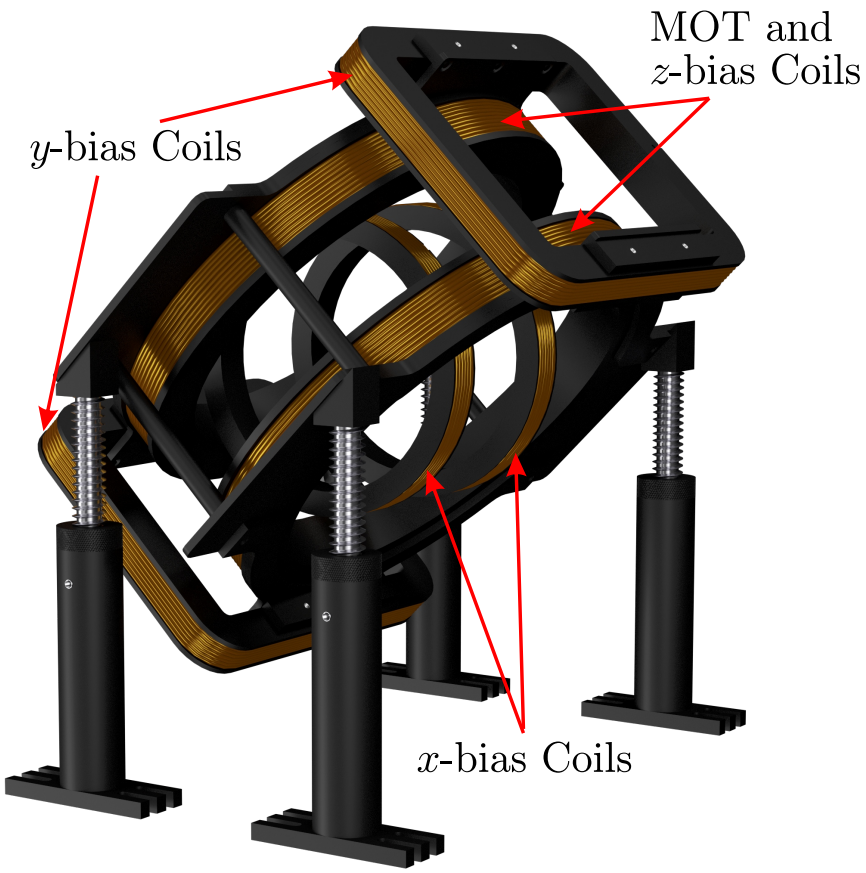

Figure 4.2: The 4 pairs of magnetic field coils used in the experiment.

direction of magnetic field can be applied to the atomic region. There is a second pair of windings on the z-coils, and these are configured as anti-Helmholtz coils to generate the quadrupole field needed for the MOT.

4.3.1 Bias Coils

All power supplies for the magnetic field coils are operated in constant current mode. Current through the bias coils is controlled by Kepco BOP 20-20M power supplies. The x and z-coils are controlled by one power supply each. The y-bias

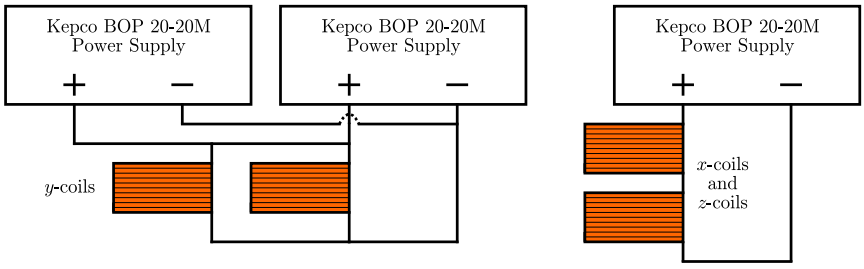

Figure 4.3: A schematic of the circuits used to control the bias coils.

coils have a high inductance and are connected in parallel instead of series. The total inductance decreases by a factor of 4, allowing for faster switching times. Two power supplies are connected in parallel to drive the coils to provide the necessary current. A schematic of the two circuits is shown in Fig. 4.3.

4.3.2 MOT Coils

A Sorenson DCS-80-37 power supply provides 24 amps of current to the MOT coils as shown in Fig. 4.4. Current is running through the coils while the MOT is loaded, but is switched off when the magnetic trap is loaded and the imaging is performed. The current is switched off fast using a circuit that is depicted in Fig. 4.4. An insulated-gate bipolar transistor (IGBT) is used to turn on and off the current. A series of transient voltage suppressors and resistors are used to dissipate the large voltage spike present from the large inductive load.

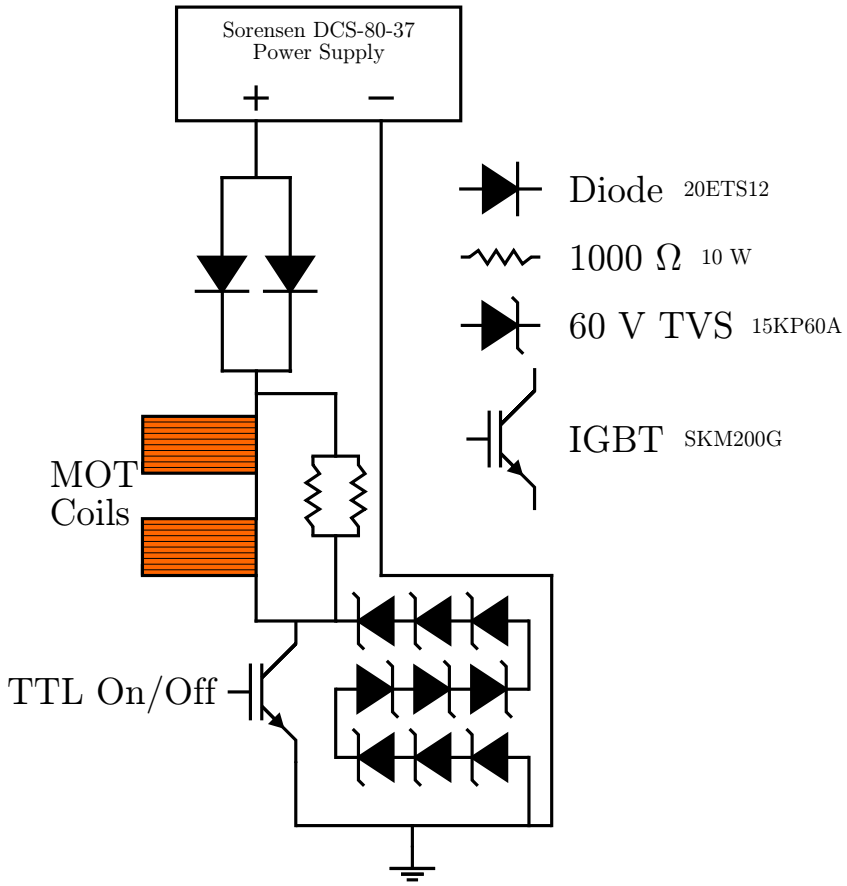

Figure 4.4: A schematic of the circuit used to switch current on and off in the MOT coils. The resistors in parallel with the MOT coils help to dampen the initial voltage spike after the turn off of the current.

4.3.3 Coil Switching

Current through the coils needs to be turned on and off fast. Using signals from the PCI boards, the current through the coils can be controlled. Fig. 4.5 shows the switching on and off of the current in the coils during the loading phase of the magnetic trap. The current in the MOT coils is shut off in $< 500\,\mu$s. Current

Table 4.1: Coil Parameters. The values were measured with the coils connected in series.

Coil Pair	R (Ω)	L (mH)	B-Field
MOT	0.58	1.2	n.a.
X-Bias	0.84	0.56	4.6 G/A
Y-Bias	1.26	0.78	1.05 G/A
Z-Bias	0.6	0.21	0.95 G/A

through the bias coils is switched on in < 1 ms with the y-bias taking the longest to turn on because of its high inductance.

4.4 Rb Source

The rubidium used in the experiment is provided by an ampoule of rubidium that is broken inside a flexible coupling, as shown in Fig. 4.1. The flexible coupling is kept at room temperature and the valve is opened a variable amount to adjust the Rb pressure inside the chamber.

4.5 Substrate Mount

The quartz-mount consists of 4 pieces: an aluminum nitride mount, copper Z-wire, gold mirror, and the quartz substrate. An exploded view of the system is shown in Fig. 4.6. We use a $20 \times 20 \times 0.5$ mm piece of single crystal quartz. The quartz is z-cut with the (0001) direction perpendicular to the surface. The surface of the quartz was polished and has a surface roughness of < 5 Å.

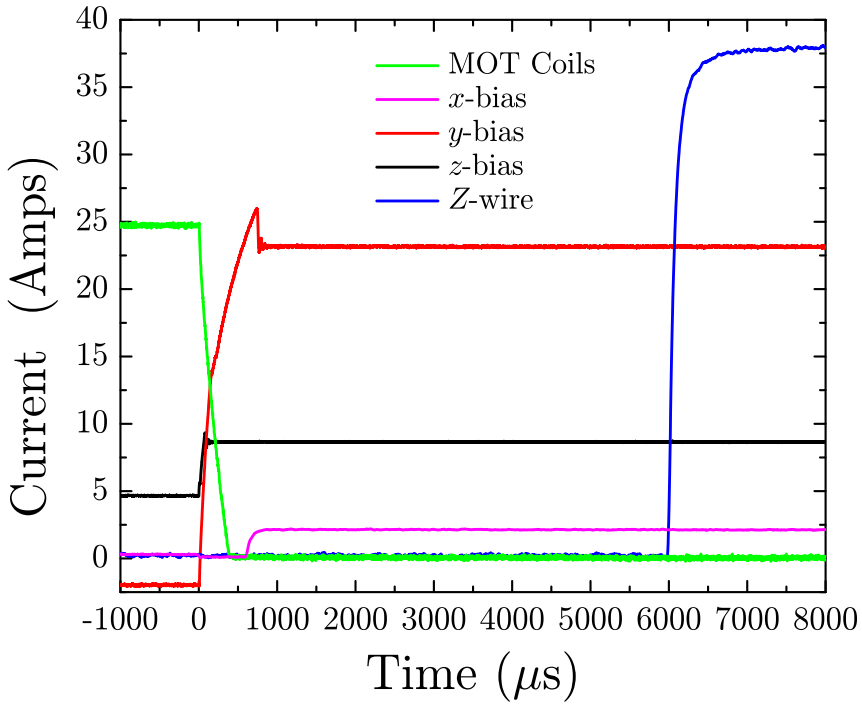

Figure 4.5: Measurements of the current in the coils and Z-wire during the experimental sequence.

The quartz is mounted to a gold mirror, Edmund Optics NT32-433. From the manufacturer the mirror has dimensions of $22 \times 22 \times 5$ mm. The mirror is cut so that it will fit into the 13×22 mm key of the aluminum nitride mount. The thickness is reduced $\sim 700\,\mu$m by cutting and polished the back of the mirror.

A thermally conductive, electrically isolating, and low outgassing epoxy Epo-tek H77 was used to bond the Z-wire to the AlN mount, attach the mirror to the mount and the quartz to the mirror. Several pictures of the mount during the assembly process are shown in Fig. 4.7.

The quartz is in thermal contact with resistive heaters positioned outside

Figure 4.6: An exploded view of the quartz mount.

the vacuum chamber. The temperature of the quartz is monitored with a thermocouple attached to the quartz surface, but far away ($\sim 14\,\mathrm{mm}$) from the Z-trap. A picture of the assembled mount ready to be placed in the chamber is shown in Fig. 4.7 (d).

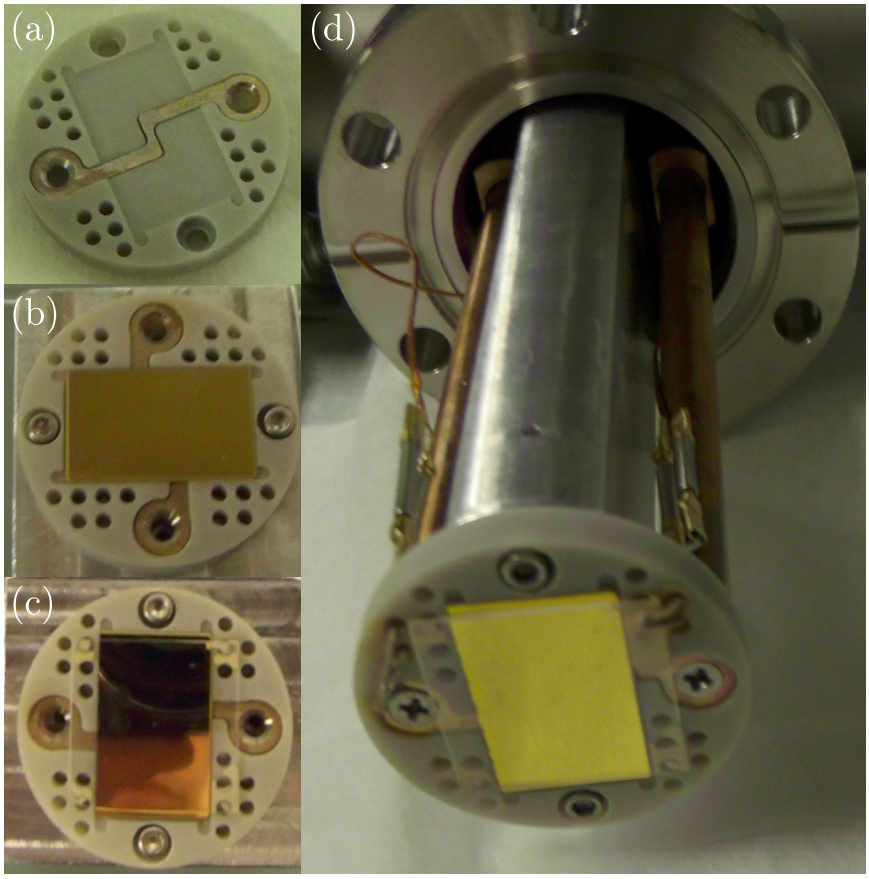

Figure 4.7: A picture of the quartz mount at several points during the assembly process. (a) The Z-wire epoxied into the aluminium nitride mount. (b) The gold mirror is epoxied into the key of the aluminum nitride mount above the Z-wire. (c) The quartz is epoxied to the aluminum nitride mount on top of the gold mirror. (d) Fully assembled mount with thermal couples attached to the mount.

4.5.1 Z-wire

Current traveling through the Z-wire generates part of the magnetic field for the magnetic trap. The circuit for controlling the current in the Z-wire is illustrated

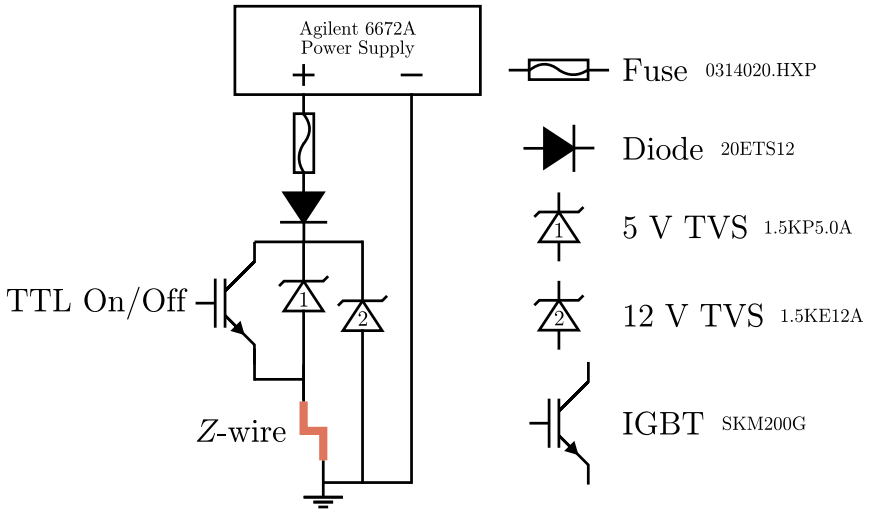

Figure 4.8: Schematic of the circuit used to control the current in the Z-wire.

in Fig. 4.8. The circuit is similar to Fig. 4.4 with some important differences. A stack of TVSs is not needed for fast shutoff times. The inductive load through the circuit is negligible because there are no coils in the system. The Z-wire is positioned after the IGBT in the circuit, so that when the gate is open and no current is flowing through wire, the voltage on the Z-wire is zero. A voltage on the Z-wire creates an electric field in the region containing cold atoms and Stark shifts the energy levels of Rydberg states, creating problems during experiments. In order to achieve fast switching times needed for experiments, the power supply is operated in constant voltage mode. If too much current travels through the Z-wire, thermal expansion of surrounding components causes damage. To prevent this a fast acting fuse is used.

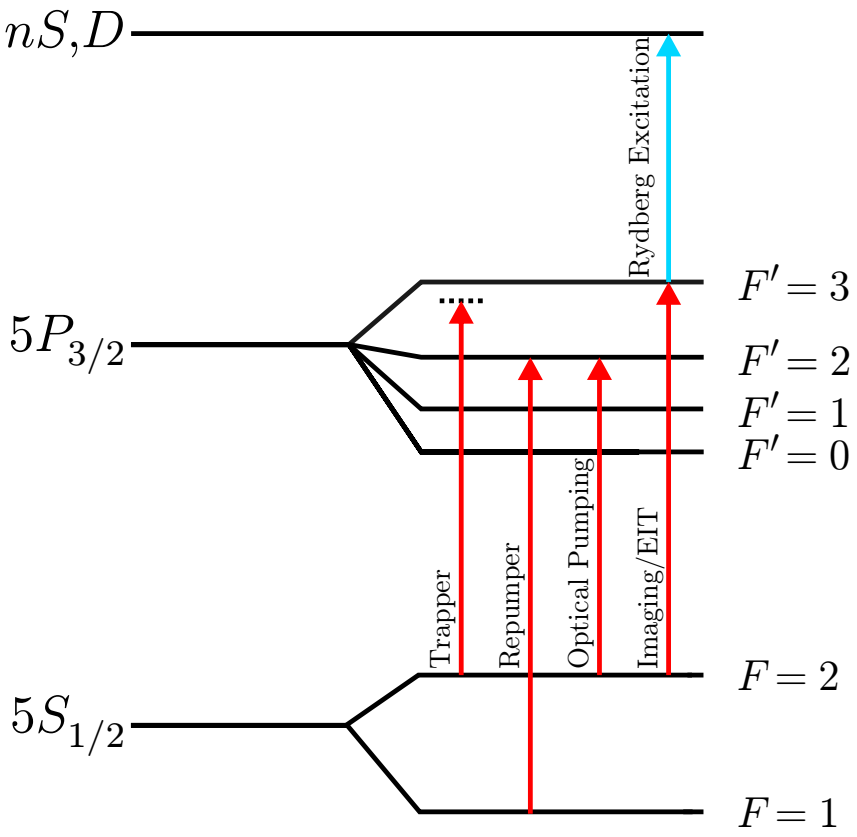

Figure 4.9: Energy level diagram of the states used in these experiments and the lasers used to couple them.

4.6 Lasers

To cool, trap, and probe atoms near the quartz surface, 4 laser systems are used. Three of the laser are operated at $\sim 780\,\text{nm}$. The fourth laser is operated at $\sim 960\,\text{nm}$ and is frequency doubled to $\sim 480\,\text{nm}$ and is used for Rydberg excitation. A diagram showing the different laser frequencies is shown in Fig. 4.9.

4.6.1 Trapper

Light at the trapping frequency is generated by a commercial external cavity diode laser (Toptica DL 100). A schematic of the optical system is shown in Fig. 4.10. The frequency is stabilized using FM spectroscopy [88] of a saturated absorption [89] signal generated in a vapor cell. The modulation and demodulation are carried out by the Digilock module. The current of the laser is modulated at 10 kHz. The saturated absorption and FM spectroscopy signals are shown in Fig. 4.11. The laser is locked to the $F' = 1, 3$ crossover transition. An acousto-optic modulator (AOM) is used to control the intensity and frequency of the light during the experiment. The light is passed twice through the AOM and the total frequency shift is +197 MHz. The trapping frequency is detuned −15 MHz from the $F = 2 \leftrightarrow F' = 3$ transition, and was experimentally optimized to maximize the density of the MOT.

4.6.2 Repumper

During the MOT loading process, the trapping laser excites a small fraction atoms into the $F' = 2$ state. From this state atoms radiatively can decay into either $F = 1$ or $F = 2$ ground state. A repumper is used to transfer atoms back into the $F = 2$ ground state so they can be further cooled by the trapping laser.

The repumping laser is a homebuilt external cavity diode laser. The optical system for the repumper is illustrated in Fig. 4.12. The laser is locked to the

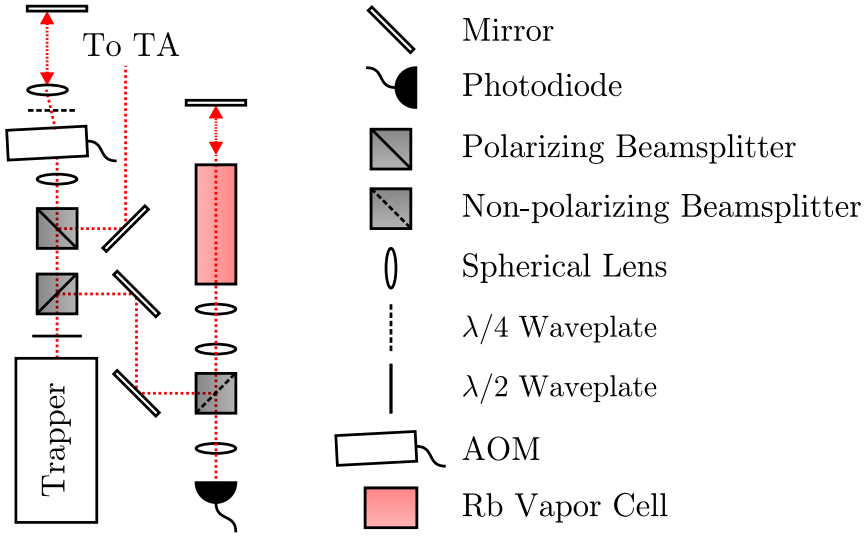

Figure 4.10: Schematic of the optical system used to generate trapping beam.

saturated absorption signal using a field programmable gate array (FPGA) [90]. A FPGA is a set of digital gates that are programmed to generate the feedback signals to stabilize the laser. FPGAs have advantages of fast response with clock speeds of $\sim 100\,\mathrm{MHz}$, rapid reconfigurability as experimental needs change, and easily scalable to produce duplicate systems.

The FPGA generates the feedback signals based on the input of the saturated absorption signal that is digitized using an analog to digital converter (ADC). The ADC accepts a signal from 0 to $3.3\,\mathrm{V}$, so the saturated absorption signal is adjusted to fit within the window. The FPGA generates feedback signals using a proportional-integral-derivative (PID) algorithm. The feedback is split into two parts, one that controls the piezo and adjusts the position of the grating, and one that controls the current. A digital to analog converter (DAC) converts the

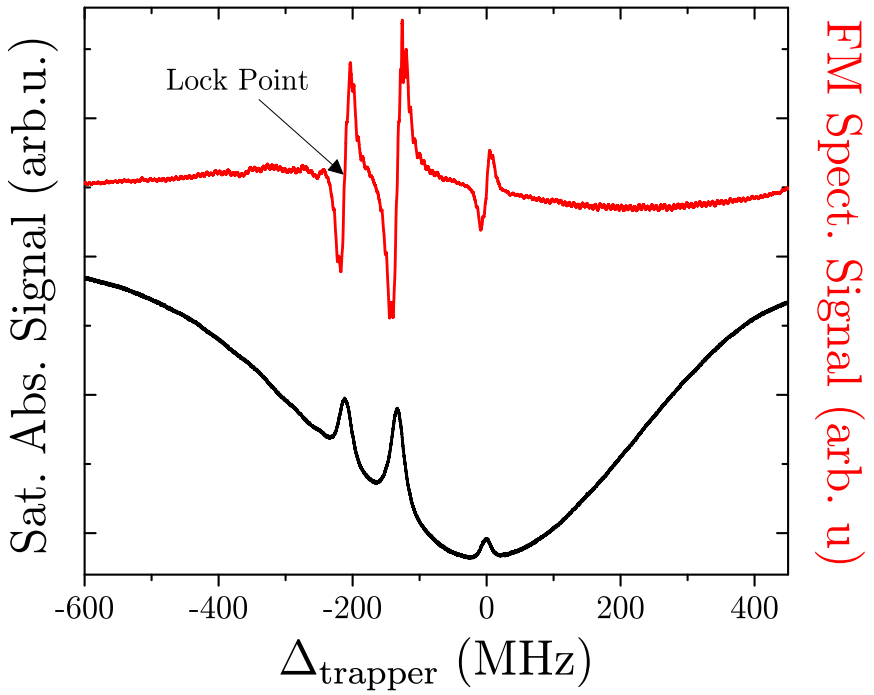

Figure 4.11: Saturated absorption (black) and FM spectroscopy signal (red) used for locking the trapper.

digitally generated feedback into an analog signal. The DAC outputs a voltage from 0 to 3.3 V. The low frequency < 500 Hz feedback is sent to the piezo, while the high frequency > 500 Hz feedback is sent to the current.

Additional analog circuits are needed to process the feedback signals. The low frequency feedback is added to a dc offset in a homebuilt circuit Fig. 4.13a. The switches on the circuit give the option of amplifying the signal from the FPGA by a factor of 1 or 6.7. The frequency of the laser can be scanned by a ramp that is generated by the FPGA, and the extra amplification is used when scanning over large frequency range is desired. Feedback for the current of the

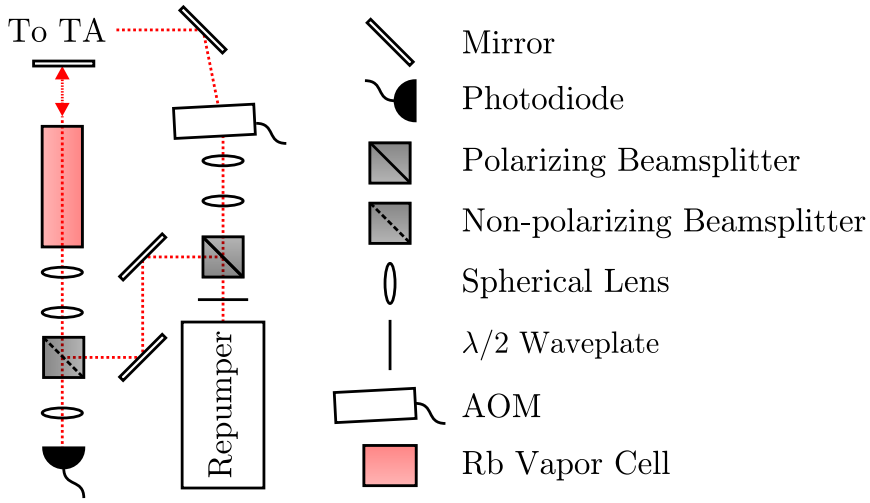

Figure 4.12: Schematic of the optical system used to generate repumping beam.

laser diode is added onto an external dc voltage that controls the current of the diode. The laser diode is controlled by a commercial laser diode controller (Wavelength LDTC0520). A schematic for combining both signals is shown in Fig. 4.13b. The dc voltage is controlled with a potentiometer, and the ac part of the feedback is added onto the signal through a transformer.

The frequency is stabilized to the side of the $F' = 0, 2$ saturated absorption peak and is shifted by a single passed AOM by $+111\,\mathrm{MHz}$, so that the laser is on resonance with the $F = 1 \leftrightarrow F' = 2$ transition.

4.6.3 Tapered Amplifier

To increase the power of the trapping and repumping beams, they are combined in a tapered amplifier (TA) as illustrated in Fig. 4.14. The two beams are combined using a 90:10 non polarizing beam splitter. 90% of the trapping beam and 10%

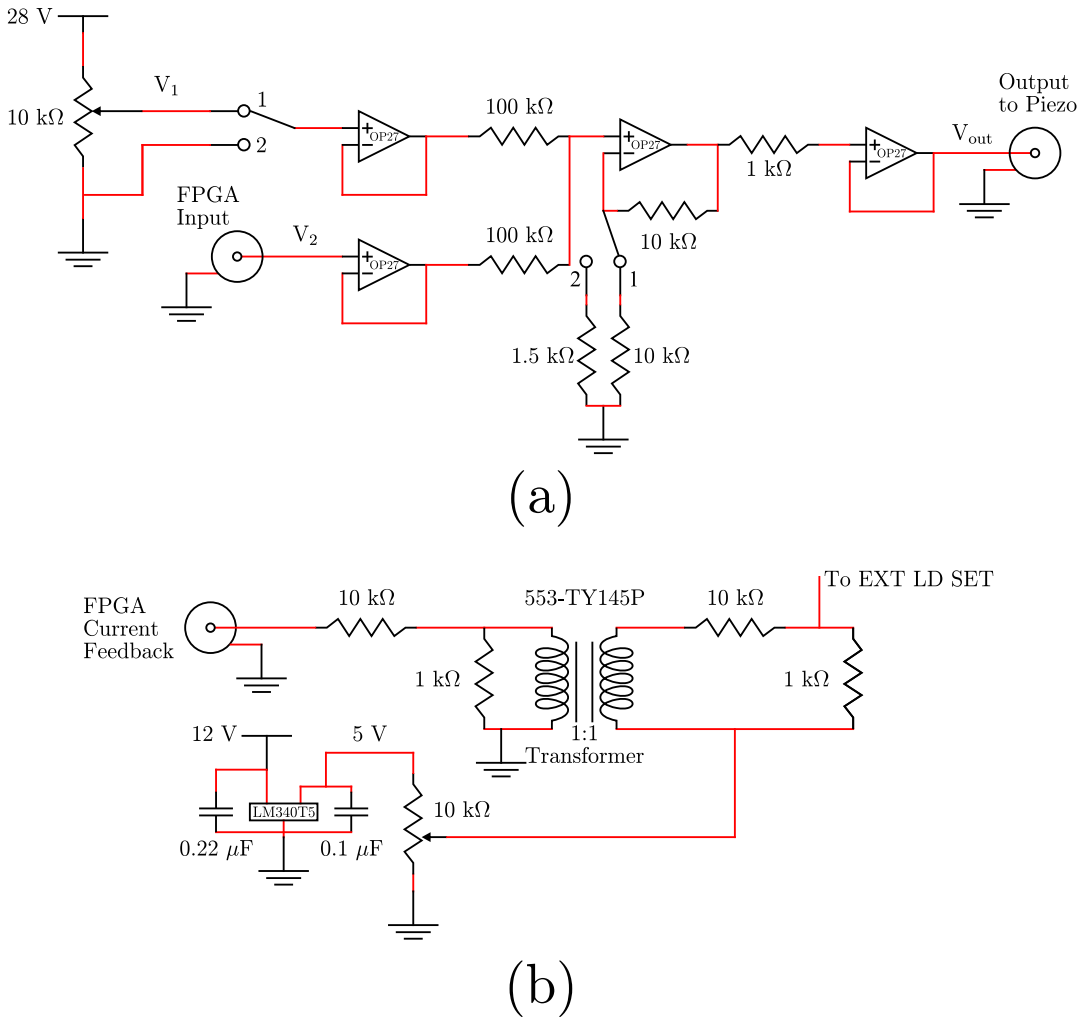

Figure 4.13: Circuits used in processing the feedback signals for the (a) piezo and (b) laser diode current. For the circuit in (a), there is a double-pole, double-throw (DPDT) switch. If the switch is in position 1, then $V_{out} = V_1 + V_2$. If the switch is in position 2, $V_{out} = 6.66V_2$.

of the repumping beam are combined into a polarization maintaining fiber. The other end of the fiber and the optical setup of the TA is on a separate breadboard. After exiting the fiber, the light seeds the TA. The system is homebuilt using a TA from m2k Laser (m2k-TA-0780-1000-CM). Light is coupled into and out of

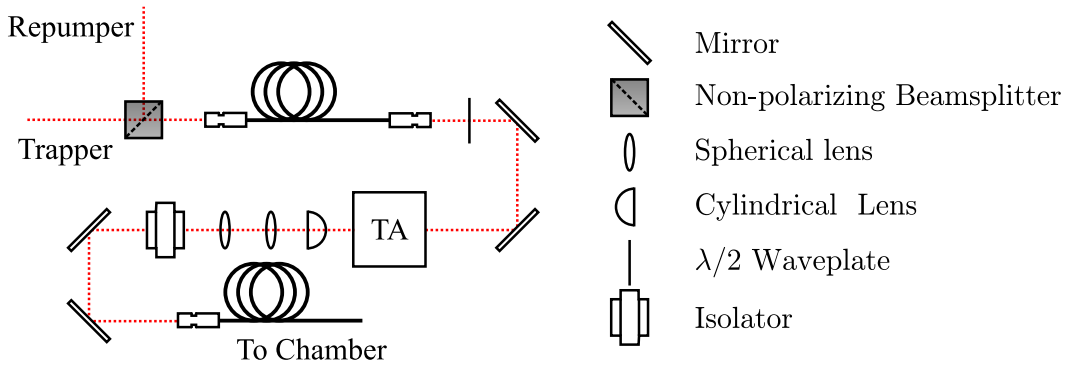

Figure 4.14: Schematic of the optical setup of the tapered amplifier used to amplify the trapping and repumping beams.

the tapered amplifier, using aspheric lenses (C330TMD-B). Alignment of the TA is done by overlapping the seed beam with the light that propagates out of the input facet of the TA. The light from the TA is collimated by the aspheric lens, and the size and position of the seed beam is adjusted to maximize the output power of the TA. The output of the TA is highly asymmetric, so the collimation of the beam is done in two stages. The asphere collimates the beam in the vertical direction and a cylindrical lens is used to collimate the beam in the horizontal direction.

4.6.4 Probe Laser

The first part of the Rydberg excitation is done with a 780 nm laser that is similar to the trapping laser. The laser is a Toptica DL 100 ECDL. The difference between this laser and the trapping laser is that laser diode has an anti-reflection

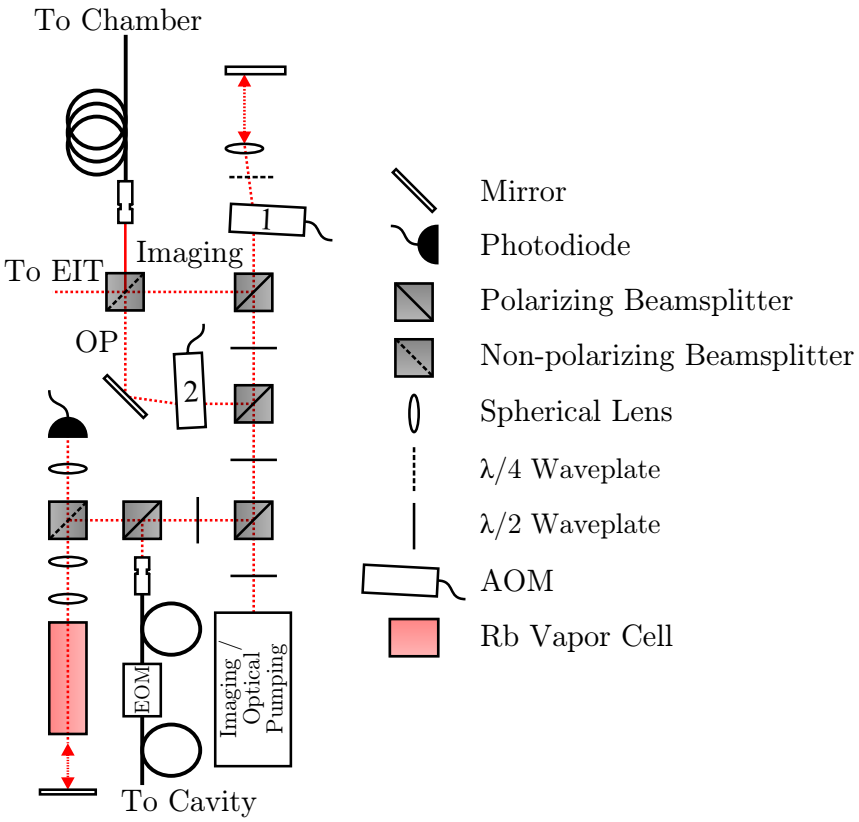

Figure 4.15: Schematic of the optical system used to generate the imaging and optical pumping beams. AOM 1 is double passed and shifts the light $200 - 220\,\mathrm{MHz}$, depending on the frequency needed. AOM 2 is single passed and shifts the light $-67\,\mathrm{MHz}$.

coating on the output facet (Eagleyard EYP-RWE-0780-02000-1300-SOT12-0000). The main advantage of the anti-reflection coating is to reduce mode competition between the cavity created with the output facet and the external cavity. This resulted in much less noise in the locking signal (see Section 4.6.6).

A schematic of the optical setup for the imaging laser is shown in Fig. 4.15. The laser is locked to a Fabry-Pérot cavity as described in Section 4.6.6. A

saturated absorption setup is used to reference the Fabry-Pérot fringes to the atomic transition frequencies.

Two beams with different frequencies are derived from this laser using AOMs. The first frequency is used for imaging the atomic cloud. It is tuned to the $5S_{1/2}\,(F = 2) \leftrightarrow 5P_{3/2}\,(F' = 3)$ frequency for imaging the MOT in zero magnetic field. The frequency can be shifted using the AOM to also image the magnetic trap with a background magnetic field. The imaging is done on the $5S_{1/2}\,(F = 2,\, m_F = 2) \leftrightarrow 5P_{3/2}\,(F' = 3,\, m'_F = 3)$ transition.

The second frequency of light derived from this laser beam is the optical pumping beam. This frequency drives the $5S_{1/2}\,(F = 2) \leftrightarrow 5P_{3/2}\,(F' = 2)$ transition. Driving this transition is used to optically pump atoms into the $5S_{1/2}\,(F = 2,\, m_F = 2)$ state as described in Section 5.2.1.

The two frequencies are linearly polarized in the same direction before being combined using a non-polarizing beam splitter. They are coupled together into a polarization maintaining fiber. After the fiber they are circularly polarized using a $\lambda/4$ waveplate and directed into the chamber. The system is setup to ensure that both beams are overlapped inside the chamber and have the same polarization.

Part of the imaging light is transmitted through the non-polarizing beam splitter and is directed to a separate Rb vapor cell on the table. Rydberg atom EIT is done in the cell with the 480 nm light to check the frequency of the coupling laser.

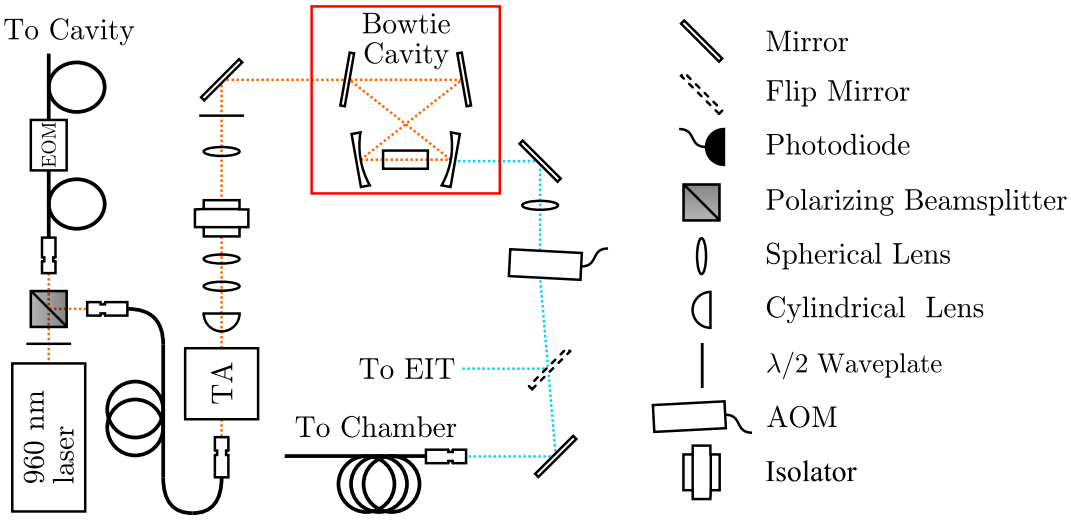

Figure 4.16: Schematic of the laser system used to generate the coupling beam. The flip mirror is used to switch between using the coupling beam for diagnostic Rydberg atom EIT in a vapor cell, and sending the light to the chamber for surface experiments.

4.6.5 Coupling Laser

Coupling the $5P_{3/2}$ state to a Rydberg state is done with $\sim 480\,\text{nm}$ light. Due to the lack of high power laser diodes in the visible, and the inconveniences of dye lasers, second harmonic generation (SHG) was chosen to generate the 480 nm light. Laser light from a 960 nm ECDL is amplified by a TA, and is sent into a bow-tie cavity as shown in the schematic in Fig. 4.16. The setup of the TA is the same as in Section 4.6.3.

Second harmonic generation (SHG) is the process of converting coherent light at frequency ω to frequency 2ω by passing it through a medium with a $\chi^{(2)}$ nonlinearity such as a crystal. Classically, the process can be thought of as

the incident light oscillating at frequency ω causing dipoles inside the crystal to oscillate and radiate at 2ω.

If the light at 2ω is generated randomly throughout the crystal, it will be subject to destructive interference. Phase-matching the crystal to the incident light will cause constructive interference and larger powers of the second harmonic will be generated. Theoretically the efficiency of SHG, η_{SHG}, the ratio of second harmonic power to the incident power, can be calculated using the plane wave approximation [91]

$$\eta_{\text{SHG}} = \frac{P_{2\omega}}{P_\omega} = \frac{8\pi^2 d^2 L_c^2 P_\omega}{n_\omega^2 n_{2\omega} c\epsilon_0 \lambda_\omega^2 A} \text{sinc}^2\left(\frac{\Delta k L_c}{2}\right), \tag{4.1}$$

where ω is the frequency of the fundamental, d is the nonlinear coefficient, L_c is the crystal length, n is the index of refraction, and P_ω/A is the intensity of the fundamental. The sinc^2 term is the phase-matching term. This analysis is correct for plane waves with no pump-depletion, and is sufficient for these purposes. For a more exact treatment with focused gaussian beams and pump depletion, Boyd-Kleinmann analysis is used [92].

SHG can be done using several different phase-matching schemes along with different polarizations of light, see for example, [93, 94, 95]. The wavevector mismatch Δk is [94]

$$\Delta k = k_{2\omega} - 2k_\omega \tag{4.2}$$

The two most common types of phase-matching are perfect or exact phase-matching, and quasi-phase-matching. In the case of perfect phase-matching

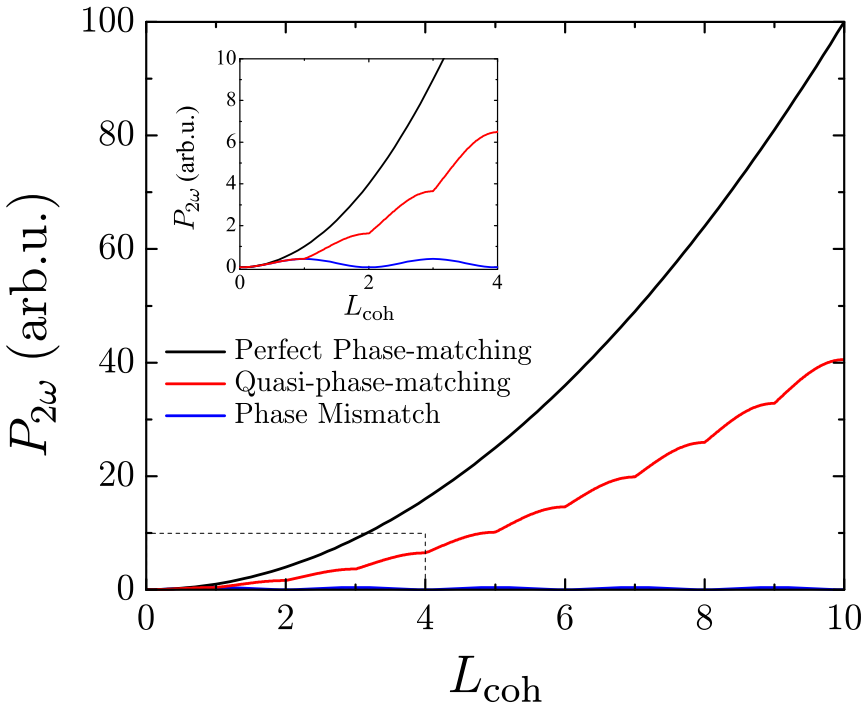

Figure 4.17: Second harmonic powers generated for several different phase-matching schemes. The x-axis is the number of coherence lengths, L_{coh}. The inset is plotting the boxed region.

$\Delta k = 0$, $P_{2\omega}$ increases quadratically across the crystal as shown in black line of Fig 4.17. To achieve perfect phase-matching for parallel k's the index of refraction n at ω and 2ω need to be equal. Most often birefringent phase-matching is used. For non-parallel wavevectors angle tuning can be used [95].

If the perfect phase-matching condition is not satisfied, there will be a wavevector mismatch of Δk. In this case, the second harmonic power will oscillate from a maximum at $\Delta k = \pi/L_{\mathrm{coh}}$ to a minimum of zero at $\Delta k = 2\pi/L_{\mathrm{coh}}$, and will repeat periodically though the crystal as shown in the blue curve of Fig 4.17.

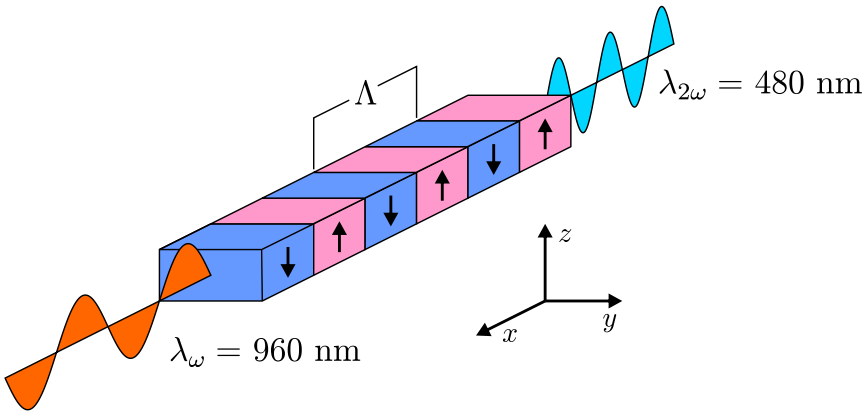

Figure 4.18: An illustration of the SHG process with a periodically poled material. All of the waves are polarized along the z-axis. The direction of the nonlinear coefficient d, is flipped every $\Lambda/2$.

The power inside the crystal increases until the coherence length $L_{\text{coh}} = \pi/\Delta k$. This effect is exploited in quasi-phase-matching.

Achieving perfect phase-matching and high conversion efficiency at a desired wavelength, in our case ~ 480 nm, is challenging without extreme experimental conditions. To get around this problem quasi-phase-matching (QPM) is used. Typically the coherence length is small (on the order of microns), so using a crystal the size of the coherence length is not practical or efficient. In QPM, the sign (or direction) of the nonlinearity is flipped every coherence length. Before $P_{2\omega}$ is about to decrease, the sign of the nonlinearity is flipped, which is equivalent to a π phase shift in the wavevector mismatch. The phase shift effectively resets the wavevector mismatch, so $P_{2\omega}$ monotonically increases throughout the crystal. This can be seen by looking at the red line in Fig. 4.17. QPM is equivalent to

perfect phase-matching with a reduced nonlinear coefficient $d_{\text{eff}} = 2d/\pi$ [96]. For a given non-linear coefficient, quasi-phase-matching will never outperform perfect phase-matching. However, quasi-phase-matching allows the use of materials with a higher d at wavelengths where perfect phase-matching cannot be obtained.

A schematic of the crystal is shown in Fig. 4.18. The crystal is grown using a process called periodic poling. A large electric field pointing in opposite directions is applied to different regions of the crystal as it is grown. The crystal we are using is PPKTP (periodically poled potassium titanyl phosphate), with a polling period of $\Lambda = 2L_{\text{coh}} = 6.375$ μm. The period was chosen so that with temperature tuning (explained later), quasi-phase-matching can be achieved for wavelengths $\sim$ 478-481 nm under standard laboratory conditions. This allows us to excite Rydberg states with $n > 30$. The crystal (manufactured by Raicol) is 20 mm long, and the ends of the crystal are anti-reflection coated at 960 and 480 nm. The efficiency of SHG increases with the crystal length as can be seen in Eq. 4.1, so theoretically a longer crystal is desired. However, the homogeneity of the periodic polling decreases with the length, so 20 mm is typically the longest crystal that Raicol will periodically pole at the time of production. In this setup we use Type I SHG with quasi-phase-matching, where the polarization of each wave is along the z-axis [97].

Evaluating Eq. 4.1 for the experimental parameters of $d_{\text{eff}} = 8.5\,\text{pm/V}$, $P_\omega = 1\,\text{W}$, yields a theoretical efficiency of $\sim 1.5\%$. Experimentally the single

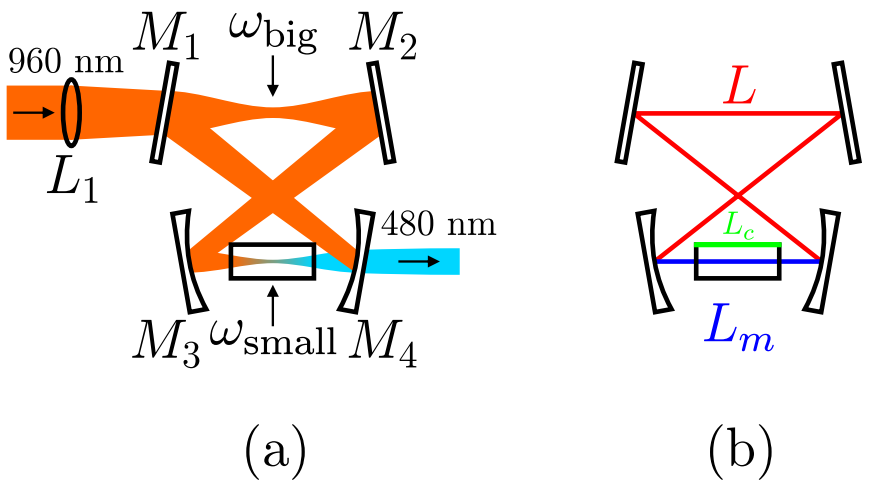

Figure 4.19: Diagrams of bow-tie cavity. (a) The 960 nm laser beam inside the cavity has two waists, ω_{big}, and ω_{small} and traces out a path that resembles a bow-tie. (b) Illustrates the three important lengths of the cavity design. L is the path length for the beam between the curved mirrors, bouncing off the flat mirrors. L_m is the path length between the curved mirrors, passing through the crystal. L_c is the length of the crystal.

pass efficiency η_{SHG} is $\sim 1\%$, 10 mW of 480 nm light is generated with 1 W of input power at 960 nm. 10 mW at 480 nm is not enough power to generate the Rabi frequencies needed to carry out experiments. To increase the efficiency of SHG and blue power, a bow-tie cavity is used. Experimentally, cavities of this type using PPKTP have achieved conversion efficiencies as high as 75% [98].

Inside the cavity the fundamental power is amplified, which will increase η_{SHG} as it scales linearly with P_ω. A schematic of the bow-tie cavity is shown

in Fig. 4.19. The basics of the cavity are as follows. The fundamental light enters the cavity through a partially reflective mirror M_1. The curved mirror M_3 focuses the beam in the center of the crystal. M_4 refocusses the fundamental light while allowing the second harmonic to pass through and exit the cavity. The fundamental light that remains in the cavity is reflected back onto M_1. In a stable configuration for a TEM_{00} laser beam, a bow-tie cavity has two waists, ω_{small} inside the crystal and ω_{big} between M_1 and M_2. The fundamental light circulates though the cavity many times until it is either absorbed (by the mirrors or crystal), transmitted (though through the mirrors), or generates the second harmonic.

There are several design considerations when arranging the mirror to form the cavity. First the cavity needs to be stable, meaning that a beam inside the cavity is not diverging and can be spatially contained inside the cavity. A bow-tie cavity is considered stable if the following condition is met,

$$-1 < \frac{2L(L_c - L_c n_\omega + n_\omega(L_M - r)) + r(2L_c(n_\omega - 1) + n_\omega(r - 2L_m))}{n_\omega r^2} < 1. \tag{4.3}$$

The distances L, L_c, and L_m are illustrated and defined in Fig. 4.19b, r is the radius of curvature of the two mirrors, and n_ω is the index of refraction of the crystal at 960 nm. Another consideration is the size of the two waists, ω_{small} and ω_{big} inside the cavity. Decreasing ω_{small} results in a larger η_{SHG}. However, if ω_{small} is made too small instabilities can arise due to heating of the crystal [98].

$\omega_{\text{small}} \sim 50\,\mu$m is sufficient for SHG and to avoid any negative thermal effects. Knowledge of ω_{big} is used to aid in mode-matching the incoming light to the mode of the cavity. The waists can be calculated,

$$\begin{aligned}\omega_{\text{small}} =& \left(\frac{L(L_c - n_\omega L_c + n_\omega(L_m - r)) + r(L_c(n_\omega - 1) - n_\omega L_m)}{4\pi^2 n_\omega^2 (L - r)}\right)^{1/4} \lambda_\omega^{1/2} \\ &\times \left(\frac{L_c(n_\omega - 1) + n_\omega(r - L_m)}{4\pi^2 n_\omega^2 (L - r)}\right)^{1/4} \\ \omega_{\text{big}} =& \omega_{\text{small}} \left(\frac{n_\omega^2 (L - r)^2}{L_c(n_\omega - 1) + n_\omega(r - L_m)}\right)^{1/4}.\end{aligned} \tag{4.4}$$

The parameters for the constructed cavity are, $L = 160\,$mm, $L_m = 65\,$mm, $L_c = 20\,$mm, $n_\omega = 1.83$, $r = 50\,$mm. These parameters yield a stable cavity with waists, $\omega_{\text{big}} = 170\,\mu$m and $\omega_{\text{small}} = 40\,\mu$m.

The fundamental power circulating inside the cavity P_c is [99],

$$P_c = \frac{P_\omega T_1}{\left(1 - \sqrt{(1 - T_1)(1 - L_{\text{rt}})(1 - \eta_{\text{SHG}} P_c)}\right)^2}, \tag{4.5}$$

where P_ω is the fundamental power incident on the cavity, T_1 is the transmission of the input coupler M_1, and L_{rt} is the fractional round-trip loss from the other 3 mirrors and crystal facets. For fixed values of L_{rt}, P_ω, and η_{SHG}, Eq. 4.5 can be optimized for T_1. T_1 was chosen to maximize the blue output power outside the cavity. For estimated experimental parameters of $P_\omega = 800$ mW, $L_{\text{rt}} = 3\%$, and $\eta = 1\%$, P_c can be as high as 7.5 W.

With an input power of $P_\omega = 800$ mW, the blue power out of the cavity is $P_{2\omega} = 200$ mW, for an efficiency of $\eta = 25\%$. The efficiency is a bit lower than the expected $\eta_{\text{SHG}} = 50 - 75\%$ that has been achieved in similar setups

Table 4.2: Specifications of the bow-tie cavity mirrors. The diameter of each mirror is 12.7 mm

Mirror	M_1	M_2	M_3	M_4
Manufacturer	Standa	Thorlabs	Eksma	Eksma
Part Number	14DM-05-PR7.90-0	BB05-E03	-	-
Type	plane	plane	plano-concave (roc = 50 mm)	plano-concave (roc = 50 mm)
Reflectivity	0.90 @ 946 nm	0.996 @ 960 nm	0.995 @ 972 nm	0.995 @ 972 nm
Transmission	-	-	-	0.90 @ 486 nm
Thickness	2 mm	6 mm	6 mm	6 mm

[98, 99]. This is most likely due to improper mode or impedance matching, but the output power is sufficient for current experimental needs.

The intensity of the blue light exiting the cavity is locked to the side of a Fabry-Pérot peak. A small percentage of light is transmitted through M_3 and is directed onto a photodiode. The signal is sent to a FPGA to generate a locking signal in a similar setup to the repumper in Section 4.6.2. The feedback is sent a piezo that is attached M_2.

By changing the temperature of the crystal, the length of the crystal changes, which make the QPM conditions zero different wave lengths. This is necessary because in many experiments involving Rydberg atoms a certain n or range of n's are desired. The change in the length of the grating period is,

$$\Delta\Lambda = \Lambda_0(\alpha(T - T_0) + \beta(T - T_0)^2), \tag{4.6}$$

where $\alpha = (7.0 \pm 0.2 \times 10^{-6}\,^{\circ}\mathrm{C}$ and $\beta = (4.4 \pm 0.8) \times 10^{-9}$ [100] are coefficients of thermal expansion and Λ_0 is the period length at temperature T_0. A period

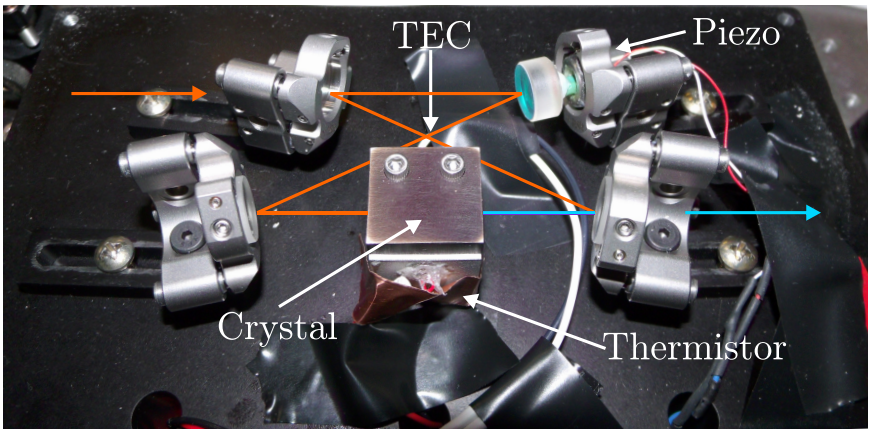

Figure 4.20: Photograph of the bow-tie cavity.

of length Λ will satisfy QPM conditions for wavelengths of the fundamental and harmonic that satisfy [101],

$$\Lambda(T) = \frac{\lambda_\omega}{2(n_{2\omega}(T) - n_\omega(T))}. \tag{4.7}$$

Experimental data for the temperature dependent QPM conditions is shown in Fig. 4.21, and a linear behavior is observed. The experimental slope is $18.0 \pm 0.1\,^\circ\mathrm{C/nm}$. Using the equations for $n(\lambda, T)$ [102, 103] the theoretical slope is $18.2 \pm 0.1\,^\circ\mathrm{C/nm}$. This result also similar to the experimental value of $18.2\,^\circ\mathrm{C/nm}$ in [104].

The temperature of the crystal is controlled with either a thermoelectric cooler (TEC), or a resistive heater. The TEC (TEC1.4-6) is used when the phase-matching temperature is near room temperature, and the resistive heater (HT15W) is used when higher temperatures are needed. These elements control a block that the crystal sits in as shown in Fig. 4.20. A thermistor (TH10K) is mounted inside the block close to crystal to sense the temperature. To minimize

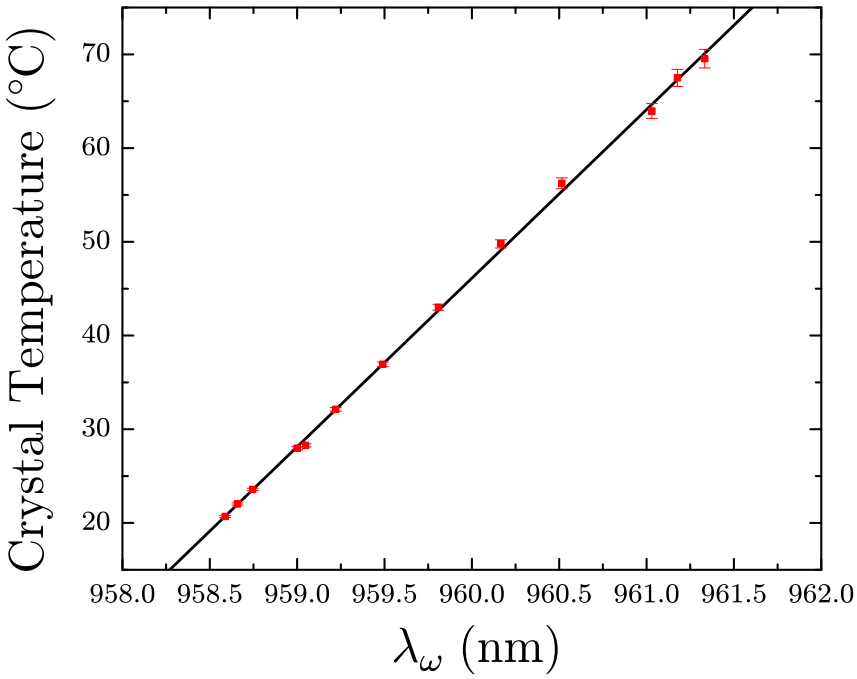

Figure 4.21: Phase-matching temperature for various values of λ_ω used in experiments over several years. The black line is a linear fit to the data with a slope of $18.0 \pm 0.1\,^{\circ}\mathrm{C/nm}$

thermal fluctuations and air turbulence, the cavity is mounted on a aluminum block that is sealed from the environment. Holes are drilled into the aluminum block and BNC bulkheads are used. An aluminum cover is placed over the cavity. Holes allowing optical access for laser beams are cut and sealed with windows.

The beam from the TA is focused into the cavity in order to overlap its mode with the TEM_{00} mode of the cavity. Successful operation of the cavity depends on the precise alignment of all 4 cavity mirrors as well as the input beam. Instructions for aligning the cavity are detailed in Appendix B.

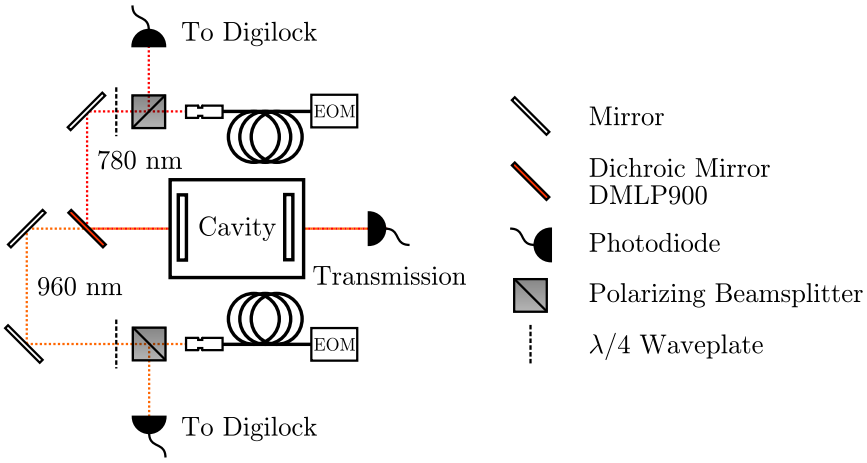

Figure 4.22: A schematic of the optical setup used for locking the two Rydberg excitation lasers. Both lasers are coupled into the cavity at the same time using a dichroic mirror. Transmitted and reflected signals are detected with photodiodes.

4.6.6 Rydberg Laser Stabilization

Both Rydberg excitation lasers are locked to the same Fabry-Pérot cavity. The system, consisting of the cavity (AT Films), and its vacuum housing (Stable Laser Systems), were bought commercially. The system is designed to provide a narrow locking signal, while minimizing the frequency drift of the cavity. The cavity mirrors are made from ultra low expansion (ULE) glass with the inner surfaces coated for high reflectivity at 780 and 960 nm, and the outer surfaces anti-reflection coated. From the provided data the finesse of the cavity is calculated to be $\sim$ 10,000 at 780 and 960 nm respectively. One mirror has a radius of curvature of 50 cm, while the other mirror is flat. In between the

mirrors is a cylindrical spacer made from ULE glass, that sets the cavity length at 10 cm. For this cavity the free spectral range (FSR), $c/2L$ is 1.5 GHz. The corresponding full width at half maximum (FWHM) of a transmission peak is 150 kHz.

To minimize thermal drift of the cavity, the temperature of the system is stabilized at, 32°C, the manufacturer measured temperature, where the coefficient of thermal expansion is zero. A 3 L/S ion pump (Gamma Vacuum 3S-CV-1H-5K-N-N) is used to pump the system at a pressure of 2×10^{-7} Torr to minimize pressure shifts of the cavity.

The optical setup for the locking is shown in Fig. 4.22. The input light is mode matched to the TEM_{00} mode of the cavity to maximize the signal. This is done by adjusting the lens of the fiber collimator (CFC-5X-B), and adjusting the optical path length of the beam, to maximize the power in the TEM_{00} mode.

Both lasers are locked to the cavity using a cascaded Pound Drever Hall (CPDH) scheme [105, 106]. CPDH is a variant of the popular Pound Drever Hall (PDH) scheme [107]. In a standard PDH scheme the frequency of the laser in modulated at a frequency $\omega_{\text{fix}}/2\pi >$ FWHM, putting sidebands on the main carrier frequency of the laser. The electric field of the laser exiting the EOM is,

$$E(t) = E_0 e^{i\omega_0 t + \alpha \sin(\omega_{\text{fix}})}, \tag{4.8}$$

where ω_0 is the frequency of the incoming laser, and α is the amplitude of the

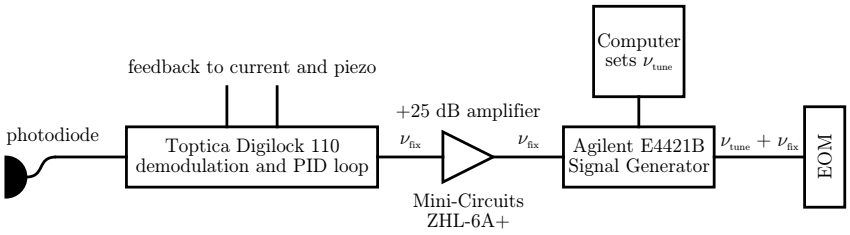

Figure 4.23: A schematic of the electronics used for locking the two Rydberg excitation lasers. An identical setup is used by both lasers.

electric field applied to the EOM. To first order, $E(t)$ can be written as,

$$E(t) = E_0 \left(e^{it\omega_0} - \frac{\alpha}{2} \left(e^{it(\omega_0 - \omega_{\text{fix}})} - e^{it(\omega_0 + \omega_{\text{fix}})} \right) \right), \tag{4.9}$$

where three frequency components, the carrier frequency ω_0 and two sidebands at $\omega_0 \pm \omega_{\text{fix}}$ can be seen. Using a quarter waveplate and a polarizing beamsplitter, the beam that is reflected from the cavity is separated from the incoming beam and is sent to a photodiode. The reflected beam is a combination of two beams, one that does not enter the cavity and reflects off the first mirror, and one from inside the cavity. Near cavity resonance an interference pattern is created when, the reflected beam at ω_0 interferes with the sidebands. The locking signal is generated by demodulating the the reflected signal at the modulation frequency similar to FM spectroscopy. The advantages of this are that the signal has a high slope and is centered around zero. The main limitation of this method is lack of tunability. The laser is only able to be locked to cavity resonances. CPDH makes the system tunable by using two different modulating frequences, ω_{fix}, and ω_{tune}. Both frequencies are applied to the EOM through the same electronic

signal, $E_{\text{ele}}(t) = \alpha \sin(\omega_{\text{tune}} t + \beta \sin(\omega_{\text{fix}} t))$, where the sine wave at a frequency ω_{tune} is phase modulated at frequency ω_{fix}. The electric field of the laser is now,

$$E(t) = E_0 e^{i\omega_0 t + \alpha \sin(\omega_{\text{tune}} t + \beta \sin(\omega_{\text{fix}} t))} \tag{4.10}$$

Instead of three frequency components, the beam has seven frequency components, which can be seen from the first order expansion,

$$\begin{aligned} E(t) =& E_0 \left(e^{it\omega_0} - \frac{\alpha}{2} \left(e^{it(\omega_0 - \omega_{\text{tune}})} - e^{it(\omega_0 + \omega_{\text{tune}})} \right) \right) \\ & - \frac{E_0 \alpha \beta}{4} \Big(e^{it(\omega_0 - \omega_{\text{tune}} - \omega_{\text{fix}})} + e^{it(\omega_0 + \omega_{\text{tune}} - \omega_{\text{fix}})} \\ & - e^{it(\omega_0 - \omega_{\text{tune}} + \omega_{\text{fix}})} - e^{it(\omega_0 + \omega_{\text{tune}} + \omega_{\text{fix}})} \Big). \end{aligned} \tag{4.11}$$

Demodulating the reflected signal around ω_{fix}, produces two PDH signals centered around ω_{tune}. $\omega_{\text{tune}}/2\pi$ can be tuned from $\omega_{\text{fix}}/2\pi$ to $\text{FSR}/2 - \omega_{\text{fix}}/2\pi$ and both sidebands can used for locking, resulting in a tunable locking system.

A schematic for the electronics used for locking each laser is shown in Fig. 4.23. The Digilock 110 generates a signal at $\omega_{\text{fix}}/2\pi = 6.25\,\text{MHz}$, that phase modulates $\sin(\omega_{\text{tune}} t)$ in the function generator via an external input. The combined signal is then sent to the EOM, which generates the side bands on the laser. An example of the transmitted and reflected signals of the 960 nm laser is shown in the black and red traces respectively in Fig. 4.24. All seven frequency components in the transmitted signal are shown, with $\omega_{\text{tune}}/2\pi = 100\,\text{MHz}$. The reflected signal is demodulated by the Digilock Module. The estimated linewidth of the lasers is 15 kHz. The drift of the cavity is $\sim 1\,\text{MHz/month}$.

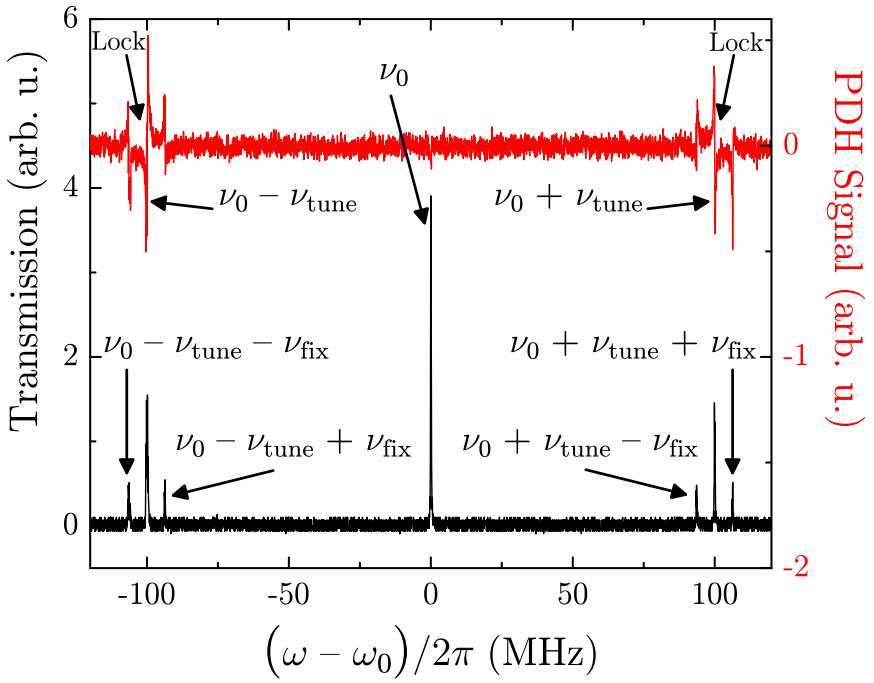

Figure 4.24: Plots of the transmission through the cavity (black) and the demodulated PDH (red) signals for the 960 nm laser. The labels and arrows point the 7 different frequency components on the laser.

Chapter 5

Experimental Techniques

In this chapter, the experimental techniques used for creating and probing the cold atomic clouds Rb near the quartz surface are detailed. The atoms are cooled from a background vapor in a magneto optical trap (MOT). Atoms are transferred from the MOT to a magnetic trap and transported to the quartz surface. Near the surface, the electric field is measured using Rydberg atom EIT. Rydberg atom EIT near the surface is observed using absorption imaging.

5.1 MOT

The atoms are initially cooled and trapped in a mirror magneto-optical trap (mirror-MOT) inside of the vacuum system pictured in Fig. 4.1. The MOT is loaded from a background vapor of Rb. A traditional MOT uses 6 laser beams and a linearly varying magnetic field to cool and trap the atoms[108]. The linearly varying field is produced by the MOT coils, which generate a quadrupole magnetic field. The cooling beams are a combination of the trapper and repumper. In a mirror-MOT, 2 of the laser beams are generated by reflection off of a mirror near the trap. A mirror-MOT is used so that the atoms can be trapped close to the quartz surface.

A cross section of the experimental chamber and the orientations of the laser beams is shown in Fig. 5.1. The output of the TA that contains the trapper

and repumper is coupled into a fiber and transported near the chamber. The beam out of the fiber is expanded to a waist of $\sim 10\,\mathrm{mm}$ so that a large number of atoms can be cooled and trapped. Using polarizing beamsplitters and half wave plates, the beam is split equally into three separate beams. One of the MOT beams passes directly through the chamber along x-direction, and is retro-reflected along the $-x$-direction with a mirror outside of vacuum. The other two MOT beams are incident upon the gold mirror at 45°, the reflection of these beams off of the mirror generates the remaining two beams needed for the MOT. The MOT coils are mounted at a 45° angle to the mirror, so the magnetic fields align correctly with the polarizations of the laser beams.

5.2 Magnetic Trap

After the atoms are loaded into the MOT, they are transferred to the magnetic trap. The magnetic trap uses the energy shift of the atoms combined with a spatially varying magnetic field to create an attractive potential. In the presence of a magnetic field the energy shift of the ground states is [57],

$$\Delta E = \mu_B g_F m_F B_z, \tag{5.1}$$

where μ_B is the Bohr Magneton, and g_F,

$$\begin{aligned} g_F &\simeq g_J \frac{F(F+1) - I(I+1) + J(J+1)}{2F(F+1)} \\ g_J &\simeq 1 + \frac{J(J+1) + S(S+1) - L(L+1)}{2J(J+1)}. \end{aligned} \tag{5.2}$$

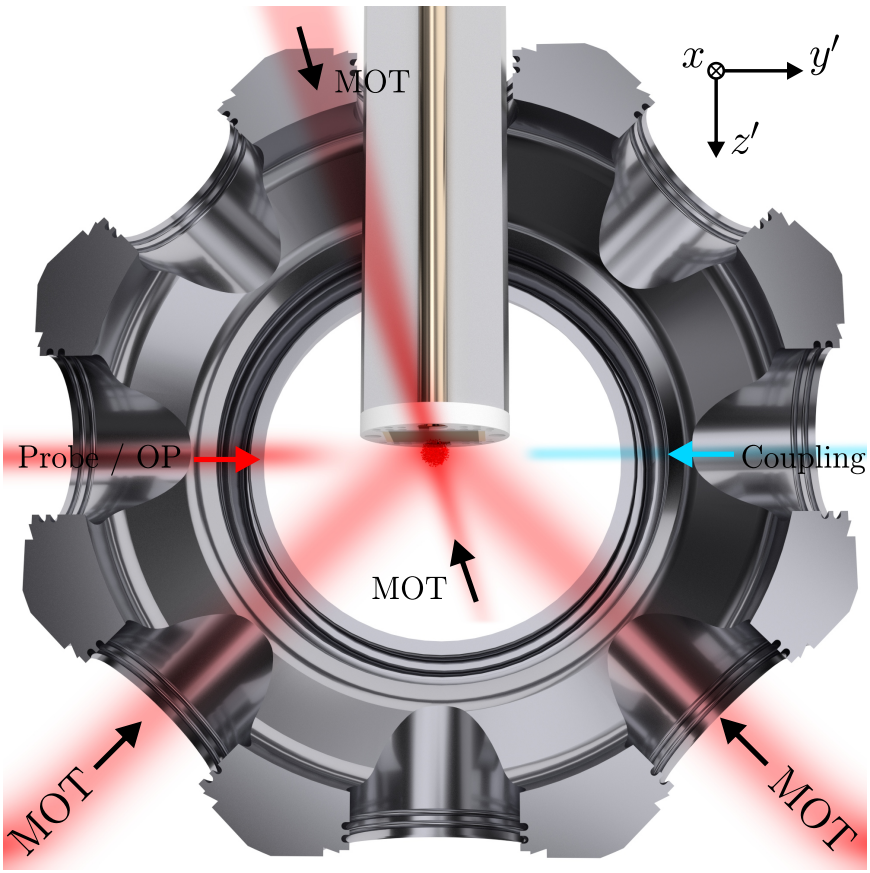

Figure 5.1: Illustration of the mirror-MOT inside a cross section of the vacuum chamber. The black arrows indicate the direction of travel of the 4 MOT beams. The colored arrows indicate the direction of travel of the imaging/OP and coupling beams. The imaging and optical pumping (OP) beams follow the same beam path. The MOT is formed $\sim 1 - 2\,\text{mm}$ from the quartz surface.

The approximations $g_L \simeq= 1$, $g_S \simeq 2$, and $g_I = 0$ are made. The sign of the energy shift, Eq. 5.1, depends on the state of the atom, which determines the signs of m_F and g_F. Atoms will feel a force that depends on the gradient of the magnetic field, $F = -\nabla(\Delta E)$. A potential well is created around a magnetic

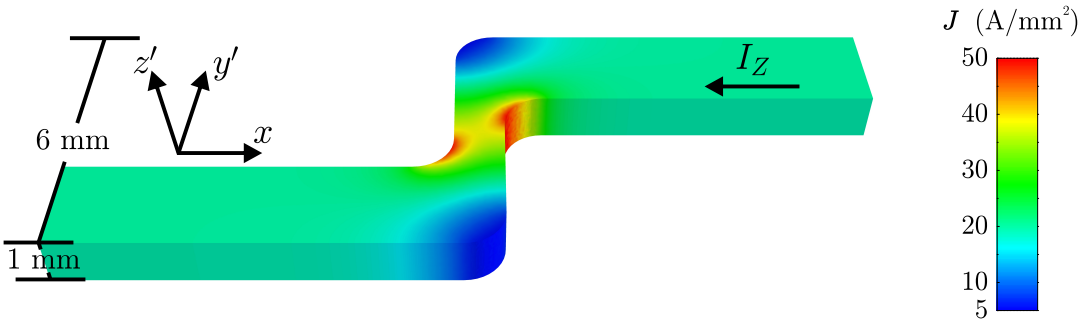

Figure 5.2: Image of the current density through the Z-wire. The current flows from the right side of the wire to the left. The current density J is uniform in the straight parts of the wire, but is concentrated at the corners when the wire bends.

field minimum for states with $g_F m_F > 0$, while states with $g_F m_F < 0$ will see a potential hill. The converse can be said for a magnetic field maximum. Atoms with $m_F g_F < 0$ are referred to as high-field seekers and those with $m_F g_F > 0$ are low-field seekers.

Due to Earnshaw's Theorem [109], a magnetic field maximum cannot be created in free space, so a magnetic field minimum is created to trap low-field seeking states. For the ground states of ^{87}Rb the low-field seeking states are $F = 2\,(m_F = 1, 2)$ and $F = 1\,(m_F = -1)$ with $g_F = +1/2$ and $-1/2$ respectively. The $F = 2\,(m_F = 2)$ state has the largest trapping potential and is used for the experiments.

The quadrupole field from the MOT coils could be used to generate the trapping field, however the current needed to produce a deep enough trap would be $\sim 200\,\mathrm{A}$. Also, a major issue with quadrupole traps is the zero crossing of the

magnetic field. As an atom crosses a magnetic field zero and the field changes faster than the spin precession, transition to another m_F state can occur [110]. The effect is called a spin-flip or Majorana transition, and limits the lifetime of the trap.

The magnetic trap used in the experiment is in a Ioffe-Pritchard configuration [111] with no zero crossing of the magnetic field. The field is generated using the Z-wire (Section 4.5.1) and bias coils (Section 4.3.1). The bias coils apply a uniform field in the atomic region in the x, y, and z directions. The three orthogonal coils can generate a field in an arbitrary direction.

The magnetic field from the Z-wire is calculated using a finite element method. This is necessary because current does not flow uniformly through the wire, especially at the corners as shown in Fig. 5.2. The magnetic trap is formed at distances from the Z-wire that are comparable to its feature sizes. The wire is broken up into smaller elements. The volume current through each element is found by solving Maxwell's equations after applying appropriate Dirichlet and Neumann boundary conditions to the surfaces of the wire. Using the current elements, the magnetic field is calculated using the Biot-Savart law, summing the contribution from each element.

It is convenient to reference the magnetic field to the x, y', z' coordinate system as defined in Fig. 5.3. The initial magnetic trap is generated with $I_Z = 38.6\,\mathrm{A}$, $B_x = 16\,\mathrm{G}$, $B_{y'} = -14.3\,\mathrm{G}$, and $B_{z'} = 0\,\mathrm{G}$. Plots of the magnetic field magnitude, $|B|$ in the x-y' plane and y'-z' plane centered at the field

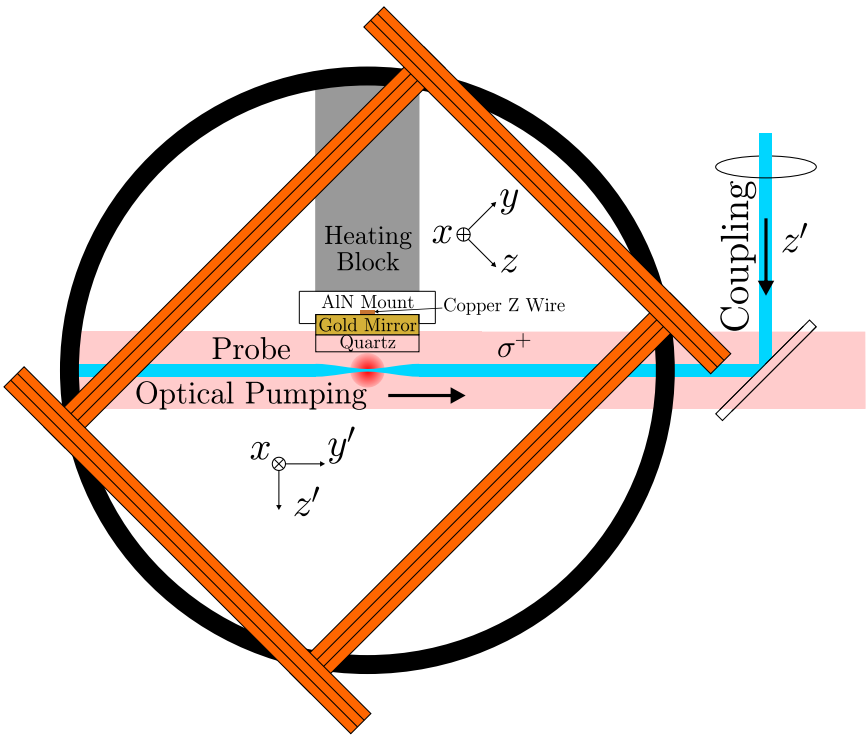

Figure 5.3: Schematic of the optical setup for observing Rydberg atom EIT with absorption imaging. The probe and optical pumping light is collimated with a waist of 4 mm and is σ^+ polarized. The coupling beam is linearly polarized in the z'-direction, and using a dichroic mirror is counter-propagating with the probe and optical pumping beams.

minimum are shown in Fig. 5.4(a) and (b) respectively. The magnetic trap is centered around the minimum of the magnetic field, B_{min}, at $z' \approx 1.5\,\text{mm}$.

To move the atoms near the surface, B_x is ramped linearly from 16 to 28 G linearly over a period of 35 ms. B_{min} moves closer to the surface ($z \approx 300\,\mu\text{m}$). The magnetic fields in this configuration are plotted in Fig. 5.4(c) and (d).

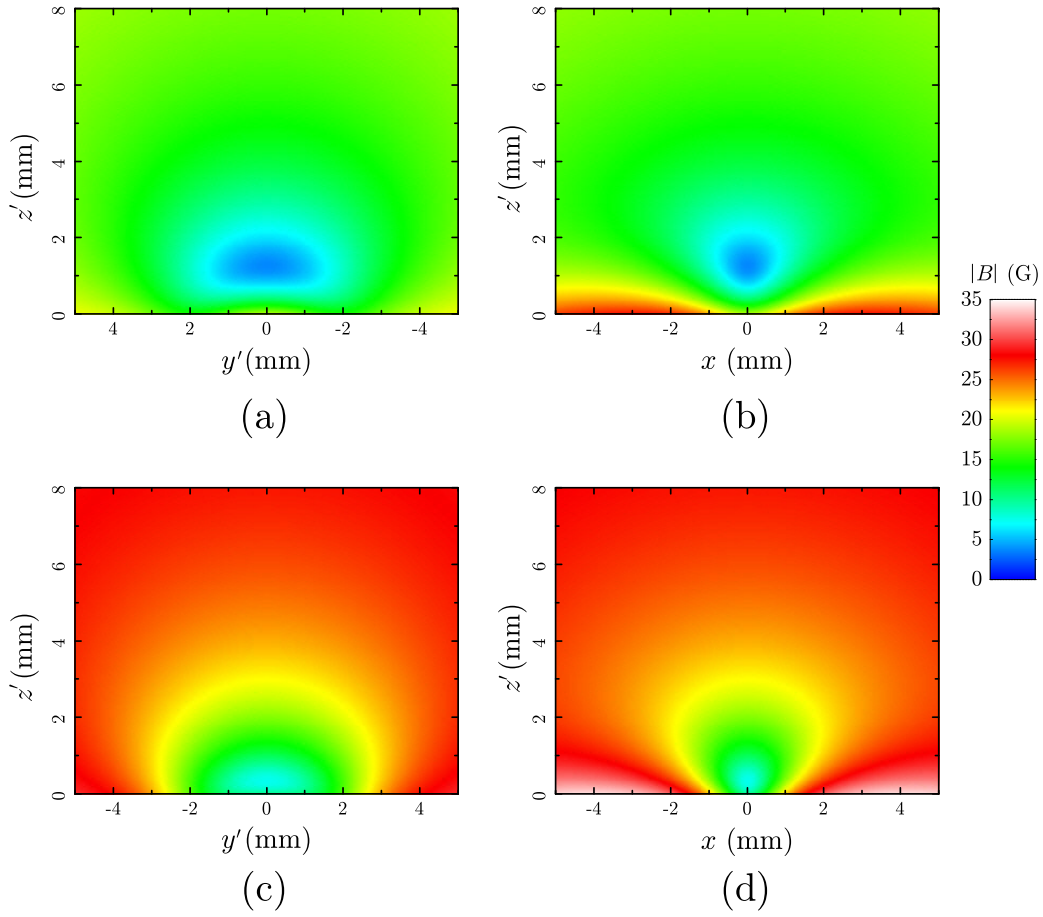

Figure 5.4: 2D plots of the magnetic field magnitude $|B|$. The center of the Z-wire is centered at $x = y' = 0$. The distance in the z'-direction is measured from the quartz surface, with free space, $z' > 0$.

5.2.1 Optical Pumping

After the MOT is turned off the atoms are in the $F = 2$ ground state, but populate all of the m_F states. The atoms are optically pumped into the $F = 2, m_F = 2$ state so they can be magnetically trapped. To accomplish this, the y and

z-bias coils are turned on creating a uniform field along the y'-direction. The direction of the field defines the quantization axis for optical pumping, and is also the major component of the field in the Z-trap. An optical pumping beam propagates along the y'-direction and is tuned to the $F = 2 \leftrightarrow F' = 2$ transition, is σ^+ polarized, and is pulsed on for $400\,\mu$s. A diagram of the optical setup is shown in Fig. 5.3. The power of the optical pumping beam is kept low to avoid stimulated emission, and the dominant relaxation process is radiative decay. The allowed transitions and strengths of absorption and radiative decay on the optical pumping transition are shown in Fig. 5.5. Through the process of absorption of σ^+ light, an atom undergoes a change of $\Delta m_F = +1$. While in an excited state an atom can radiatively decay into several possible states, over many decays the average change is $\Delta m_F \approx 0$. The net effect after many transitions is the hyperfine population moves to higher and higher m_F until atoms decay into the $m_F = 2$ state. Once in this state the atoms no longer absorb optical pumping photons and are in a dark state. Note that the sum of $\Gamma_B \neq 1$ for each excited state as shown in Fig. 5.5b, because the $F' = 2$ state can also decay into the $F = 1$ ground state which is not pictured. The repumper is on during the optical pumping process to prevent the atoms ending up in the $F = 1$ ground state. After the atoms are all pumped into the $m_F = 2$ state they are ready to be loaded into the magnetic trap.

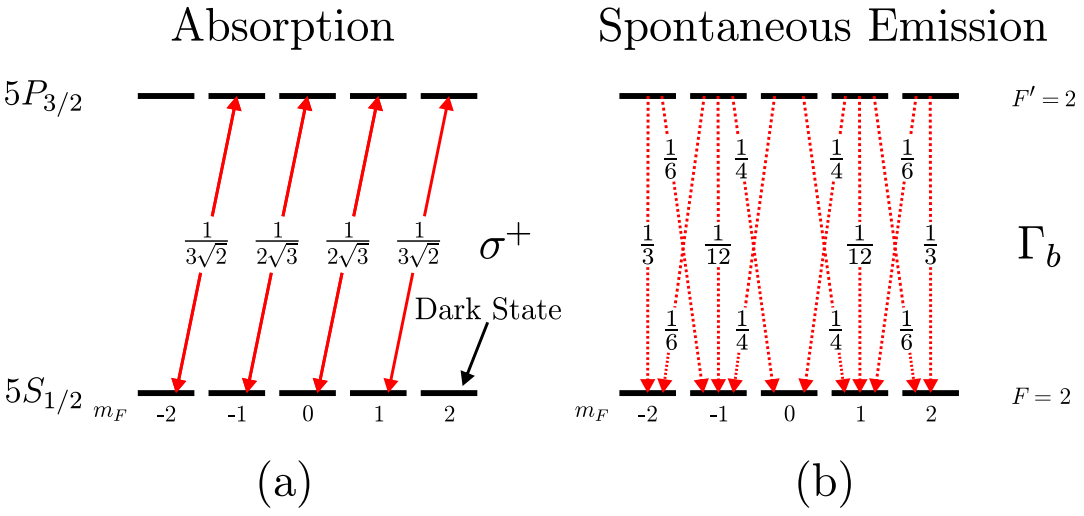

Figure 5.5: Diagrams of the transitions involved in optical pumping. (a) Shows the transitions and strengths (μ_a) for the absorption of the σ^+ polarized optical pumping beam. (b) Shows the rates of radiative decay, Γ_b, for each transition.

5.3 Absorption Imaging

A widely used technique for probing cold atoms is absorption imaging [112]. In these experiments, absorption imaging is used to spatially detect Rydberg atom EIT. An experimental schematic of absorption imaging is shown in Fig. 5.6. A collimated laser beam that is resonant with the $5S_{1/2} \leftrightarrow 5P_{3/2}$ transition is incident on a cloud of cold atoms. The atoms will absorb the resonant light and the shadow of the atom cloud is imaged onto a CCD camera. Two lenses are used for imaging the shadow of the atoms onto the CCD camera with a magnification of 2 from the original size. With the incident laser intensity below

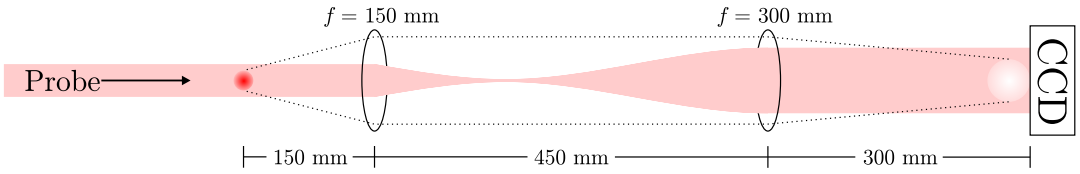

Figure 5.6: Experimental setup of absorption imaging. A resonant laser beam passes through the atoms. The shadow of the atoms is imaged onto a CCD camera. The pink is the profile of the laser beam and the dashed line is an outline of the image of the absorbed atoms. The lenses are used to magnify the image of the atoms by a factor of 2.

saturation, the absorption is given by Beer's law [69],

$$I(\nu, z) = I_0 e^{-\sigma(\nu)n}, \tag{5.3}$$

where $I(\nu, z)$ is the intensity after passing through the atoms, I_0 is the incident intensity, $\sigma(\nu)$ is the absorption cross section, and n is the column density of the atoms. $\sigma(\nu)n$ is a dimensionless attenuation factor, and ν is the frequency of the incident light. This can be expressed as,

$$\sigma(\nu)n = \ln\left(\frac{I_0}{I(\nu, z)}\right). \tag{5.4}$$

$\sigma(\nu)n$ is related to a commonly used quantity named optical density (OD). OD is defined as $\log_{10}(\text{OD}) = I/I_0$. In terms of σn the OD is,

$$\text{OD} = \frac{\sigma(\nu)n}{2.303}. \tag{5.5}$$

Using absorption imaging the OD and n can be calculated for each pixel. This is done by taking a series of three images. The first image, I_{abs} is taken with

the cold atoms present and the imaging laser on. Next, a reference image I_{ref}, is taken with the imaging laser on, but no cold atoms. Lastly, a background image, I_{bg}, is taken with the imaging laser off to capture any stray light. Subtracting I_{bg} from I_{ref} and I_{abs} yields the values of I_0 and $I(\nu, z)$ respectively. The optical density can be computed through the following formula,

$$\text{OD} = \ln\left(\frac{I_{\text{ref}} - I_{\text{bg}}}{I_{\text{abs}} - I_{\text{bg}}}\right)/2.303. \tag{5.6}$$

An example of a processed absorption image of the MOT with the imaging laser on resonance is shown in Fig. 5.7. The column density n as well as the total atom number can be computed from the absorption image as well. The atom number can be calculated by multiplying the column density of each pixel by the trap area of each pixel, and summing over all pixels. The resonant cross section for the transition used is $\sigma(\nu) = 2.907(3) \times 10^{-9}\,\text{cm}^2$ [57].

The OD of the medium is dependent on the frequency, ν, of the laser. As the probe laser is scanned across the transition, the optical density of the medium changes as seen in Fig. 5.8. The data is taken from absorption images of the Z-trap as the probe laser is scanned across resonance. The black line is a Lorentzian fit to the data with a FWHM of 6.1 MHz.

5.4 Experimental Sequence

The experiment is run on a 10 s cycle using the DAQ cards, see Section 4.2. A majority of the cycle is spent loading the MOT. After the MOT is saturated

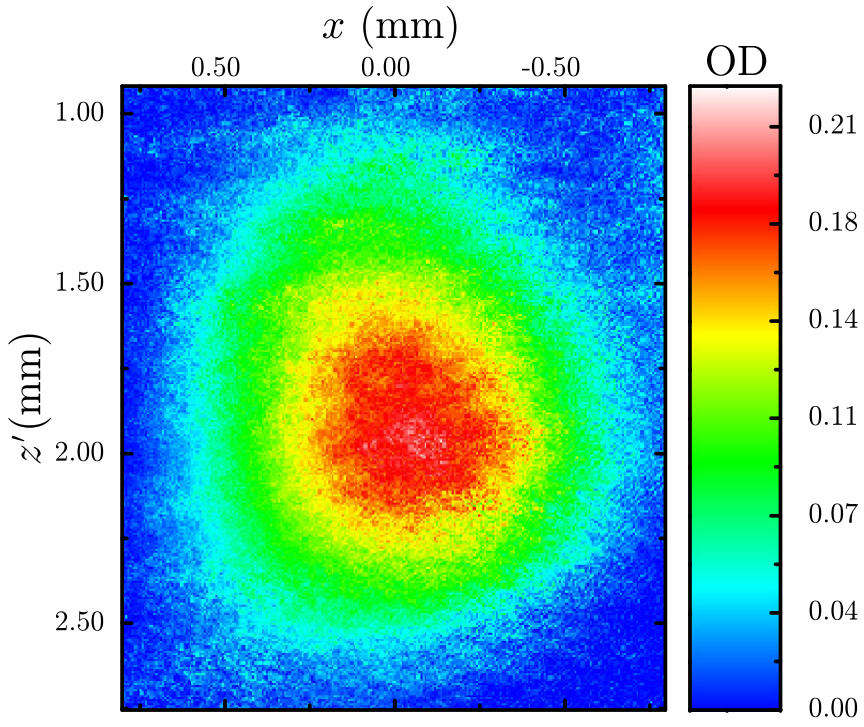

Figure 5.7: An absorption image of the MOT. The pixel color corresponds to the optical density (OD) shown on the right. This image was taken 3 ms after the MOT coils and lasers are turned off.

with atoms, the current in the MOT coils and the trapping laser is turned off. Before they turn off, the frequency of the trapping laser is detuned from the trapping transition by 43 MHz for 30 ms. Using polarization gradient cooling, temperature of the atoms is reduced from 170 μK to 15 μK.

After the MOT coils and trapper are off, optical pumping is done before loading the magnetic trap. To capture as many atoms as possible the initial magnetic trap is spatially overlapped with the MOT. The position of the magnetic trap can be moved in the z'-direction, but its position is the x-y' plane is mostly

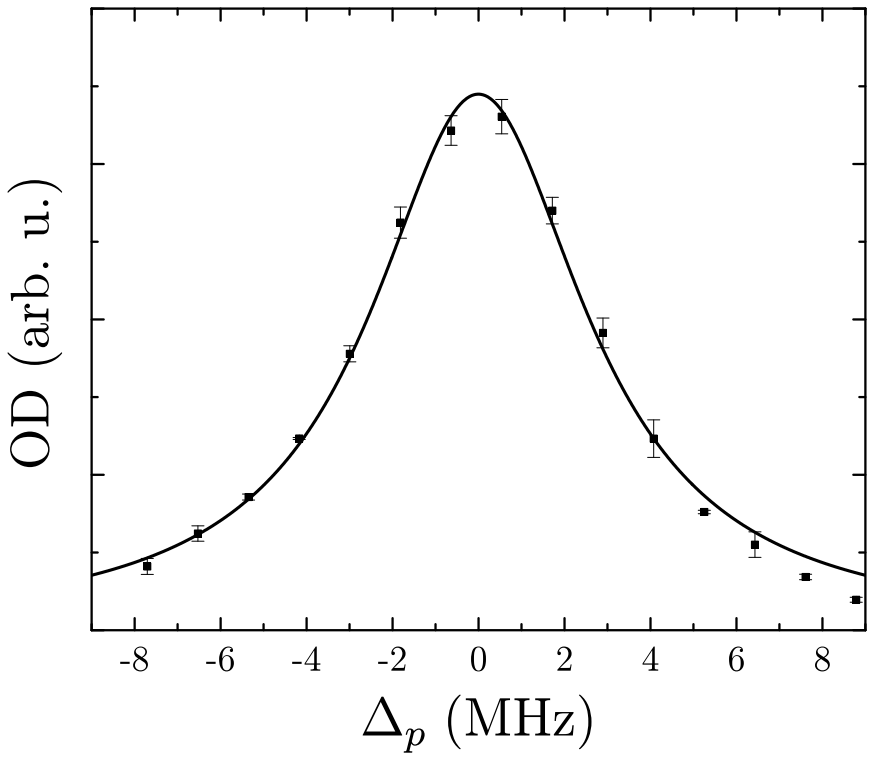

Figure 5.8: Absorption profile of the Z-trap. The probe laser is scanned across resonance, while many absorption images are taken. Three images are taken for each frequency, and the average of them at one pixel value are the experimental points. The error bars are the standard deviation of the three values. The black line is a fit of a Lorentzian fit to the data, with a full width at half maximum (FWHM) of 6.1 MHz.

fixed. The position of the MOT is adjusted by changing the relative power in the laser beams, changing beam pointing, and adding a small offset field with the bias coils to move the minimum of the quadrupole field.

After the optical pumping beam is switched off the bias field in the x-direction

is applied and current is sent through the Z-wire. Switching on the current in the Z-wire is delayed by 5.5 ms due to eddy currents in the stainless steel chamber produced by the switching of the bias coils. If the Z-wire is turned on too early the transient potential pushes the atoms out of the trap area. When the trap is off the atoms thermally expand and fall due to gravity, so if the Z-wire is switched on too late there will not be any atoms in the trapping area. A plot of the current switching is shown in Fig. 4.5. About 2/3 of the atoms are transferred from the MOT to the Z-trap.

After the atoms are initially loaded into the Z-trap, the magnetic field B_x is ramped linearly from 16 to 28 G linearly over a period of 35 ms. The atoms are released from the magnetic trap and imaged. The atoms can be imaged while in the Z-trap, however the spatially varying magnetic fields broaden the imaging transition and only a fraction of the atoms in the trap can be imaged at one time. The current in the Z-wire and x-bias coil are turned off, and the atomic cloud is imaged 1.5 ms later. The magnetic field is still applied along the $-y'$-direction, because turning off the current in the y and z-bias coils produces eddy currents and a magnetic field is still present in the atomic region for 7-8 ms. In the 7-8 ms time period the atoms fall away from the surface due to gravity and are no longer in the area of interest, so the trap is imaged with a magnetic field of $B_{y'} = -14.3\,\mathrm{G}$

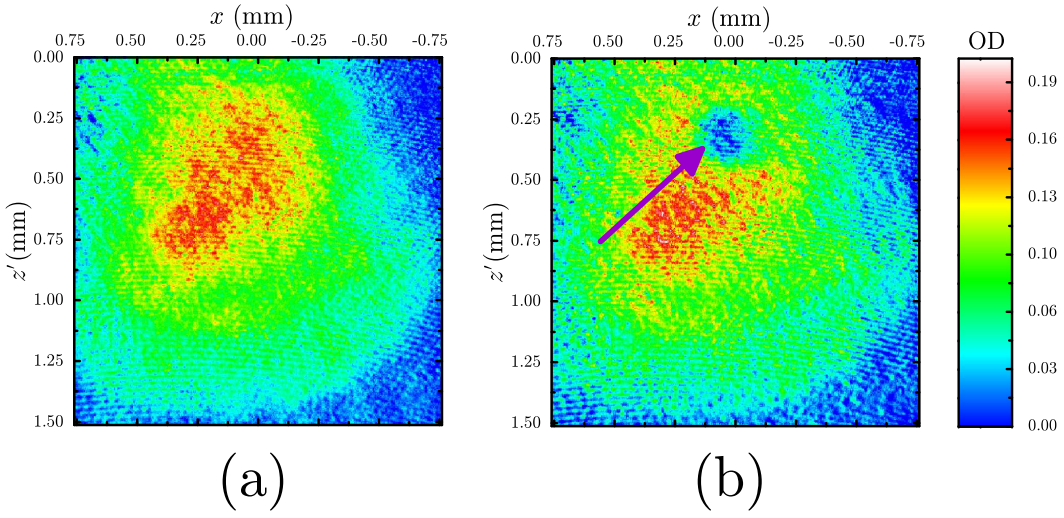

Figure 5.9: Absorption images of the atoms after release from the Z-trap. (a) Image taken without the coupling beam. (b) Image with the coupling beam on. The arrow highlights the effect of the coupling beam on the transparency of the atoms to the probe beam.

5.5 Rydberg EIT with Absorption Imaging

In the cold atomic sample, Rydberg EIT is detected by using absorption imaging. Similar setups have been used in [36, 37, 113, 114]. The coupling laser is counter-propagating with the probe beam, similar to the vapor cell experiments, and is focused through the atomic sample as illustrated in Fig. 5.3. The laser is focused to a waist of 50 μm at the position of the MOT or Z-trap. The waist is small to achieve the Rabi frequencies needed to perform the experiment. The presence of the coupling laser on resonance with the atoms causes them to be transparent to the probe laser. An example of two of the images are shown in Fig. 5.9. In the first image no coupling laser is present and an absorption image

of the Z-trap is taken. In the second image, with the coupling laser present and on resonance, the optical density of a patch of atoms in the trap is reduced. This area is highlighted by the purple arrow.

The frequency dependence of the Rydberg atom EIT signal is obtained by scanning either the probe or the coupling laser over the resonance and taking absorption images at each step. A single absorption image measures the response of the system for one set of frequencies. By changing the laser frequency, and taking absorption images at each step, an EIT spectrum can be obtained. An example while scanning the probe laser shown in Fig. 5.10.

5.6 Measuring DC Electric fields

Analogous to the microwave measurements, Rydberg EIT converts the measurement of the amplitude of a dc electric field, E into an optical frequency measurement. The amplitude is obtained by measuring the Stark shift of the Rydberg state and comparing to the calculation. The calculation is carried out as described in Appendix A. Due to the small polarizability of the $5S$ and $5P$ states, the shift of these states is neglected. The application of a dc electric field shifts resonance condition for Rydberg atom EIT. Electric fields have been measured using Rydberg atom EIT [34, 115, 116], and agree with theoretical Stark shift calculations of a known field.

The frequency response of the Rydberg states in an electric field varies with

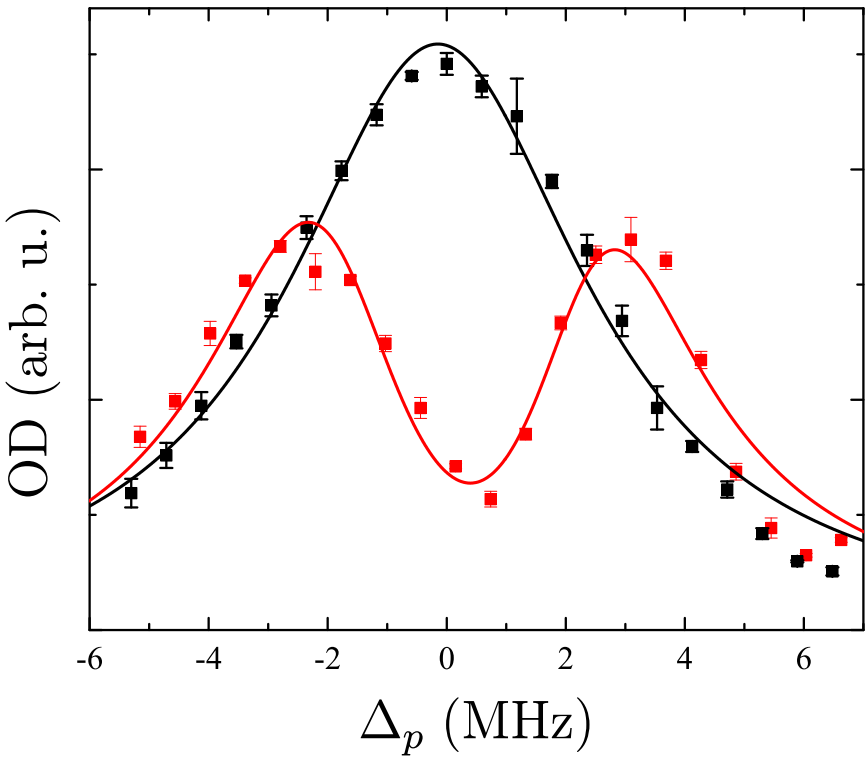

Figure 5.10: Rydberg EIT in the MOT. The black points are experimental data with no coupling beam. The black line is a Lorentzian fit to the data. The red points are data taken with the coupling laser present. The optical density is reduced near probe resonance. The red line is a fit to Eq. 5.7.

n, since the polarizability scales $\sim n^7$. A suitable n can be chosen to measure a given E. The shifts of the $41D$ and $81D$ states are shown in Fig. 5.11. Since the experiment is done in a background magnetic field after the magnetic trap is turned off, the atoms are still in the $m_F = 2$ state. The σ^+ imaging light couples the ground state atoms to the intermediate state with $m_J = 3/2$. The linear polarized coupling beam can couple together states with $\Delta m_J = \pm 1$, resulting

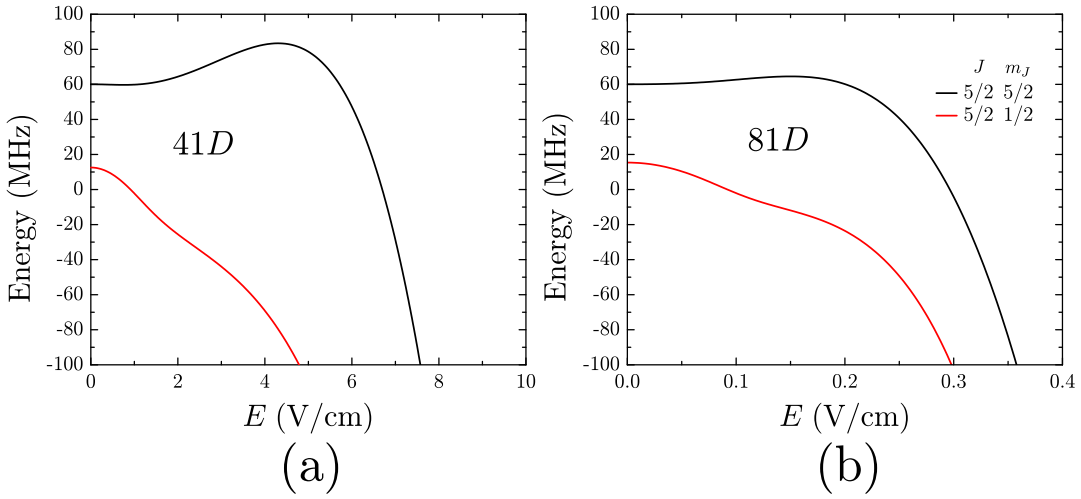

Figure 5.11: Stark shifts of the $J = 5/2$, $m_J = 5/2$, $1/2$ states in the (a) $41D$ and (b) $81D$ manifolds in a background magnetic field of 14.3 G. In the calculations, the direction of the magnetic field is orthogonal to the direction of the electric field.

in EIT from Rydberg states with $m_J = 5/2, 1/2$.

The advantage of detecting Rydberg EIT through absorption imaging a spatial distribution of atoms, is that the spatial dependence of the electric field can be obtained by analyzing different portions of the absorption image. Since the electric fields can spectrally shift the Rydberg state greater that the natural linewidth of the probe transition, the frequency of the coupling laser was scanned while taking absorption images. The probe laser and transition is fixed in frequency and the EIT condition shifts with the Rydberg state energy level. Scanning the coupling laser maps the shift of the Rydberg state onto a shift of the coupling laser frequency. A plot of an EIT signal while scanning

the coupling laser is shown in Fig. 5.12. To account for fluctuations in atom number over the $15-20$ minute duration of an experiment, an image is taken without the coupling laser after each image taken with the coupling laser present. With cold atoms, the Doppler shifts are negligible, and an analytic expression for $\mathrm{Im}[\rho_{12}]$ can be approximated using Eq. 2.28, assuming the population in the excited states is negligible,

$$\mathrm{Im}[\rho_{12}] = \mathrm{Re}\left[\frac{\Omega_p}{\Gamma_p - 2i\Delta_p + \frac{\Omega_c^2}{\Gamma_c - i(\Delta_p+\Delta_c)}}\right]. \tag{5.7}$$

The red line in Fig. 5.12 is a fit to Eq. 5.7.

The image recording is automated by computer. The frequency of the coupling laser is varied by changing the frequency of the lock ν_{tune}, see Section 4.6.6. The frequency range, frequency step, and number of averages are all set in a program that controls ν_{tune} via a RS232 cable. Using the frequency range, step size, and number of averages a list of frequencies is generated, as shown in Fig. 5.13. The list of frequencies is then randomized so technical noise does not skew the data. The camera program for capturing absorption images is setup to save the same number of images as the length of the list of random frequencies. The two programs are started at the same time and images are saved as the frequency is changed. Afterwards, the images are sorted and processed in Mathematica by importing the saved list of frequencies.

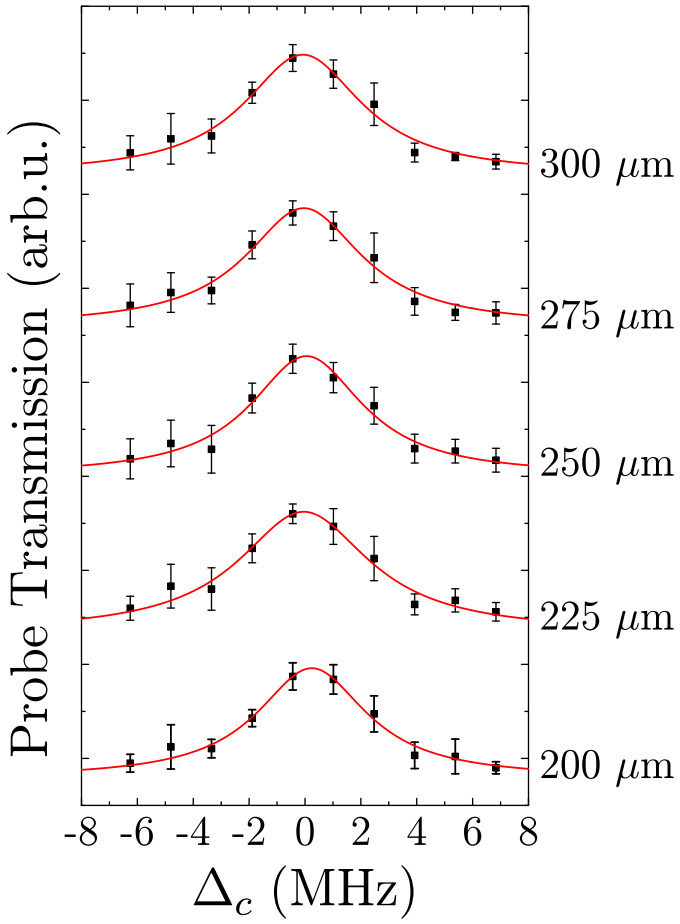

Figure 5.12: EIT spectra taken while scanning the coupling laser at different distances from the quartz in the Z-trap. The Rydberg state used in this experiment is the $81D_{5/2}$, $m_J = 5/2$ state. The black points are averages of pixel values for three different images. The error bars are the standard deviation of the experimental values. The red lines are Lorentzian fits to the data, with a FWHM $\approx 5\,\mathrm{MHz}$.

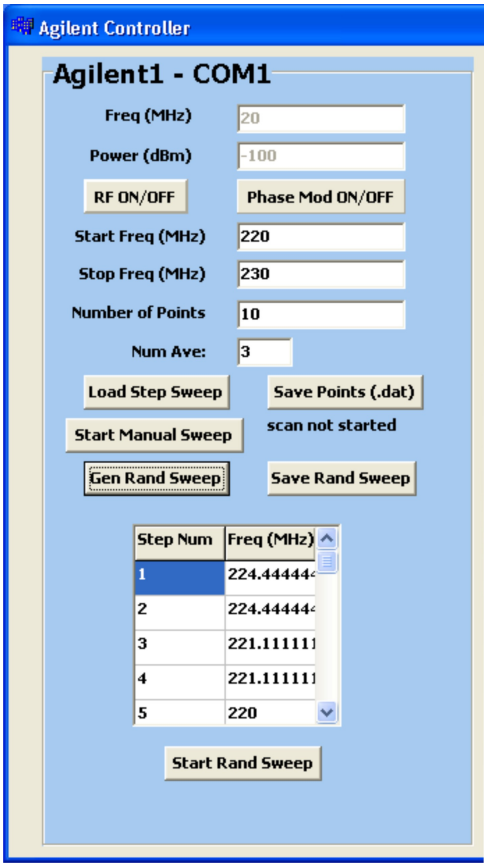

Figure 5.13: Screenshot of the program that controls ν_{tune}. The frequency range, number of steps, and number of averages are all set by the user. The list of frequencies is then randomized and saved. It is important to note that ν_{tune} controls the frequency of the 960 nm laser, while the frequency doubled 480 nm is used in the experiment. A change of 1 MHz of ν_{tune}, corresponds to a 2 MHz change of the 480 nm frequency.

Chapter 6

Near Surface Measurements

6.1 Electric Fields Near Surfaces

Recently a large effort in the atomic physics community is being put forth to create hybrid quantum systems. These efforts include interfacing quantum mechanical systems such as atoms, ions, or electrons, with macroscopic surfaces, electrodes, and resonators. Rydberg atoms are a strong candidate for use in these systems due to their long lifetimes and strong dipole transitions in the microwave regime.

A common problem encountered when constructing these devices is electric field noise on surfaces. The electric field noise is caused by adsorbates on the surface. An adsorbate is an atom or molecule that is bound to a surface [117]. The surface binding asymmetrically perturbs the electronic cloud of the atom or molecule, inducing a dipole moment. Adsorbates produce both dc [35, 38, 39, 41, 118, 119, 120] and ac [42, 121, 122, 123] electric fields that perturb experiments.

Working towards a quantum hybrid system using atoms, the system described in Chapters 4 and 5 was constructed to study the electric fields near the surface of quartz. Rydberg atom EIT is used to measure the dc electric field near the surface. The main result of this chapter is the reduction of the electric field,

and its small magnitude. The electric field measured near the surface is orders of magnitude smaller than other experiments. The reduction of the adsorbate electric field is due to the binding of low energy electrons on the (0001) surface of quartz. The low energy electrons are created from blackbody ionization of Rydberg atoms.

6.2 Theoretical Calculations

Many calculations are needed to describe and characterize experimental results. First a microscopic look at the Rb-surface binding is done through DFT calculations. The calculations were done by collaborators Eunja Kim and Phil Weck. Second, electrostatic calculations are done to estimate the dipole moment of a Rb adsorbate on the surface of quartz. Third, the model used to describe the electric field resulting from a patch of adsorbates is presented. The model relates the measured electric field to the density of Rb adsorbates on the surface of quartz. Next, Langmuir adsorption is introduced, which describes the amount of Rb adsorbed to the quartz surface as a function of temperature. Lastly, the average kinetic energy of blackbody ionized electrons is calculated. Blackbody ionization of Rydberg atoms is a source of ultra-low kinetic energy electrons, capable of binding to the surface and reducing the overall electric field.

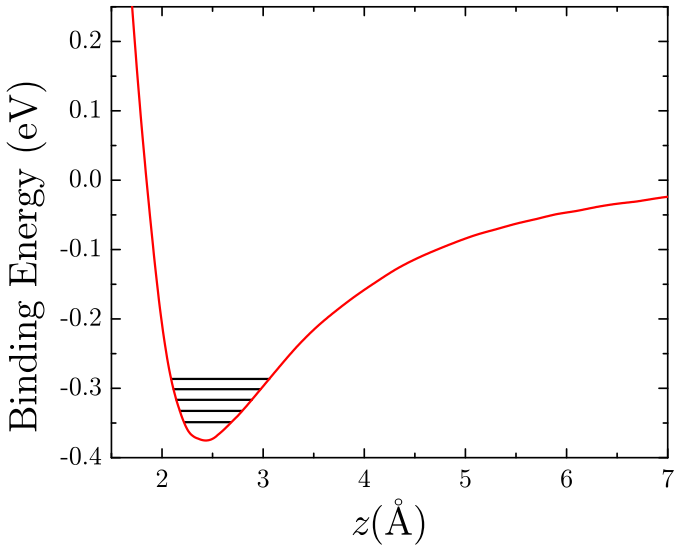

Figure 6.1: The interaction potential for Rb adsorbed on an O-terminated (0001) surface of quartz. The black lines indicate the energies of the lowest 5 vibrational states.

6.2.1 DFT Calculations

To investigate the Rb-quartz on a microscopic level, we performed total-energy calculations for the (0001) surface of quartz using spin-polarized density functional theory (DFT) [124]. The surface of the quartz is oxygen terminated [125]. The details of the DFT calculations are contained in [126] and references therein, and lie outside the scope of this thesis.

The Rb-quartz interaction potential is shown in Fig. 6.1 for a coverage of 1 monolayer. A monolayer (ML) is a surface that is completely filled with adsorbates. The amount of Rb atoms on the surface is described in terms of coverage, θ. The coverage relates the density of adsorbed atoms, ρ_a, to the

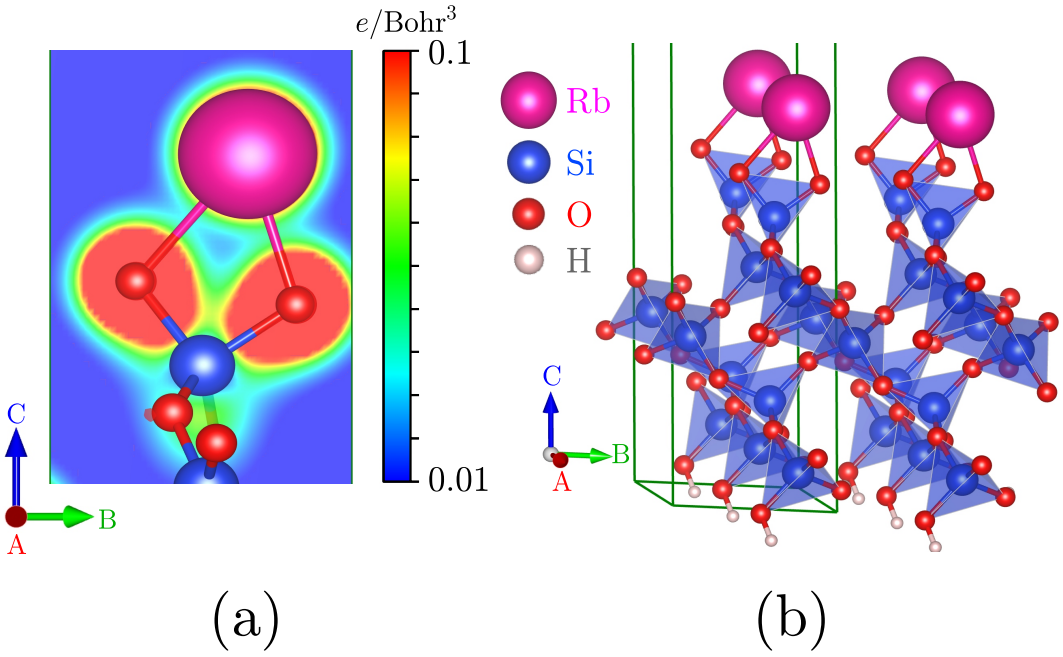

Figure 6.2: Results of the DFT calculations. (a) Charge density map for Rb-SiO_2(0001) in the plane of Rb and surface terminated O atoms. The Rb atom is positioned between the two surface O atoms and the charge density is centered around both O atoms, illustrating the Rb adsorbates are bound to two oxygen atoms. (b) Side view of the Rb adsorption on SiO_2(0001) surface. Each Rb atom (pink) is bound to two O atoms (red). The bottom of the slab is passivated by attaching hydrogen atoms (white). The green axes outline the periodic supercell used in the DFT calculations for 1 ML of coverage.

density of adsorption sites, $\rho_{\max}$ [127],

$$\theta = \frac{\rho_a}{\rho_{\max}}. \tag{6.1}$$

$\theta = 1$ corresponds to 1 monolayer. The energy of the lowest 5 bound states are

indicated with the black lines. Assuming a Boltzmann distribution of thermally occupied states, the lowest five states will contain $\sim 95\%$ of the population. The lowest bound state has an energy of $E_b = 0.35\,\mathrm{eV}$. The Rb is bound to two oxygen (O) atoms on the quartz surface. This can be seen by looking at the charge density map shown in Fig. 6.2a. Charge is transferred from the Rb atom and is localized around 2 O atoms, showing the dipole nature of an adsorbate. The positive end of the dipole is the Rb atoms, while the negative end of the dipole is on the surface. These calculations were done with a full monolayer, $\theta = 1$ of Rb.

With a coverage, $\theta = 0.11$, the charge transferred from one Rb adatom the the surface is $0.947e$, where e is the electron charge. The calculated equilibrium bond distance is $2.79\,\mathrm{\AA}$, resulting in a dipole moment of each adatom of, $d_0 = 0.947e \times 2.79\,\mathrm{\AA} = 12.7\,\mathrm{D}$.

6.2.2 Electrostatic Calculations

Alternatively to numerical DFT calculations, straightforward electrostatic calculations of the dipole moment can also be done. This is useful for gaining some physical intuition about the system, which is more difficult with the black box of DFT calculations. The dipole moment of an adsorbate can be estimated by calculating the dipole moment between a molecule consisting of the adsorbing atom, Rb, and the substrate atom, O. Using the fractional charge transfer, Δq,

and the bond distance, d_{cov}, the dipole moment d_0 is [128],

$$d_0 = \Delta q e d_{\mathrm{cov}}, \tag{6.2}$$

where e is the electron charge. The fractional charge transfer is,

$$\Delta q = 0.16|X_A - X_B| + 0.035|X_A - X_B|^2, \tag{6.3}$$

where the quantities X_i are the electronegativities of the atoms forming the bond. The results of the DFT calculation show that the Rb is bound to two oxygen atoms, which in turn are bound to a Si atom. The effective electronegativity of the substrate atom is the geometric mean of the three atoms, $X_B = (1.90 \times 3.44 \times 3.44)^{1/3} = 2.82$. The bond distance is the sum of the covalent radii, r_{cov}, of both atoms,

$$d_{\mathrm{cov}} = r_{\mathrm{cov}}^{\mathrm{Rb}} + r_{\mathrm{cov}}^{\mathrm{O}} = 2.79\,\text{Å}. \tag{6.4}$$

The values for X_i and r_{cov}^i are taken from the CRC Handbook [129]. Evaluating Eq. 6.2 yields a dipole moment from each Rb-O bond of $d_0 = 6.2\,\mathrm{D}$. The z component of d_0 is calculated using the O-O separation of 2.363 Å from the DFT calculations, yielding a total dipole moment in the z-direction of 12 D. These calculations are consistent with the 12.7 D calculated with DFT.

The dipole moment of the adsorbates are coverage dependent [130]. With an increasing amount of adsorbates, the electric field from neighboring adsorbates points in the opposite direction of the dipole, reducing the effective dipole moment of each adsorbate. The coverage dependent dipole moment of each

adsorbate is [128],

$$d(\rho_a) = \frac{d_0}{1 + 9\alpha_{\mathrm{ad}}\rho_a^{3/2}}, \tag{6.5}$$

where $\alpha_{\mathrm{ad}} = 47.3\,\text{Å}^3$[131] is the polarizability of Rb, and ρ_a is the density of adsorbed atoms.

6.2.3 Surface Adsorbate Model

The electric field from a single adsorbed atom is small and localized, but many adsorbates produce macroscopic electric fields. At a distance $z \gg 2\,\text{Å}$, the charge separation of the dipole, the electric field can be modeled as resulting from a layer of dipoles on the surface [37, 113]. The dipole field is modeled by two uniformly but oppositely charged square sheets with length L separated by a small distance. The resulting electric field near the center of the sheets and perpendicular to the surface is:

$$E_z(z) = \frac{2\sqrt{2}PL^2}{\pi\epsilon_0\sqrt{L^2 + 2z^2}(L^2 + 4z^2)}, \tag{6.6}$$

where ϵ_0 is the permittivity of free space, z is the distance from surface and P is the dipole density.

6.2.4 Langmuir Adsorption

The density of Rb atoms adsorbed on quartz can be calculated using the Langmuir theory of adsorption. The Langmuir theory of adsorption successfully describes the adsorption of a submonolayer of adatoms, but relies on several assumptions.

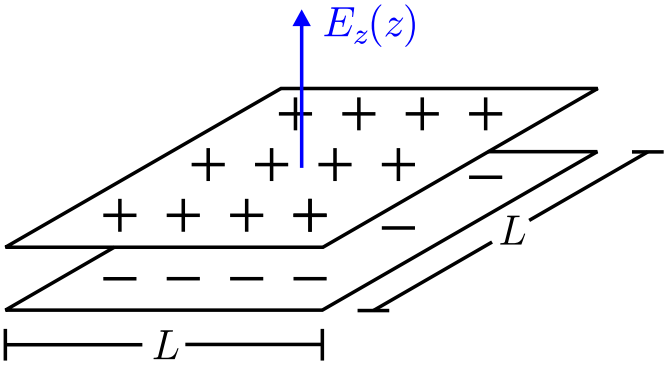

Figure 6.3: Schematic of the dipole sheet used to model the electric field.

The first assumption is that there is a fixed number of equivalent adsorption sites on the surface, and only one atom can occupy each site. Also, the interaction between adsorbates in neglected. By equating the chemical potential of a 3D ideal gas with that of a 2D gas with energy E_a the Langmuir isobar is [132],

$$\frac{\theta}{1-\theta} = Ce^{\frac{E_a}{k_B T_q}}, \tag{6.7}$$

where T_q is the temperature of the quartz. In Eq. 6.7, θ varies from 0 to 1. As T_q increases the coverage decreases. Physically this is due to thermal desorption, the surface is adding more energy to the adsorbates allowing them to break the bond to the surface.

The coefficient, C depends on the translational, vibrational, and rotational partition functions of the 2D and 3D gas. To describe this experiment the vibrational and rotational partition function are unity for the 3D gas of Rb, and the translational partition function is that of an ideal gas. The adsorbates on the surface are assumed to stay adsorbed to one site. The atom can be bound

in different vibrational states of the potential formed at the surface. Under the assumption that the adsorbate is deeply bound and remains in the same vibrational state, the translational, vibrational, and rotational partition are all unity [133]. Using these assumptions, C is,

$$C = \frac{ph^3}{k_B T_{\text{gas}} (2\pi m k_B T_{\text{gas}})^{3/2}}, \tag{6.8}$$

where T_{gas} is the temperature of the background atoms, and p is the pressure.

6.2.5 Blackbody Ionized Electrons

As discussed in Section 2.1.3, blackbody radiation can ionize Rydberg atoms. As a result of the ionization, a free electron with a small amount of kinetic energy is produced. These slow electrons have been a central focus in the investigation of avalanche ionization in Rydberg gases [134, 135, 136], and the positive ions have been used in Stark spectroscopy [137]. In these experiments, the ionized electrons are attracted to the positive adsorbate potential. If the electrons have too much kinetic energy, then the force from the potential will be negligible.

The kinetic energy of an electron, $\Delta\bar{E}_e$ can be calculated following the approach of [135],

$$\Delta\bar{E}_e = \bar{E}_{bb} - E_{\text{Ryd}}, \tag{6.9}$$

where, $E_{\text{Ryd}} = 1/n^{*2}$, is the absolute value of the energy level of the Rydberg

atom, and $\bar{E}_{bb}$ is the average energy of an absorbed blackbody photon,

$$\bar{E_{bb}} = \frac{\int_{E_{\mathrm{Ryd}}}^{\infty} E_{bb}\sigma_{E_{\mathrm{Ryd}}}(E_{bb})\frac{E_{bb}^2}{e^{E_{bb}/(k_B T)}-1}dE_{bb}}{\int_{E_{\mathrm{Ryd}}}^{\infty} \sigma_{E_{\mathrm{Ryd}}}(E_{bb})\frac{E_{bb}^2}{e^{E_{bb}/(k_B T)}-1}dE_{bb}}. \tag{6.10}$$

$\sigma_{E_{\mathrm{Ryd}}}(E_{bb})$ is the photoabsorption cross section for photons with energy E_{bb} for a Rydberg state with energy, $-E_{\mathrm{Ryd}}$, where,

$$\sigma_{E_{\mathrm{Ryd}}}(E_{bb}) \propto E_{bb}(E_{\mathrm{Ryd}}^{3/4}E_{bb}^{-5/3})^2. \tag{6.11}$$

Electrons blackbody ionized from the $81D_{5/2}$ state have an average kinetic energy, $\Delta\bar{E}_e = 9.26\,\mathrm{meV}$. For $n = 40 - 100$ the kinetic energies range from $\Delta\bar{E}_e = 7.92 - 15.16\,\mathrm{meV}$. The energies are consistent with complimentary calculations [59].

6.3 Experimental Results

Using Rydberg atom EIT with absorption imaging the electric field near quartz is measured. The electric field near the quartz surface is determined by measuring the frequency shift of the Rydberg state, and comparing the observed shift to a Stark shift calculation. The electric field was measured at a distance of $500\,\mu$m from the surface for a range of different quartz temperatures from $28\,^{\circ}$C to $80\,^{\circ}$C. Data was taken in two different regimes, high and low Rydberg atom population. The amount of Rydberg excitation was controlled by changing Ω_p. The results for low Rydberg atom population is shown in black in Fig. 6.4. Over

the temperature range sampled the electric field is reduced by a factor of 34, from 1.7 V/cm to 0.05 V/cm. The reduction of the electric field is due to the thermal desorption. From the spatial variation of the field, the size of the adsorbate patch is calculated to be, $L = 10\,\text{mm}$ at $T_q = 28\,^\circ\text{C}$. The calculated dipole density, $P = 5 \times 10^6\,\text{D}/\mu\text{m}$, is consistent with the dipole density observed in an experiment with Rb adsorbates on evaporated SiO_2 [114]. Assuming a constant L with increasing T_q, the electric field is only dependent on the dipole density P. Using the dipole moment per adatom of Eq. 6.5, the adsorbate density is,

$$\rho_a = \frac{P}{d(\rho_a)}. \tag{6.12}$$

Combining Eq. 6.5, 6.7, and 6.12, the data in black is fit to C and E_a, and is plotted as the black line. The fit yields an activation energy of $E_a = 0.66 \pm 0.2\,\text{eV}$, which is consistent with the measured E_a of alkali atoms on similar surfaces [120, 138, 139, 140]. At $T_q = 28\,^\circ\text{C}$, the coverage is, $\theta = 0.11$, and the average spacing between Rb atoms is $\sim 1.5\,\text{nm}$.

From the fit, $C = 1 \times 10^{-12}$. C can also be calculated for experimental parameters using Eq. 6.8. Eq. 6.8 needs to be slightly modified because it assumes adsorption is due to background gas. In the experiment the main source of the Rb adsorbate electric field is the MOT atoms. Disabling the magnetic trap for $\sim 10\,\text{min}$ did not change the electric field, however, disabling the MOT for the same period changes the electric field. Using the ideal gas law, $P = \rho k_B T_{\text{gas}}$, where ρ is the density of atoms in the MOT. With the estimated parameters of

the MOT during the loading phase of, $\rho = 1 \times 10^7\,\mathrm{atoms/cm^3}$, and $T_{\mathrm{gas}} = 1\,\mathrm{mK}$ yields, $C = 2 \times 10^{-12}$.

For one ML of Rb, Fig. 6.1 shows lowest bound state of an adsorbate has an energy of, $E_b = 0.35\,\mathrm{eV}$. For the lower experimentally investigated coverages, the DFT calculations show an increase of E_b by ~ 1.4 to $0.49\,\mathrm{eV}$. The energy of the bound state is the least amount of thermal energy needed to desorb an atom. Depending on the details of the atom-surface bond and desorption dynamics more thermal energy is needed. The calculated E_b at low coverages is comparable in magnitude with the measured E_a, and is consistent with the expectation $E_b \leq E_a$ [141, 142].

The electric field from the adsorbates points away from the surface as confirmed by applying an external compensating field. From the calculations outlined in Appendix A, the electric field is estimated to point perpendicular to the surface to within 15°. This estimate is the result of the good agreement between the overall and differential shifts of the different m_J states, for a variety of n used in experiments.

Over the extent of the magnetic trap the electric field was observed to be homogeneous. An inhomogeneous electric field across the atomic sample would cause a broadening of the EIT resonance, since the absorption images reveal the OD over the $\sim 2\,\mathrm{mm}$ depth of the sample. The width of the EIT signal was not detectably broadened, and variation of the electric field measured in the

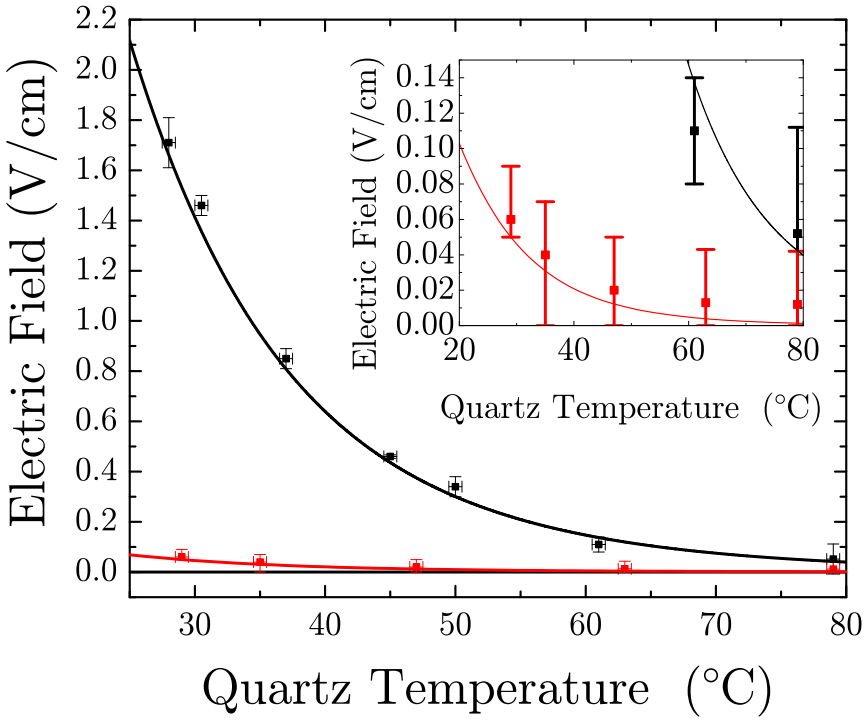

Figure 6.4: The measured electric fields due to Rb adsorbates on the (0001) surface of quartz as a function temperature, at a distance of 500 μm from the surface. The black points the result of experimental data taken in the limit of low Rydberg atom production. The black line is a fit to the Langmuir isobar of Eq. 6.7. The red data points were taken with high Rydberg atom production. The horizontal error bars are due to the uncertainty in the temperature, T_{q}. The vertical errors bars are the standard deviation of the experimental data. In the case of high (low) Rydberg atom production the Rabi frequencies of the probe and coupling lasers are $\Omega_p = 2\pi \times 3.5(0.5)$ MHz and $\Omega_c = 2\pi \times 4(4)$ MHz.

z-direction is $< 0.1\,\mathrm{V/cm}$. These observations indicate that the Rb is spread out evenly on the surface and is not forming large clusters on the surface. If large clusters are formed then Brunauer–Emmett–Teller (BET) theory needs to be used instead of the Langmuir equation [143].

The data in black is taken with minimal Rydberg atom population. The Rabi frequencies of the probe and coupling were, $\Omega_p = 2\pi \times 0.5\,\mathrm{MHz}$ and $\Omega_c = 2\pi \times 4\,\mathrm{MHz}$. If Ω_p is increased to $2\pi \times 3.5\,\mathrm{MHz}$, the measured electric field is greatly reduced. The data with the increased probe Rabi frequency is plotted as the red points in Fig. 6.4. At $T_q = 28\,^{\circ}\mathrm{C}$ the electric field is reduced by a factor 30. The reduction in the electric field is due to electrons binding to the surface and partially canceling out the electric field from the adsorbates. Blackbody ionization of Rydberg atoms is the source of the slow electrons. With the increase in probe Rabi frequency, the amount of atoms that are blackbody ionized increases by a factor of 20. This is calculated by solving the density matrix equations time dependently for the experimental parameters, including an extra state for blackbody decay from the Rydberg state.

The electric field from the electrons on the surface is modeled as a square sheet of length L_e with uniform charge density, σ,

$$E_e(z) = \frac{\sigma}{\pi\epsilon_0} \tan^{-1}\left(\frac{L_e^2}{z\sqrt{2L_e^2 + z^2}}\right). \tag{6.13}$$

The total electric field is the sum of the electric field from the adsorbates and

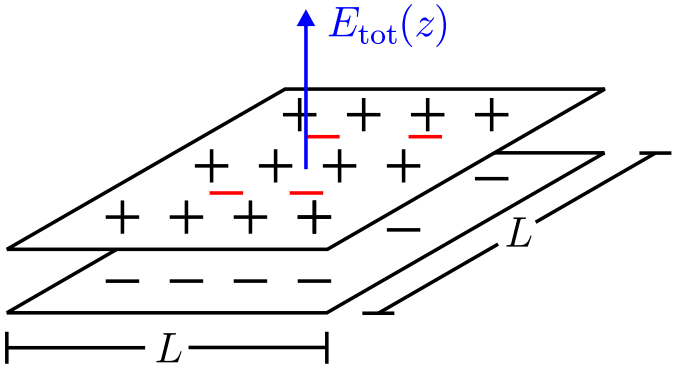

Figure 6.5: Schematic of the dipole and electron sheet used to model the electric field.

the electrons,

$$E_{\mathrm{tot}}(z) = E(z) + E_e(z). \tag{6.14}$$

Experimentally it is observed that after prolonged Rydberg excitation the electric field reaches a steady state value, indicating that the surface is saturated with electrons. The surface saturation suggests the electric field from the electrons completely cancels the electric fields from the adsorbates. Requiring $E_{\mathrm{tot}}(0) = 0$, and using the black line in Fig. 6.4, with $L_e = L$, the charge density σ for the electrons is calculated. Using this information, $E_{\mathrm{tot}}(z)$ can be calculated, and is plotted as the red line in Fig. 6.4. The overlap of the experimental data with the calculation is an indication that the reduction of electric fields is due to the binding of the electrons on the surface.

Using the calculated charge density of the electrons, σ, the number and density of electrons on the surface can be calculated. At $T_q = 28\,^{\circ}\mathrm{C}$, $\sigma =$

200 electrons/mm^2, with a total of 20,000 electrons of the surface. During experiments with $\Omega_p = 2\pi \times 3.5\,\text{MHz}$, 200 Rydberg atoms are ionized during each experiment sequence, compared to 10 electrons when $\Omega_p = 2\pi \times 0.5\,\text{MHz}$.

6.4 Electrons on Liquid Helium

This system closely resembles that of electrons bound to the surface of liquid helium [144, 145, 146]. The electrons are bound in the Coulomb potential near the surface due to their image potential,

$$V(z) = \frac{(\epsilon - 1)e^2}{4(\epsilon + 1)z} \quad \text{for } x > 0, \tag{6.15}$$

where, ϵ is the static dielectric constant. A potential wall at the surface prevents low energy electrons from penetrating into the bulk liquid helium, and the electrons are trapped in the Coulomb states. The potential wall at the surface is due to the negative electron affinity(NEA) of the surface [147].

In semiconductors and insulators, electron affinity, χ, is defined as [128],

$$\chi = E_{\text{vac}} - E_{\text{boc}}, \tag{6.16}$$

where E_{vac} is the energy level of the vacuum, and E_{boc} is the energy level of the bottom of the conduction band. This is shown schematically in Fig. 6.6. When $\chi < 0$, E_{vac} is in the band gap below the bottom of the conduction band E_{boc}. Since the Fermi energy, E_F lies in the band gap all of the electronic states in the valence band are filled. A barrier is created where an electron needs kinetic energy to access states in the conduction band.

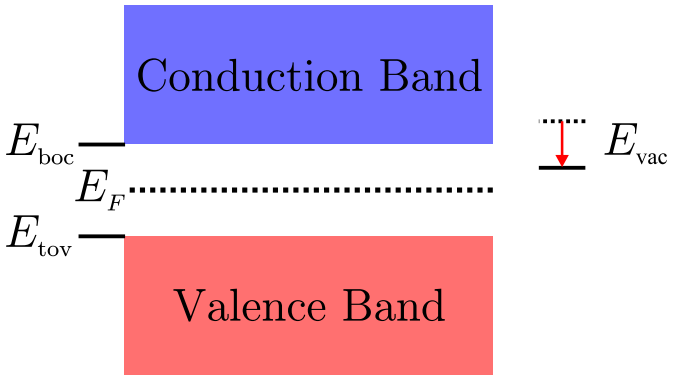

Figure 6.6: Diagram of the general band structure of an undoped semiconductor or insulator. If $E_{\text{vac}} > E_{\text{boc}}$, then the surface has a positive electron affinity. Conversely, if $E_{\text{vac}} < E_{\text{boc}}$ the surface has a negative electron affinity.

In liquid helium the height of this barrier is 1 eV. Approximating the barrier as infinite in height the 1D Schrödinger equation, equivalent to that of a 1D hydrogen atom can be solved. Eigenenergies are in agreement with spectroscopic measurements [148, 149].

Electrons on the surface of liquid helium can remain bound for tens of hours [146]. Surface states exist on surfaces that have a positive electron affinity such as copper, lithium and silver, however their lifetimes are short, usually on the order of ~ 10 fs [150]. Liquid helium is not the only surface demonstrated to have a negative electron affinity and bind electrons on the surface. Other surfaces include liquid H_2, and liquid Ne [146].

6.5 Inducing Negative Electron Affinity

The surface of quartz, like most materials, has a positive electron affinity. It has been experimentally measured to be 1 eV [151, 152]. However, through adsorption of atoms or molecules the electron affinity of a surface can be shifted. If the shift is large enough a negative electron affinity can be induced. Through adsorption of a similar alkali atom cesium, materials such as diamond, gallium nitride, aluminum nitride, and boron nitride [153, 154, 155, 156, 157], can shift the electron affinity of their surface from positive to negative.

Using DFT, the density of states, as well as the vacuum energy with varying amounts of Rb coverage is calculated, Fig. 6.7. E_F is set equal to zero, and lies in the middle of the band gap. The energies of the top of the valence band, E_{tov}, and bottom of the conduction band, E_{boc}, of bulk quartz are at ± 3.05 eV and indicated by the purple and green lines respectively. Consistent with experiment, the vacuum energy of a clean surface, $\overline{V}_{\text{clean}}(\infty)$ is above E_{boc} indicating a positive electron affinity. As the Rb coverage increases the vacuum level shifts downward, and a negative electron affinity is induced around 0.5 ML.

The shift in electron affinity can also be calculated using electrostatic methods. The atomic dipoles on the surface create an electric field that lowers E_{vac}. The shift in electron affinity can be calculated using [130],

$$\Delta\chi = -\frac{ed(\rho_a)\rho_a}{\epsilon_0}. \tag{6.17}$$

With the calculated dipole moment, $d_0 = 12$ D, and experimental values for

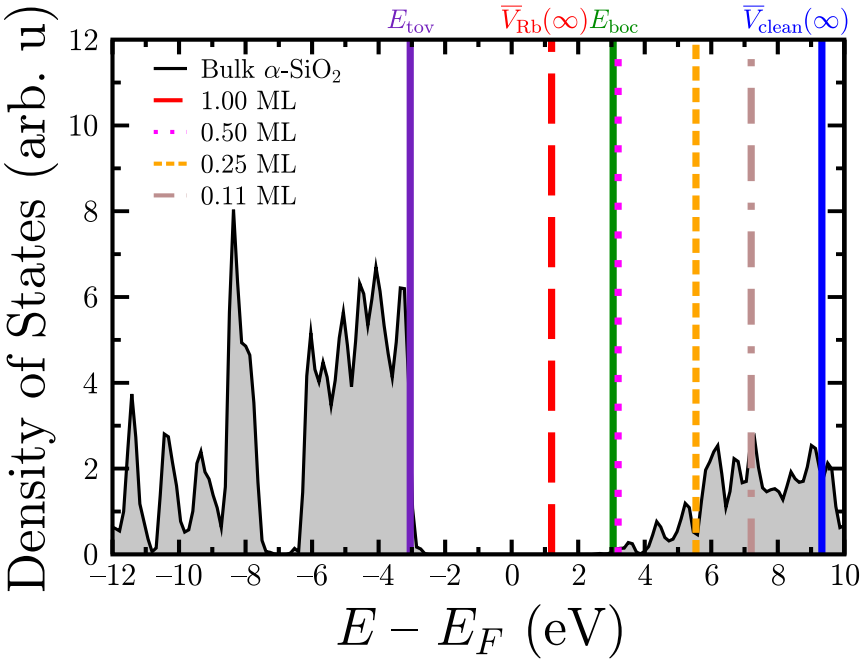

Figure 6.7: Density of states of bulk α-quartz from DFT calculations. The energy of the bottom of the conduction band, E_{boc} is shown in green. The vacuum energies are plotted for a clean surface (blue), and for increasing Rb coverage. Increasing the amount of Rb coverage shifts the vacuum level down in energy. With one ML of Rb on the surface (red line), the vacuum energy dips below the bottom of the conduction band (green line), indicating the formation of a NEA surface.

$\rho_a = 4.2 \times 10^5\,\mathrm{atoms}/\mu\mathrm{m}^2$ at $T = 28\,^{\circ}\mathrm{C}$, $\Delta\chi = -1.9\,\mathrm{eV}$. Combining this shift with the experimental value of $\chi = 1\,\mathrm{eV}$, indicates onset on a NEA surface at $28\,^{\circ}\mathrm{C}$. This model shows a NEA surface up to $\sim 40\,^{\circ}\mathrm{C}$.

6.6 Surface Potential

The potential that an electron experiences is a combination of its image potential and a potential created from the adsorbates on the surface. The image potential will dominate at distances close to the surface, while far away from the surface the adsorbate potential will dominate. Using Eq. 6.15 with $\epsilon = 3.85$ for quartz [158], the image potential for an electron is calculated. The potential from the adsorbate field can be calculated by integrating Eq. 6.6. The total potential is plotted in Fig. 6.8. At distances of $\sim$ mm from the surface, the adsorbate field dominates and attract electrons toward the surface. When the electron is near the surface the image potential is dominant. The lowest bound state in the image potential has an energy of 0.3 eV. Note that the kinetic energies of the blackbody electrons is much lower than these energy scales. The electron will collide with the surface and needs to lose its kinetic energy in order to be trapped. The loss in energy can be mediated by the surface, similar to the adsorption of an atom on a surface. As electrons are added to the surface, the adsorbate part of the potential is lowered.

6.7 Small Fields Near The Surface

Since the electric field is reduced at high temperature and high Rydberg atom population, the electric field close the surface is investigated in this limit. With $T_q = 79\,^{\circ}\mathrm{C}$, and $\Omega_p = 2\pi \times 3.5\,\mathrm{MHz}$, the measured electric field is shown in black

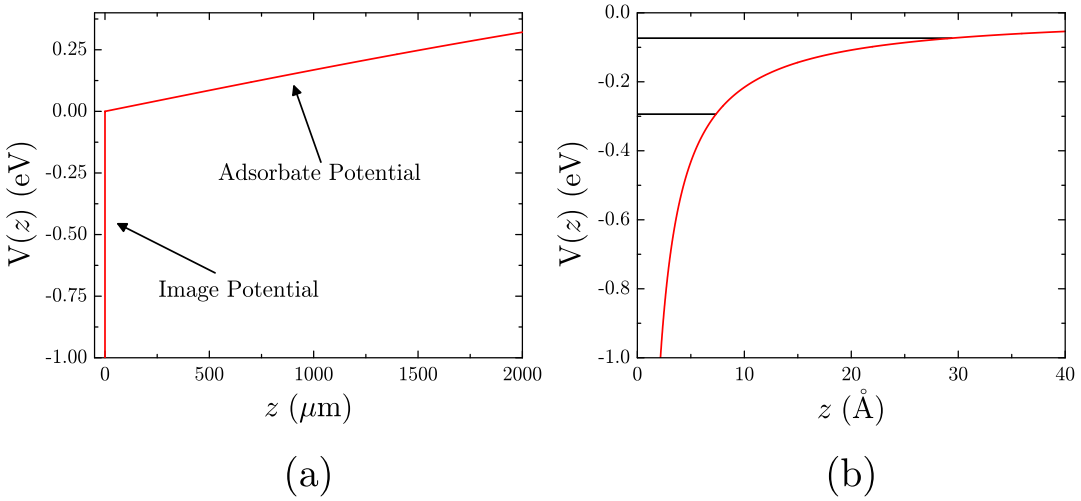

Figure 6.8: Plots of the potential for an electron above the quartz surface. (a) The long range potential is due to the adsorbates of the surface. As electrons accumulate on the surface this part of the potential decreases. (b) A zoomed in look at the image potential for an electron on quartz. The black lines indicate the energies of the first two bound states.

in Fig. 6.9. For $z > 200\,\mu$m the electric field is negligible within experimental error. For $z < 200\,\mu$m the electric field increases to $E =\sim 30\,\mathrm{mV/cm}$, $20\,\mu$m from the surface. As can be seen in the experimental traces, Fig. 6.10, the width of the EIT resonance increases from 2 MHz far from the surface to 4 MHz for $z \leq 50\,\mu$m.

Under experimental conditions the estimated electron density is ~ 10 electrons/mm^2, yielding an average electron spacing of $\sim 300\,\mu$m. At distances less that the electron spacing, Eq. 6.13 breaks down, and the electric field becomes inhomoge-

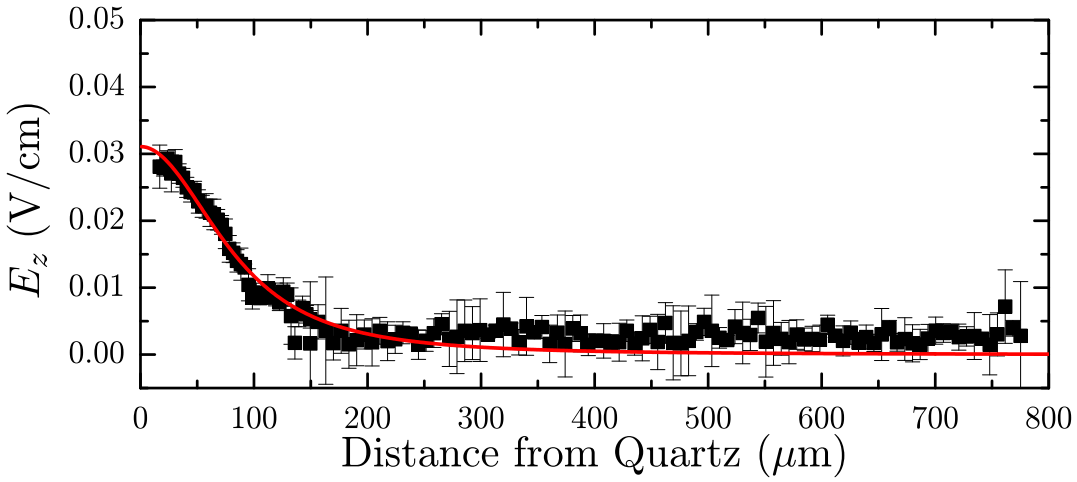

Figure 6.9: In the limit of large numbers of Rydberg atoms, the electric field is measured at distances of $\sim$ 20–800 μm from the quartz surface at $T_q = 79\,^{\circ}\mathrm{C}$. The electric field is calculated using the difference in frequency shifts of the $m_J = 1/2$ and 5/2 states of the $81D_{5/2}$ state. Black points are taken from different pixels on the CCD camera. The error bars are the standard deviation of the measurement. The red line is a fit to Eq. 6.6, showing the inhomogeneity of the electric field. Calculations indicate that the electric field at $z < 200\,\mu$m is caused by the large spacing between the electrons.

neous. The red line in Fig. 6.9 is a fit to Eq. 6.6, with $L = 200\,\mu$m, demonstrating the inhomogeneity of the field.

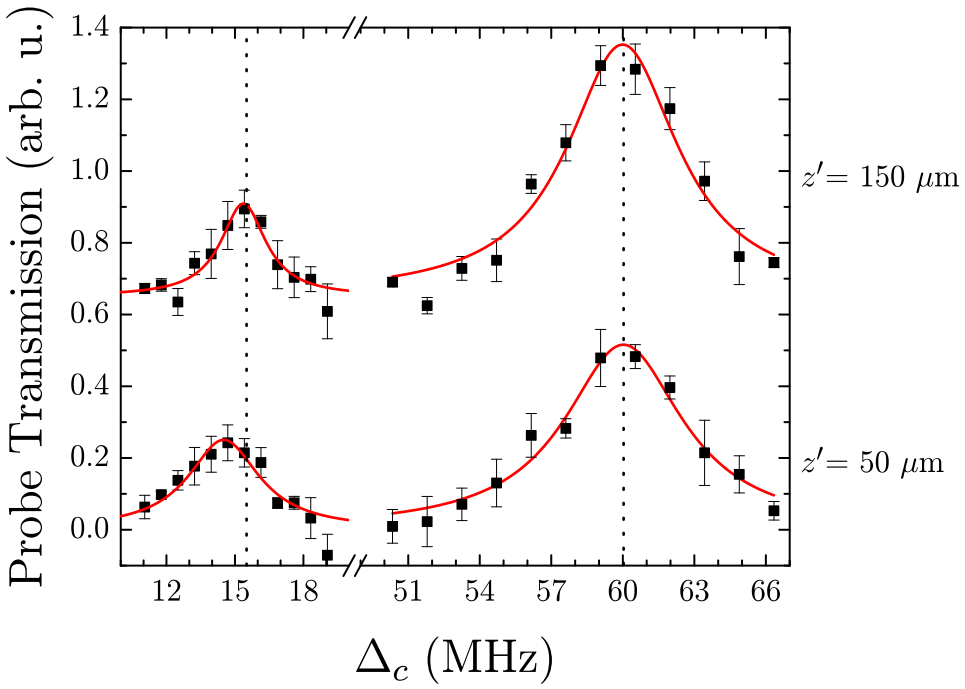

Figure 6.10: EIT spectra taken at 2 different positions $z = 150\,\mu$m (upper) and $z = 50\,\mu$m (lower) for $81D_{5/2}$ $m_J = 1/2$ (left) and $m_J = 5/2$ (right). The black points are pixel values of 3 averaged images, and the error bars are the standard deviation of the pixel values. The red lines are Lorentzian fits to the data. At $z = 50\,\mu$m the $m_J = 1/2$ state is broadened and shifted corresponding to an electric field of 0.02 V/cm. The dashed lines indicate the zero electric field frequencies for the $m_J = 5/2$ and 1/2 states.

6.8 Electron Photodesorption with UV LEDs

The electrons on the surface can be removed by using UV light. The UV light is generated by light emitting diodes (LEDs) with emission centered at 400 nm. The LEDs are placed below the quartz surface outside vacuum and are directed

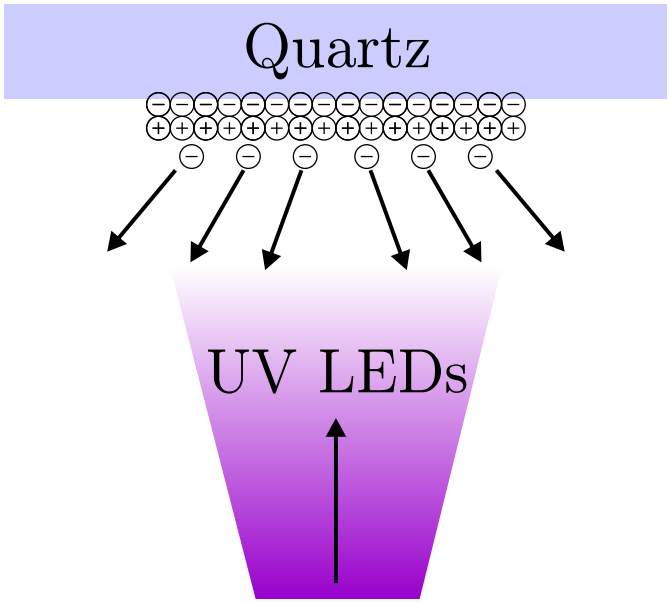

Figure 6.11: Schematic of the setup used to remove electrons from the quartz surface. The light from the LEDs is applied through a viewport on the bottom of the vacuum chamber.

upward as shown in Fig. 6.11. The effects of varying pulse lengths of UV light is studied. Before every UV pulse, the surface is saturated with electrons. During the MOT loading sequence the LEDs are pulsed on for a variable amount of time. After the pulse, the electric field near the surface is measured. A plot of the electric field with the substrate at 56 °C is shown in Fig. 6.12a. As the pulse length increases the electric field also increases until in reaches a constant value, $\sim 0.2\,\mathrm{V/cm}$. The data is fit to,

$$E(t) = A(1 - e^{-bt}), \tag{6.18}$$

where b is the photodesorption rate constant. Eq. 6.18 is motivated by the study of photodesorption of atoms and molecules [159, 160]. From the fit to

Eq. 6.18, the photodesorption rate constant, b, is extracted. b was measured for several different temperatures and was found to change significantly. The results are shown in Fig. 6.12(b). The changing rate constant suggests that the electron binding is changing with quartz temperature. The data in Fig. 6.12(b) is fit to an Arrhenius equation similar to Eq. 6.7, with an activation energy of $0.7 \pm 0.07\,\mathrm{eV}$. The activation energy is consistent with that of the Rb adsorption, which suggests that the electron binding is strongly dependent on the amount of Rb on the surface.

The surface is not only sensitive to light at 400 nm, but to visible light as well. Careful alignment of the coupling beam is needed to avoid clipping the quartz and generating large electric fields. Changing electric fields were also seen using a helium-neon laser to illuminate the surface, and sensitivity to ambient room lights was also observed. The area around the optical table and chamber is shielded from abient light. Changing the power of the MOT beams incident on the quartz by a factor of 2 does not change the electric field on the surface. Equivalently using the same power as the MOT beams, light at 1064 nm also does not change the electric field.

6.9 Conclusions

Adsorbate electric fields near the surface of the (0001) surface of quartz have been characterized. In the limit of low Rydberg atom excitation, Rb adsorption follows

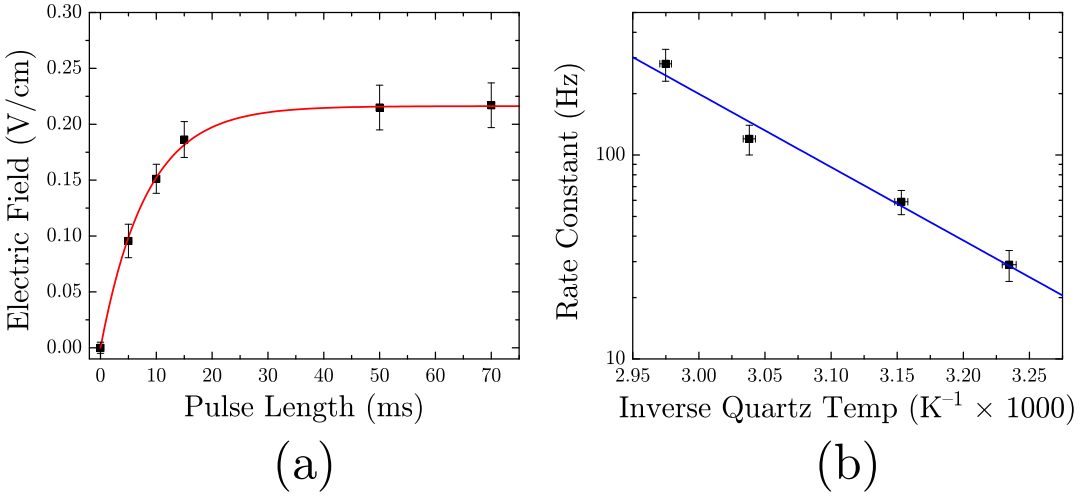

Figure 6.12: (a) The increase of the electric field with the pulse duration at $T_q = 56\,^{\circ}\mathrm{C}$. The black points are experimental data, and the error bars are the standard deviation of the measurement. The red line is a fit to $E(t) = A(1 - e^{-bt})$, where the photodesorption rate constant b is extracted from the fit. (b) Plot of b measured for different quartz temperatures. The error bars are the uncertainty in the fit of the data to b. The blue line is a fit of the data to an Arrhenius equation, with an activation energy of $0.7 \pm 0.07\,\mathrm{eV}$.

the theory of Langmuir adsorption, with an activation energy, $E_a = 0.66\,\mathrm{eV}$. Measurements of the dipole density and E_a are consistent with experimental results of other groups. Electric fields can be reduced by increasing the quartz temperature and thermally desorbing Rb from the surface. Results of DFT calculations were presented that investigated the microscopic nature of Rb binding to the (0001) surface of quartz. The calculations reveal that the Rb atoms are bound to two different oxygen atoms on the surface.

Increasing the amount of Rydberg atom excitation reduces the electric field even further. Electric fields as low as 30 mV/cm have been measured 20 μm from the surface. Electrons binding to the surface and canceling out the electric field from the Rb adsorbates are responsible for the small magnitude of the field. With the reduction in the field, it is shown that coherent excitation of Rydberg atoms at high principal quantum numbers is possible near a quartz surface. To date, most experiments involving Rydberg atoms near surface use states with $n \leq 50$. The ability to use Rydberg atoms with higher n includes the advantages of longer lifetimes and stronger Rydberg-Rydberg interactions.

Chapter 7

Conclusions and Future Directions

In this thesis, measurements of microwave and dc electric fields have been made. The fields were measured using Rydberg atom EIT as a spectroscopic tool. In recent years, the use of Rydberg EIT has been steadily increasing due to its experimental simplicity and non-invasiveness. The theoretical basics of 3 and 4-level EIT are discussed. Experimental and theoretical results have been presented showing the viability of using Rydberg EIT in vapor cells to measure the absolute electric field and polarization of microwaves. These methods have reached amplitudes as low as $8\,\mu$V/cm and an angular resolution of $0.5°$. With technical improvements in the experiment, and new ideas, these limits will soon be surpassed.

Since the results presented here, the microwave experiment has been moved over to a different setup in our lab using Cs. It has demonstrated spatial sensitivity [86], as well as insensitivity to perturbations of the electric field from the vapor cell [85]. Some of the current efforts include using FM spectroscopy to push the sensitivity toward the standard quantum limit, and use a 3-photon scheme for Rydberg excitation to cancel out the Doppler shift.

Rydberg EIT near a quartz surface has been used to show low electric fields. Electrons binding to the surface are responsible for the fields that can be as low as $30\,\mu$V/cm at a distance of $20\,\mu$m from the quartz surface. It is possible

that increasing the quartz temperature could push the minimum electric field down even further. DFT and electrostatic calculations qualitatively agree with the induction of a NEA of the surface of quartz. Perhaps these results can encourage more theoretical and experimental work on atom-surface interactions. The experimental results shown in Chapter 6 show that Rydberg atom-surface experiments are indeed possible.

Many pieces of experimental apparatus were designed and constructed. The design and operation of a bow-tie cavity for generation of 480 nm light was described. The system has been used successfully in both microwave and surface experiments, and currently is being used in an atom-cavity experiment in our lab. The cold atom apparatus including the magnetic trap is a robust environment for the study of Rydberg atoms in free space or near a surface.

Extensions of the work with the Rb-quartz system will be focussed on determining the details of the electron binding. One of the biggest questions is, are electrons bound to individual adsorbates, or are they a 2D gas? In an attempt to answer this question, we plan to measure the mobility of electrons in a similar fashion to experiments done with electrons on liquid helium [161, 162]. To do the experiment, the gold mirror needs to be modified into three different electrodes as shown in Fig. 7.1. An ac voltage is sent to one of the electrodes. The electrons on the surface move back and forth and couple the ac signal to the output electrode. The relative phase shift is dependent on the phase shift between the input and output signals.

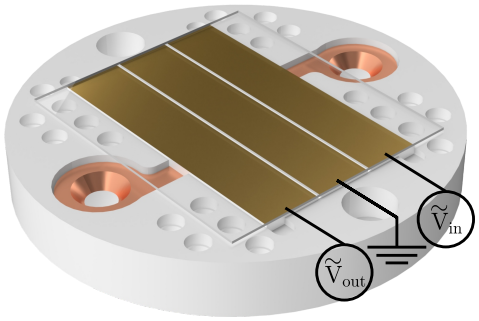

Figure 7.1: Schematic of a future experiment. The gold mirror for the mirror-MOT is turned into 3 electrodes. Electrons on the surface will transfer the signal on the input electrode to the output electrode.

In its current state the experiment is setup to study the coupling of Rydberg atoms to surface phonon polaritons on quartz. Transitions between Rydberg states have frequencies that overlap with frequencies of surface-phonon-polaritions on dielectric materials such as quartz. In the near-field, the coupling between the Rydberg atom and surface-phonon-polaritons enhances the atomic decay, transferring the energy of the excitation to the surface [163].

The lowest frequency surface-polarition mode in quartz has a frequency of 3.8 THz [164]. To achieve sufficient coupling the atoms need to be in the near-field, $\lambda/2\pi = 12\,\mu$m. Imaging the atoms this close to the surface is pushing the limit of direct absorption imaging. An alternative is to use grazing incident imaging [112]. With grazing incident imaging, the imaging beam is incident upon the mirror at a small angle, and due to the reflection off of the mirror two images of the atomic cloud are produced. The distance between the two images in the plane of the CCD camera are related to the distance of the atoms from the

surface. The 500 μm thickness of the quartz prevents us from imaging at angles of a few degrees that are typically used. One possible solution is to set up the absorption imaging along a different axis and use an incident angle close to 45°.

Another possible experiment is to use a material that has lower frequency surface polarition modes. For natural dielectrics, there is not a large variance of the lowest resonance frequencies. A solution that our group has theoretically investigated is to artificially construct periodically poled materials that can have lower frequency modes, $\sim 500\,\mathrm{MHz}$ to $5\,\mathrm{GHz}$ [165]. Using this approach atom-surface coupling can be in the strong-coupling regime at mm-distances.

The measurements in this thesis describe measurements of dc fields and resonant microwave fields. Recently, techniques for measuring non-resonant electric fields are being developed by other groups. In [121], electric field noise near the surface of an atom chip was measured by using microwaves to drive spin-echo and spin-locking sequences between two Rydberg states. In [64, 166, 167], rf signals with frequencies from $10\,\mathrm{kHz} - 100\,\mathrm{MHz}$ have been applied to vapor cells via external electrodes. The applied electric fields are measured with Rydberg atom EIT. With some modifications both the vapor cell and surface experiments could be adapted to study non-resonant ac electric fields. This could prove to be useful in characterizing the frequency characteristics of adsorbate electric fields that have plagued surface ion trapping efforts.

With the work presented here combined with the work of others, atom based sensing of electric fields is a promising and rapidly advancing area of research.

Specifically measurement of electric fields with Rydberg atom EIT has been shown to be a robust and minimally invasive measurement tool. There are numerous applications of these senors including as an electric field standard, characterizing passive intermodulation in microwave circuits, detecting geoelectromagnetic noise, and measuring electric fields near surfaces.

References

[1] M. Fleischhauer, A. Imamoglu, and J. P. Marangos, Rev. Mod. Phys. **77**, 633 (2005).

[2] C. L. Garrido Alzar, M. A. G. Martinez, and P. Nussenzveig, Am. J. Phys. **70**, 37 (2002).

[3] J. A. Souza, L. Cabral, R. R. Oliveira, and C. J. Villas-Boas, Phys. Rev. A **92**, 023818 (2015).

[4] D. Meschede, *Optics, Light and Lasers* (Wiley-VCH Verlag GmbH & Co. KGaA, 2008).

[5] J. P. Marangos, J. Mod. Opt. **45**, 471 (1998).

[6] J. Vanier and C. Audoin, *The Quantum Physics of Atomic Frequency Standards Volume 1* (Adam Hilger, 1989).

[7] T. L. Nicholson, S. L. Campbell, R. B. Hutson, G. E. Marti, B. J. Bloom, R. L. McNally, W. Zhang, M. D. Barrett, M. S. Safronova, G. F. Strouse, W. L. Tew, and J. Ye, Nat. Commun. **6**, 6896 (2015).

[8] D. Sheng, S. Li, N. Dural, and M. V. Romalis, Phys. Rev. Lett. **110**, 160802 (2013).

[9] A. D. Cronin, J. Schmiedmayer, and D. E. Pritchard, Rev. Mod. Phys. **81**, 1051 (2009).

[10] J. Fang and J. Qin, Sensors **12**, 6331 (2012).

[11] S. Knappe, P. D. D. Schwindt, V. Shah, L. Hollberg, J. Kitching, L. Liew, and J. Moreland, Opt. Express **13**, 1249 (2005).

[12] P. D. D. Schwindt, S. Knappe, V. Shah, L. Hollberg, J. Kitching, L.-A. Liew, and J. Moreland, Appl. Phys. Lett. **85**, 6409 (2004).

[13] J. Stuhler, Nat. Phys. **11**, 293–295 (2015).

[14] E. Thoreson, *Evolution of Cyber Technologies and Operations to 2035* (Springer, 2015), pp. 91–105.

[15] D. K. Doughty and J. E. Lawler, Appl. Phys. Lett. **45**, 611 (1984).

[16] C. A. Moore, G. P. Davis, and R. A. Gottscho, Phys. Rev. Lett. **52**, 538 (1984).

[17] B. N. Ganguly and A. Garscadden, Phys. Rev. A **32**, 2544 (1985).

[18] G. Kurizki, P. Bertet, Y. Kubo, K. Mølmer, D. Petrosyan, P. Rabl, and J. Schmiedmayer, Proc. Natl Acad. Sci. **112**, 3866 (2015).

[19] C. Sias and M. Köhl, arXiv:1401.3188 (2014).

[20] A. Jöckel, A. Faber, T. Kampschulte, M. Korppi, M. T. Rakher, and P. Treutlein, Nat. Nanotechnol. **10**, 55 (2015).

[21] J. S. Douglas, H. Habibian, C.-L. Hung, A. Gorshkov, H. J. Kimble, and D. E. Chang, Nat. Photon. **9**, 326 (2015).

[22] N. Daniilidis and H. Häffner, Annual Review of Condensed Matter Physics **4**, 83 (2013).

[23] D. Petrosyan, G. Bensky, G. Kurizki, I. Mazets, J. Majer, and J. Schmiedmayer, Phys. Rev. A **79**, 040304 (2009).

[24] H. Kübler, D. Booth, J. Sedlacek, P. Zabawa, and J. P. Shaffer, Phys. Rev. A **88**, 043810 (2013).

[25] J. Pritchard, J. Isaacs, M. Beck, R. McDermott, and M. Saffman, Phys. Rev. A **89**, 010301 (2014).

[26] E. A. Hinds, K. S. Lai, and M. Schnell, Phil. Trans. R. Soc. Lond. A **355**, 2353 (1997).

[27] F. Bariani, J. Otterbach, H. Tan, and P. Meystre, Phys. Rev. A **89**, 011801 (2014).

[28] M. Gao, Y. X. Liu, and X.-B. Wang, Phys. Rev. A **83**, 022309 (2011).

[29] C. Hermann-Avigliano, R. C. Teixeira, T. L. Nguyen, T. Cantat-Moltrecht, G. Nogues, I. Dotsenko, S. Gleyzes, J. M. Raimond, S. Haroche, and M. Brune, Phys. Rev. A **90**, 040502 (2014).

[30] T. Thiele, S. Filipp, J. A. Agner, H. Schmutz, J. Deiglmayr, M. Stammeier, P. Allmendinger, F. Merkt, and A. Wallraff, Phys. Rev. A **90**, 013414 (2014).

[31] R. C. Teixeira, C. Hermann-Avigliano, T. L. Nguyen, T. Cantat-Moltrecht, J. M. Raimond, S. Haroche, S. Gleyzes, and M. Brune, Phys. Rev. Lett. **115**, 013001 (2015).

[32] S. B. Hill, C. B. Haich, Z. Zhou, P. Nordlander, and F. B. Dunning, Phys. Rev. Lett. **85**, 5444 (2000).

[33] E. So, M. Dethlefsen, M. Ford, and T. P. Softley, Phys. Rev. Lett. **107**, 093201 (2011).

[34] H. Kübler, J. P. Shaffer, T. Baluktsian, R. Löw, and T. Pfau, Nat. Photon. **4**, 112 (2010).

[35] J. D. Carter, O. Cherry, and J. D. D. Martin, Phys. Rev. A **86**, 053401 (2012).

[36] H. Hattermann, M. Mack, F. Karlewski, F. Jessen, D. Cano, and J. Fortágh, Phys. Rev. A **86**, 022511 (2012).

[37] K. S. Chan, M. Siercke, C. Hufnagel, and R. Dumke, Phys. Rev. Lett. **112**, 026101 (2014).

[38] A. Tauschinsky, R. M. T. Thijssen, S. Whitlock, H. B. van Linden van den Heuvell, and R. J. C. Spreeuw, Phys. Rev. A **81**, 063411 (2010).

[39] R. P. Abel, C. Carr, U. Krohn, and C. S. Adams, Phys. Rev. A **84**, 023408 (2011).

[40] T. F. Gallagher, *Rydberg Atoms*, 1st edn ed. (Cambridge Univ. Press, 1994).

[41] J. M. McGuirk, D. M. Harber, J. M. Obrecht, and E. A. Cornell, Phys. Rev. A **69**, 062905 (2004).

[42] D. A. Hite, Y. Colombe, A. C. Wilson, K. R. Brown, U. Warring, R. Jördens, J. D. Jost, K. S. McKay, D. P. Pappas, D. Leibfried, and D. J. Wineland, Phys. Rev. Lett. **109**, 103001 (2012).

[43] P. F. Weck, E. Kim, and G. W. Biedermann, RSC Adv. **5**, 38623 (2015).

[44] R. H. Miwa, T. M. Schmidt, W. L. Scopel, and A. Fazzio, Appl. Phys. Lett. **99**, 163108 (2011).

[45] T. C. Nguyen, M. Otani, and S. Okada, Phys. Rev. Lett. **106**, 106801 (2011).

[46] J. Yang and E. G. Wang, Phys. Rev. B **73**, 035406 (2006).

[47] N. H. de Leeuw, F. M. Higgins, and S. C. Parker, J. Phys. Chem. B **103**, 1270 (1999).

[48] *The Physics of SiO_2 and Its Interfaces*, edited by S. T. Pantelides (Pergamon, 1978).

[49] S. S. Nekrashevich and V. A. Gritsenko, Phys. Solid State **56**, 207 (2014).

[50] S. Ismail-Beigi and S. G. Louie, Phys. Rev. Lett. **95**, 156401 (2005).

[51] M. Mack, F. Karlewski, H. Hattermann, S. Höckh, F. Jessen, D. Cano, and J. Fortágh, Phys. Rev. A **83**, 052515 (2011).

[52] W. Li, I. Mourachko, M. W. Noel, and T. F. Gallagher, Phys. Rev. A **67**, 052502 (2003).

[53] J. Han, Y. Jamil, D. V. L. Norum, P. J. Tanner, and T. F. Gallagher, Phys. Rev. A **74**, 054502 (2006).

[54] M. Marinescu, H. R. Sadeghpour, and A. Dalgarno, Phys. Rev. A **49**, 982 (1994).

[55] A. Sanayei, N. Schopohl, J. Grimmel, M. Mack, F. Karlewski, and J. Fortágh, Phys. Rev. A **91**, 032509 (2015).

[56] F. Salvat, J. Fernndez-Varea, and W. Williamson Jr., Comput. Phys. Commun. **90**, 151 (1995).

[57] D. A. Steck, http://steck.us/alkalidata/rubidium87numbers.1.6.pdf (2003).

[58] I. I. Beterov, I. I. Ryabtsev, D. B. Tretyakov, and V. M. Entin, Phys. Rev. A **79**, 052504 (2009).

[59] I. I. Beterov, D. B. Tretyakov, I. I. Ryabtsev, A. Ekers, and N. N. Bezuglov, Phys. Rev. A **75**, 052720 (2007).

[60] J. Deiglmayr, M. Reetz-Lamour, T. Amthor, S. Westermann, A. de Oliveira, and M. Weidem Opt. Commun. **264**, 293 (2006).

[61] M. Saffman, T. G. Walker, and K. Mølmer, Rev. Mod. Phys. **82**, 2313 (2010).

[62] A. K. Mohapatra, T. R. Jackson, and C. S. Adams, Phys. Rev. Lett. **98**, 113003 (2007).

[63] G. Günter, H. Schempp, M. Robert-de Saint-Vincent, V. Gavryusev, S. Helmrich, C. S. Hofmann, S. Whitlock, and M. Weidemüller, Science **342**, 954 (2013).

[64] A. K. Mohapatra, M. G. Bason, B. Butscher, K. J. Weatherill, and C. S. Adams, Nat. Phys. **4**, 890 (2008).

[65] P. Kok and B. Lovett, *Introduction to Optical Quantum Information Processing* (Cambridge University Press, 2010).

[66] P. R. Berman and V. S. Malinovsky, *Principles of Laser Spectroscopy and Quantum Optics* (Princeton University Press, 2011).

[67] C. Cohen-Tannoudji, J. Dupont-Roc, and G. Grynberg, *Atom-Photon Interactions* (Wiley-VCH Verlag GmbH, 2008).

[68] M. G. Bason, A. K. Mohapatra, K. J. Weatherill, and C. S. Adams, J. Phys. B **42**, 075503 (2009).

[69] C. J. Foot, *Atomic Physics* (Oxford University Press, New York, 2005).

[70] J. E. Thomas and W. W. Quivers, Phys. Rev. A **22**, 2115 (1980).

[71] T. Swan-Wood, J. G. Coffer, and J. C. Camparo, IEEE Trans. Instrum. Meas. **50**, 1229 (2001).

[72] P. Böhi and P. Treutlein, Appl. Phys. Lett. **101**, 181107 (2012).

[73] A. Horsley, G. Du, and P. Treutlein, New J. Phys. **17**, 112002 (2015).

[74] C. Affolderbach, G. Du, T. Bandi, A. Horsley, P. Treutlein, and G. Mileti, IEEE Trans. Instrum. Meas. **64**, 3629 (2015).

[75] J. E. Bayfield and P. M. Koch, Phys. Rev. Lett. **33**, 258 (1974).

[76] J. G. Leopold and I. C. Percival, Phys. Rev. Lett. **41**, 944 (1978).

[77] R. G. Hulet and D. Kleppner, Phys. Rev. Lett. **51**, 1430 (1983).

[78] L. A. Bloomfield, R. C. Stoneman, and T. F. Gallagher, Phys. Rev. Lett. **57**, 2512 (1986).

[79] T. Udem, R. Holzwarth, and T. W. Hänsch, Nature **416**, 233 (2002).

[80] M. P. J., B. N. Taylor, and D. B. Newell, arXiv:1507.07956 (2015).

[81] J. J. McClelland, in *Atomic, Molecular, and Optical Physics: Atoms and Molecules*, *Experimental Methods in the Physical Sciences*, edited by F. Dunning and R. G. Hulet (Academic Press, 1996), p. 145.

[82] S. Chang and V. Minogin, Phys. Rep. **365**, 65 (2002).

[83] C. L. Holloway, J. A. Gordon, S. Jefferts, A. Schwarzkopf, D. A. Anderson, S. A. Miller, N. Thaicharoen, and G. Raithel, IEEE Trans. Antennas Propag. **62**, 6169 (2014).

[84] J. A. Gordon, C. L. Holloway, A. Schwarzkopf, D. A. Anderson, S. Miller, N. Thaicharoen, and G. Raithel, Appl. Phys. Lett. **105**, (2014).

[85] H. Fan, S. Kumar, J. Sheng, J. P. Shaffer, C. L. Holloway, and J. A. Gordon, Phys. Rev. Applied **4**, 044015 (2015).

[86] H. Q. Fan, S. Kumar, R. Daschner, H. Kübler, and J. P. Shaffer, Opt. Lett. **39**, 3030 (2014).

[87] D. A. Anderson, S. A. Miller, G. Raithel, J. A. Gordon, M. L. Butler, and C. L. Holloway, Phys. Rev. Applied **5**, 034003 (2016).

[88] G. Bjorklund, M. Levenson, W. Lenth, and C. Ortiz, Appl. Phys. B **32**, 145 (1983).

[89] D. W. Preston, Am. J. Phys **64**, 1432 (1996).

[90] A. Schwettmann, J. Sedlacek, and J. P. Shaffer, Rev. Sci. Instrum. **82**, 103103 (2011).

[91] S. C. Kumar, G. K. Samanta, K. Devi, and M. Ebrahim-Zadeh, Opt. Express **19**, 11152 (2011).

[92] G. Boyd and D. Kleinman, **39**, 3597 (1968)

[93] B. Saleh and M. Teich, *Fundamentals of Photonics*, 2nd ed. (Wiley New York, 1991).

[94] R. Boyd, *Nonlinear Optics*, 3rd ed. (Academic Press, 2008).

[95] W. Risk, T. Gosnell, and A. Nurmikko, *Compact Blue-Green Lasers* (Cambridge University Press, 2003).

[96] R. Driggers, *Encyclopedia of Optical Engineering* (CRC press, 2003), Vol. 3.

[97] A. A. Lagatsky, C. T. A. Brown, W. Sibbett, S. J. Holmgren, C. Canalias, V. Pasiskevicius, F. Laurell, and E. U. Rafailov, Opt. Express **15**, 1155 (2007).

[98] R. L. Targat, J.-J. Zondy, and P. Lemonde, Opt. Commun. **247**, 471 (2005).

[99] F. Villa, A. Chiummo, E. Giacobino, and A. Bramati, J. Opt. Soc. Am. B **24**, 576 (2007).

[100] F. Pignatiello, M. D. Rosa, P. Ferraro, S. Grilli, P. D. Natale, A. Arie, and S. D. Nicola, Opt. Commun. **277**, 14 (2007).

[101] G. Li, K. A. Winick, A. A. Said, M. Dugan, and P. Bado, Opt. Express **17**, 9442 (2009).

[102] K. Kato and E. Takaoka, Appl. Opt. **41**, 5040 (2002).

[103] S. Emanueli and A. Arie, Appl. Opt. **42**, 6661 (2003).

[104] F. Torabi-Goudarzi and E. Riis, Opt. Commun. **227**, 389 (2003).

[105] J. I. Thorpe, K. Numata, and J. Livas, Opt. Express **16**, 15980 (2008).

[106] A. Nevsky, S. Alighanbari, Q.-F. Chen, I. Ernsting, S. Vasilyev, S. Schiller, G. Barwood, P. Gill, N. Poli, and G. M. Tino, Opt. Lett. **38**, 4903 (2013).

[107] E. D. Black, Am. J. Phys **69**, 79 (2001).

[108] H. J. Metcalf and P. van der Straten, *Laser Cooling and Trapping* (Springer New York, 1999).

[109] C. C. Bradley and R. G. Hulet, in *Atomic, Molecular, and Optical Physics: Atoms and Molecules, Experimental Methods in the Physical Sciences*, edited by F. Dunning and R. G. Hulet (Academic Press, 1996), p. 129.

[110] W. Ketterle, Rev. Mod. Phys. **74**, 1131 (2002).

[111] J. Reichel, W. Hänsel, P. Hommelhoff, and T. Hänsch, Appl. Phys. B **72**, 81 (2014).

[112] D. A. Smith, S. Aigner, S. Hofferberth, M. Gring, M. Andersson, S. Wildermuth, P. Krüger, S. Schneider, T. Schumm, and J. Schmiedmayer, Opt. Express **19**, 8471 (2011).

[113] A. Tauschinsky, R. M. T. Thijssen, S. Whitlock, H. B. van Linden van den Heuvell, and R. J. C. Spreeuw, Phys. Rev. A **81**, 063411 (2010).

[114] J. Naber, S. Machluf, L. Torralbo-Campo, M. L. Soudijn, N. J. van Druten, H. B. van Linden van den Heuvell, and R. J. C. Spreeuw, J. Phys. B **49**, 094005 (2016).

[115] D. Barredo, H. Kübler, R. Daschner, R. Löw, and T. Pfau, Phys. Rev. Lett. **110**, 123002 (2013).

[116] J. Grimmel, M. Mack, F. Karlewski, F. Jessen, M. Reinschmidt, N. Sándor, and J. Fortágh, New J. Phys. **17**, 053005 (2015).

[117] L. W. Bruch, M. W. Cole, and E. Zaremba, *Physical Adsorption: Forces and Phenomena* (Oxford University Press, 1997).

[118] L. Béguin, A. Vernier, R. Chicireanu, T. Lahaye, and A. Browaeys, Phys. Rev. Lett. **110**, 263201 (2013).

[119] A. M. Hankin, Y.-Y. Jau, L. P. Parazzoli, C. W. Chou, D. J. Armstrong, A. J. Landahl, and G. W. Biedermann, Phys. Rev. A **89**, 033416 (2014).

[120] J. M. Obrecht, R. J. Wild, and E. A. Cornell, Phys. Rev. A **75**, 062903 (2007).

[121] J. D. Carter and J. D. D. Martin, Phys. Rev. A **88**, 043429 (2013).

[122] A. Safavi-Naini, P. Rabl, P. F. Weck, and H. R. Sadeghpour, Phys. Rev. A **84**, 023412 (2011).

[123] A. Safavi-Naini, E. Kim, P. F. Weck, P. Rabl, and H. R. Sadeghpour, Phys. Rev. A **87**, 023421 (2013).

[124] G. Kresse and J. Furthmüller, Phys. Rev. B **54**, 11169 (1996).

[125] G.-M. Rignanese, A. De Vita, J.-C. Charlier, X. Gonze, and R. Car, Phys. Rev. B **61**, 13250 (2000).

[126] J. A. Sedlacek, E. Kim, S. T. Rittenhouse, P. F. Weck, H. R. Sadeghpour, and J. P. Shaffer, Phys. Rev. Lett. **116**, 133201 (2016).

[127] K. Christmann, *Introduction to Surface Physical Chemistry* (Springer-Verlag New York, 1991).

[128] W. Mönch, *Semiconductor surfaces and interfaces*, third edition ed. (Springer Science & Business Media, 2013), Vol. 26.

[129] *CRC Handbook of Chemistry and Physics, 96th Edition*, edited by W. M. Haynes (CRC Press/Taylor and Francis, Internet Version 2016).

[130] *Thin-Film Diamond II*, Vol. 77 of *Semiconductors and Semimetals*, edited by C. E. Nebel and J. Ristein (Elsevier, 2004).

[131] J. Mitroy, M. S. Safronova, and C. W. Clark, J. Phys. B **43**, 202001 (2010).

[132] H. Ibach, *Physics of Surfaces and Interfaces* (Springer Berlin Heidelberg, 2006).

[133] J. de Boer, *The Dynamical Character of Adsorption*, 2 ed. ed. (Oxford: Clarendon, 1968).

[134] M. P. Robinson, B. L. Tolra, M. W. Noel, T. F. Gallagher, and P. Pillet, Phys. Rev. Lett. **85**, 4466 (2000).

[135] W. Li, M. Noel, M. Robinson, P. Tanner, T. Gallagher, D. Comparat, B. Laburthe Tolra, N. Vanhaecke, T. Vogt, N. Zahzam, P. Pillet, and D. Tate, Phys. Rev. A **70**, 042713 (2004).

[136] M. Robert-de Saint-Vincent, C. S. Hofmann, H. Schempp, G. Günter, S. Whitlock, and M. Weidemüller, Phys. Rev. Lett. **110**, 045004 (2013).

[137] X. Lu, Y. Sun, and H. Metcalf, Phys. Rev. A **84**, 033402 (2011).

[138] M. Bouchiat, J. Guéna, P. Jacquier, M. Lintz, and A. Papoyan, Appl. Phys. B **68**, 1109 (1999).

[139] M. Stephens, R. Rhodes, and C. Wieman, J. Appl. Phys. **76**, 3479 (1994).

[140] S. Gozzini, G. Nienhuis, E. Mariotti, G. Paffuti, C. Gabbanini, and L. Moi, Opt. Commun. **88**, 341 (1992).

[141] D. A. King, Surface Science **64**, 43 - 51 (1977).

[142] L. J. Brillson, *Surfaces and Interfaces of Electronic Materials* (John Wiley & Sons, 2010), Vol. 7.

[143] F. Rouquerol, J. Rouquerol, and K. Sing, *Adsorption by Powders and Porous Solids* (Academic Press, 1999).

[144] M. W. Cole, Rev. Mod. Phys. **46**, 451 (1974).

[145] C. Grimes, Surf. Sci. **73**, 379 (1978).

[146] E. Andrei, *Two-dimensional Electron Systems: On Helium and Other Cryogenic Substrates* (Springer Science & Business Media, 2012), Vol. 19.

[147] R. S. Crandall and R. Williams, Phys. Rev. A **5**, 2183 (1972).

[148] C. C. Grimes and T. R. Brown, Phys. Rev. Lett. **32**, 280 (1974).

[149] C. C. Grimes, T. R. Brown, M. L. Burns, and C. L. Zipfel, Phys. Rev. B **13**, 140 (1976).

[150] E. Chulkov, V. Silkin, and P. Echenique, Surf. Sci. **391**, L1217 (1997).

[151] A. M. Goodman and J. J. O'Neill, J. Appl. Phys. **37**, 3580 (1966).

[152] S. D. Brorson, D. J. DiMaria, M. V. Fischetti, F. L. Pesavento, P. M. Solomon, and D. W. Dong, J. Appl. Phys. **58**, 1302-1313 (1985).

[153] V. I. Polyakov, N. M. Rossukanyi, A. I. Rukovishnikov, S. M. Pimenov, A. V. Karabutov, and V. I. Konov, J. Appl. Phys **84**, 2882 (1998).

[154] K. P. Loh, J. S. Foord, R. G. Egdell, and R. B. Jackman, Diamond Relat. Mater. **6**, 874 (1997).

[155] M. Eyckeler, W. Monch, T. Kampen, R. Dimitrov, O. Ambacher, and M. Stutzmann, J. Vac. Sci. Technol. B **16**, 2224 (1998).

[156] C. Wu and A. Kahn, Appl. Surf. Sci. **162-163**, 250 (2000).

[157] K. P. Loh, M. Nishitani-Gamo, I. Sakaguchi, T. Taniguchi, and T. Ando, Appl. Phys. Lett. **72**, 3023 (1998).

[158] *Springer Handbook of Electronic and Photonic Materials*, edited by S. Kasap and P. Capper (Springer US, 2007).

[159] A. M. Bonch-Bruevich, T. A. Vartanyan, A. V. Gorlanov, Y. N. Maksimov, S. G. Przhibelskiĭ, and V. V. Khromov, Zh. Eksp. Teor. Fiz **97**, 1077 (1990).

[160] Y. Shapira, S. Cox, and D. Lichtman, Surf. Sci. **50**, 503 (1975).

[161] W. T. Sommer and D. J. Tanner, Phys. Rev. Lett. **27**, 1345 (1971).

[162] R. Mehrotra and A. J. Dahm, Journal of Low Temperature Physics **67**, 115 (1987).

[163] H. Failache, S. Saltiel, A. Fischer, D. Bloch, and M. Ducloy, Phys. Rev. Lett. **88**, 243603 (2002).

[164] H. J. Falge and A. Otto, Phys. Status Solidi (b) **56**, 523 (1973).

[165] Y. Chao, J. Sheng, J. A. Sedlacek, and J. P. Shaffer, Phys. Rev. B **93**, 045419 (2016).

[166] Y. Jiao, Z. Yang, J. Li, G. Raithel, J. Zhao, and S. Jia, arXiv:1601.01748 (2016).

[167] S. A. Miller, D. A. Anderson, and G. Raithel, arXiv:1601.06840 (2016).

[168] M. Auzinsh, D. Budker, and S. M. Rochester, *Optically Polarized Atoms* (Oxford University Press, New York, 2010).

[169] B. H. Bransden and C. J. Joachain, *Physics of Atoms and Molecules, Second Edition* (Prentice Hall, 2003).

[170] J. Hare, M. Gross, and P. Goy, Phys. Rev. Lett. **61**, 1938 (1988).

[171] M. Weisbluth, *Atoms and Molecules* (Academic, New York, 1978).

[172] R. N. Zare, *Angular Momentum: Understanding Spatial Aspects in Chemistry and Physics* (John Wiley & Sons, 1989).

Appendix A

Rydberg Atoms in External Fields

The preceding chapters show results of spectroscopy of Rydberg atoms in external dc electric and magnetic fields. The effects are theoretically analyzed by constructing the full Hamiltonian and rediagonalizing it, which is equivalent to solving the time independent Schrödinger equation. The full Hamiltonian is,

$$H = H_{\text{atom}} + H_{\text{atom-field}}, \tag{A.1}$$

where $H_{\text{atom-field}}$ is the Hamiltonian due to the interaction between the atom and an external field. In this section, the external field will be either a magnetic field, an electric field, or both. H_{atom} is the bare atom Hamiltonian consisting of the energies of the states along the diagonal,

$$H_{\text{atom}} = \begin{pmatrix} E_1 & & & & \\ & E_2 & & 0 & \\ & & E_3 & & \\ & 0 & & \ddots & \\ & & & & E_j \end{pmatrix}. \tag{A.2}$$

In matrix form the Hamiltonian due to external fields is,

$$H_{\text{atom-field}} = \begin{pmatrix} \langle\psi_1|H_{\text{atom-field}}|\psi_1\rangle & \cdots & \langle\psi_1|H_{\text{atom-field}}|\psi_j\rangle \\ \vdots & \ddots & \vdots \\ \langle\psi_i|H_{\text{atom-field}}|\psi_1\rangle & \cdots & \langle\psi_i|H_{\text{atom-field}}|\psi_j\rangle \end{pmatrix}. \tag{A.3}$$

The details of calculating the matrix elements for $H_{\text{atom-field}}$ for different cases are given in the following sections.

A.1 Rydberg Atoms in a Magnetic Field

A.1.1 Hamiltonian and Basis

The interaction between a magnetic field, $\vec{B}$, and an atom is described by the magnetic dipole Hamiltonian,

$$H_B = -\vec{\mu} \cdot \vec{B}, \tag{A.4}$$

with the magnetic moment $\vec{\mu} = -\mu_B g_L \vec{L} - \mu_B g_S \vec{S}$. Rb is an atom with a single valence electron, so the g-factors are $g_L = 1$ and $g_L \simeq 2$ [168]. There is also a diamagnetic Hamiltonian, H_D, in addition to H_B . However its effect is small and it is neglected. The relative magnitude of the diamagnetic term to the dipole term is [169],

$$\frac{H_D}{H_B} \approx \frac{n^4}{Z^2} B\, 10^6, \tag{A.5}$$

where Ze is the nuclear charge and B is the magnetic field in T. For Rb with $Z = 37$, $n = 100$ and $B = 100\,\mathrm{G}$ the relative magnitude is $\sim 10^{-3}$.

The Zeeman shift is a valid approximation when the interaction with a magnetic field is much smaller in energy that the splitting between states. In the case of magnetically trapping the ground state of ^{87}Rb with magnetic fields ($< 30\,\mathrm{G}$), the approximation holds. For Rydberg atoms, this is not always the case, as the fine structure splitting scales $\sim n^{-3}$. At high n the fine structure splitting can be small. The calculations involving Rydberg atoms are done in

the $|Jm_J\rangle$ basis. In this basis H_B becomes (with $\vec{L} = \vec{J} - \vec{S}$),

$$H_B = \mu_B(\vec{J} + \vec{S}) \cdot \vec{B}. \tag{A.6}$$

A.1.2 Matrix Elements

The matrix elements of H_B are

$$\begin{aligned} H_{B_{ij}} =& \mu_B B \sum_{q=-1}^{+1} A_q \left(\langle nLSJm_J|J|n'L'S'J'm'_J\rangle + \langle nLSJm_J|S|n'L'S'J'm'_J\rangle\right) \\ & \times \langle nL|n'L'\rangle, \end{aligned} \tag{A.7}$$

where $\langle nL|n'L'\rangle$ is an integral using the radial part of the wavefunction for state n and L. Since the radial wavefunctions are orthogonal,

$$\langle nL|n'L'\rangle = \delta_{nn'}\delta_{LL'}, \tag{A.8}$$

where δ_{ij} is the Kronecker delta. The values of A_q depend on the angle α between $\vec{B}$ and the quantization axis along $\vec{z}$, as shown in Fig. A.1. $\vec{B}$ is decomposed into $\vec{x}$ and $\vec{z}$ components following Table 3.2,

$$\begin{aligned} A_{-1} &= \frac{1}{\sqrt{2}} \sin\alpha \\ A_0 &= \cos\alpha \\ A_{+1} &= -\frac{1}{\sqrt{2}} \sin\alpha. \end{aligned} \tag{A.9}$$

Typically the quantization axis is chosen along $\vec{B}$, however this is not always the case, in particular when $\vec{E}$ and $\vec{B}$ are both present and pointing in different directions [170].

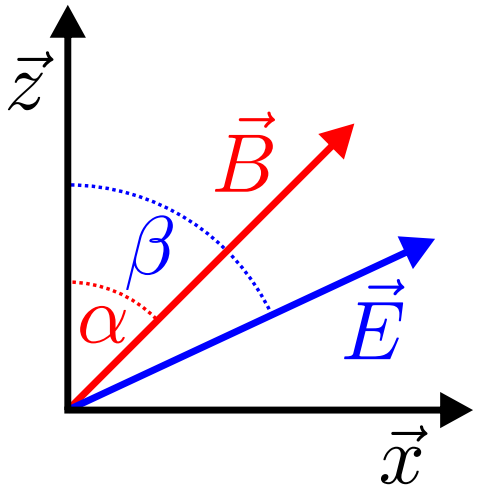

Figure A.1: Angle α of the magnetic field $\vec{B}$ with respect to the quantization axis $\vec{z}$.

The values for $\langle J\rangle$ and $\langle S\rangle$ can be evaluated using the Wigner-Eckart theorem [171]. Using the Wigner-Eckart theorem, $\langle J\rangle$ is,

$$\langle nLSJm_J|J|n'L'S'J'm'_J\rangle = (-1)^{J-m_J}\begin{pmatrix} J & 1 & J' \\ -m_J & q & m'_J \end{pmatrix}\langle nLSJ||J||n'L'S'J'\rangle, \tag{A.10}$$

with the reduced matrix element $\langle||J||\rangle$ [171],

$$\langle nLSJ||J||n'L'S'J'\rangle = \delta_{JJ'}\sqrt{J(2J+1)(J'+1)}. \tag{A.11}$$

A similar process can be followed to evaluate $\langle S\rangle$,

$$\langle nLSJm_J|S|n'L'S'J'm'_J\rangle = (-1)^{J-m_J}\begin{pmatrix} J & 1 & J' \\ -m_J & q & m'_J \end{pmatrix}\langle nLSJ||S||n'L'S'J'\rangle, \tag{A.12}$$

Table A.1: List of selection rules for magnetic dipole (M1) transitions in two different bases.

	$\|Jm_J\rangle$	$\|Fm_F\rangle$
Δn	0	0
ΔL	0	0
ΔS	0	0
ΔJ	$\pm 1, 0 (0 \nleftrightarrow 0)$	$\pm 1, 0 (0 \nleftrightarrow 0)$
Δm_J	$\pm 1, 0 (0 \nleftrightarrow 0$ if $\Delta J = 0)$	-
ΔF	-	$\pm 1, 0 (0 \nleftrightarrow 0)$
Δm_F	-	$\pm 1, 0 (0 \nleftrightarrow 0$ if $\Delta F = 0)$

with,

$$\begin{aligned}\langle nLSJ||S||n'L'S'J'\rangle =&(-1)^{L+S'+J+1}\delta_{LL'}\sqrt{(2J+1)(2J'+1)} \\ &\times \begin{Bmatrix} J & 1 & J' \\ S' & L & S \end{Bmatrix} \langle nS||S||n'S'\rangle,\end{aligned} \tag{A.13}$$

and,

$$\langle nS||S||n'S'\rangle = \sqrt{(2S+1)(S+1)S}\delta_{SS'}. \tag{A.14}$$

After combining equations the Hamiltonian becomes

$$\begin{aligned}H_B =&\mu_B B \sum_{q=-1}^{+1} A_q (-1)^{J-m_J}\sqrt{(2J+1)}\delta_{nn'}\delta_{LL'} \begin{pmatrix} J & 1 & J' \\ -m_J & q & m'_J \end{pmatrix} \Big[\sqrt{J(J+1)}\delta_{JJ'} \\ &+(-1)^{L+S'+J+1}\sqrt{S(2S+1)(S+1)(2J'+1)}\delta_{SS'} \begin{Bmatrix} J & 1 & J' \\ S' & L & S \end{Bmatrix}\Big].\end{aligned} \tag{A.15}$$

The Kronecker deltas represent selection rules and only allow coupling between certain states. Other selection rules arise when evaluating the $3j$ and $6j$ symbols, a complete list is compiled in Table A.1. By analyzing selection rules, it can be seen that only states with the same n and L will couple to each other and

produce nonzero values. For D states with $S = 1/2$, 10 states are needed to construct H_B. With $\alpha = 0$, H_B in units of MHz with B in units of G is,

$$H_B = \begin{pmatrix} -1.68B & 0 & 0 & 0 & 0 & -0.56B & 0 & 0 & 0 & 0 \\ 0 & -0.56B & 0 & 0 & 0 & 0 & -0.69B & 0 & 0 & 0 \\ 0 & 0 & 0.56B & 0 & 0 & 0 & 0 & -0.69B & 0 & 0 \\ 0 & 0 & 0 & 1.68B & 0 & 0 & 0 & 0 & -0.56B & 0 \\ 0 & 0 & 0 & 0 & -4.20B & 0 & 0 & 0 & 0 & 0 \\ -0.56B & 0 & 0 & 0 & 0 & -2.52B & 0 & 0 & 0 & 0 \\ 0 & -0.69B & 0 & 0 & 0 & 0 & -0.84B & 0 & 0 & 0 \\ 0 & 0 & -0.69B & 0 & 0 & 0 & 0 & 0.84B & 0 & 0 \\ 0 & 0 & 0 & -0.56B & 0 & 0 & 0 & 0 & 2.52B & 0 \\ 0 & 0 & 0 & 0 & 0 & 0 & 0 & 0 & 0 & 4.20B \end{pmatrix} \begin{matrix} \left.\vphantom{\begin{matrix}a\\a\\a\\a\end{matrix}}\right\} J = \frac{3}{2} \\ \left.\vphantom{\begin{matrix}a\\a\\a\\a\\a\\a\end{matrix}}\right\} J = \frac{5}{2} \end{matrix}$$

$$m_J = \begin{matrix} \frac{-3}{2} & \frac{-1}{2} & \frac{1}{2} & \frac{3}{2} & \frac{-5}{2} & \frac{-3}{2} & \frac{-1}{2} & \frac{1}{2} & \frac{3}{2} & \frac{5}{2} \end{matrix} \tag{A.16}$$

Most of the elements are zero as a result of the selection rules. The energies along the diagonal are equal to the Zeeman shift for low fields,

$$\begin{aligned} \Delta E &= g_J \mu_B B m_J \\ g_J &= \frac{3}{2} + \frac{S(S+1) - L(L+1)}{2J(J+1)}. \end{aligned} \tag{A.17}$$

Following a similar process, calculations can be carried out in the $|F, m_F\rangle$ basis,

$$\begin{aligned} H_B =& \mu_B B \sum_{q=-1}^{+1} A_q (-1)^{F-m_F+I+J+F'+1} \delta_{nn'} \delta_{LL'} \delta_{II'} \sqrt{(2F+1)(2F'+1)(2J+1)} \\ & \begin{pmatrix} F & 1 & F' \\ -m_F & q & m'_F \end{pmatrix} \begin{Bmatrix} F & 1 & F' \\ J' & I & J \end{Bmatrix} \Bigg[\delta_{JJ'} \sqrt{J(J+1)} + \\ & (-1)^{L+S+J+1} \delta_{SS'} \sqrt{S(2S+1)(S+1)(2J'+1)} \begin{Bmatrix} J & 1 & J' \\ S' & L & S \end{Bmatrix} \Bigg]. \end{aligned} \tag{A.18}$$

Using this Hamiltonian the shifts of $5S$ and $5P$ states can be calculated. Ex-

pressions are equivalent to the Breit-Rabi formulas in [57], but are not restricted to $J = 1/2$ states. A list of selection rules also apply to this basis and are listed in Table A.1.

A.1.3 Results

After constructing the bare atom Hamiltonian with quantum defects, the energy shifts can be calculated. Results are shown in Fig. A.2 for the $41D$ and $81D$ states with $\alpha = 0$, so a comparison can be made with the first order Zeeman shift. H_B is same for both states, however the fine structure splitting is not the same which accounts for the difference in calculated energies. For the $41D$ states Eq. A.17 is a good approximation until $\sim 50\,\mathrm{G}$. At higher n, the fine structure splitting is smaller, so the approximation of Eq. A.17 breaks down at a smaller magnetic field. For the $81D$ states this happens at $\sim 20\,\mathrm{G}$.

To compare to calculations, the energy level shift between Rydberg states is measured using Rydberg atom EIT. A solenoid around a vapor cell is used to create a uniform B field. The B field splits the fine structure states into its different m_J components. The frequency difference between the $|5/2\ 5/2\rangle$ and $|5/2\ 1/2\rangle$ states is measured. There are many more states, however most are not observed as a result of selection rules due to the relative orientation of the magnetic field to laser polarizations. These two states are the strongest. Experimental results for the $81D$ states are shown in Fig. A.3.

At high magnetic fields when the energy shifts are large compared to the fine

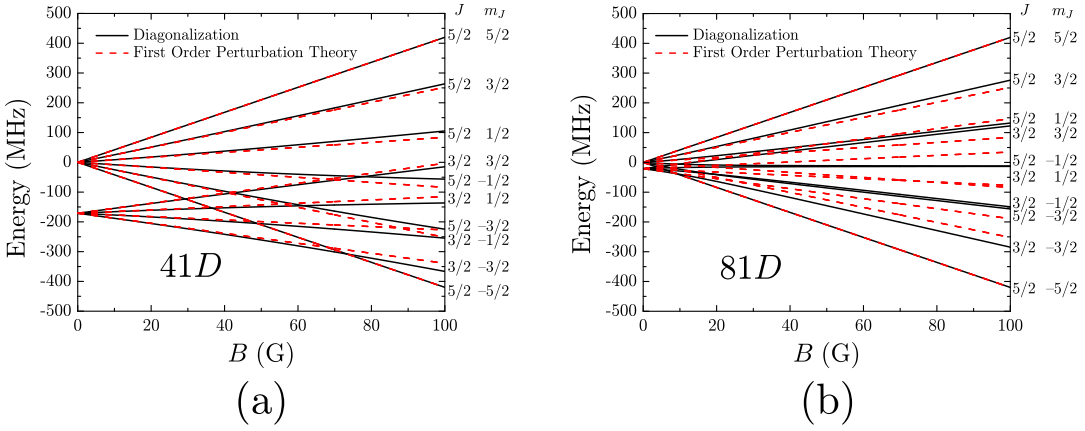

Figure A.2: Energy shift of the $41D$ (a) and $81D$ states (b). The states are labeled by $|Jm_J\rangle$ which are only good quantum numbers for small energy shifts. The dashed red lines are calculated using Eq. A.17.

structure splitting, J and m_J are no longer good quantum numbers. The shift can be approximated by [169],

$$\Delta E = \mu B(m_L + 2m_S). \tag{A.19}$$

A comparison between this approximation and the matrix diagonalization for the $81D$ state is shown in Fig. A.4.

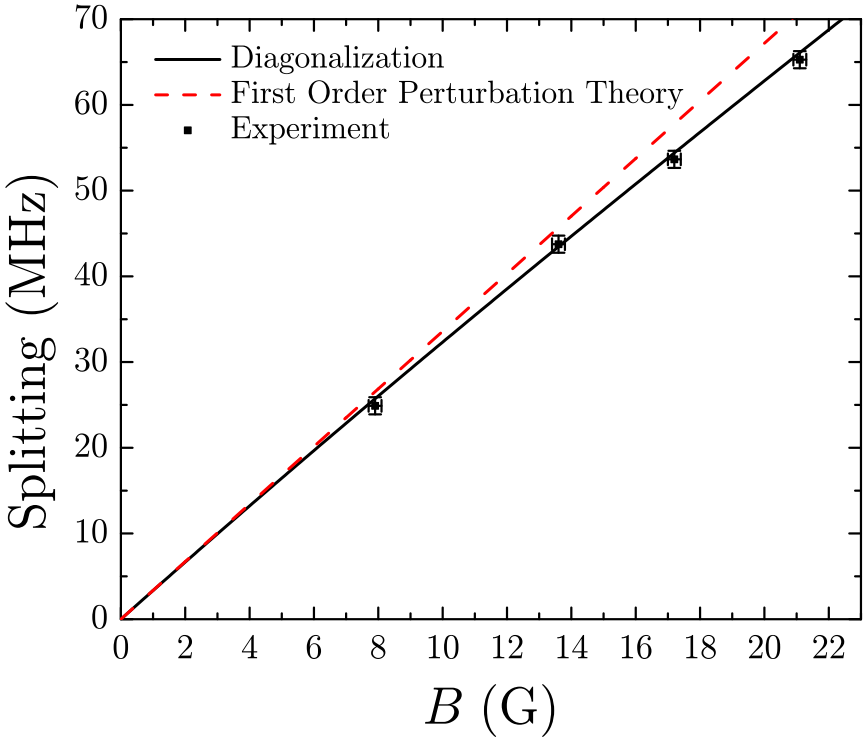

Figure A.3: Theory and experimental measurement of the energy difference between the $|5/2\ 5/2\rangle$ and $|5/2\ 1/2\rangle$ states in the $81D$ manifold.

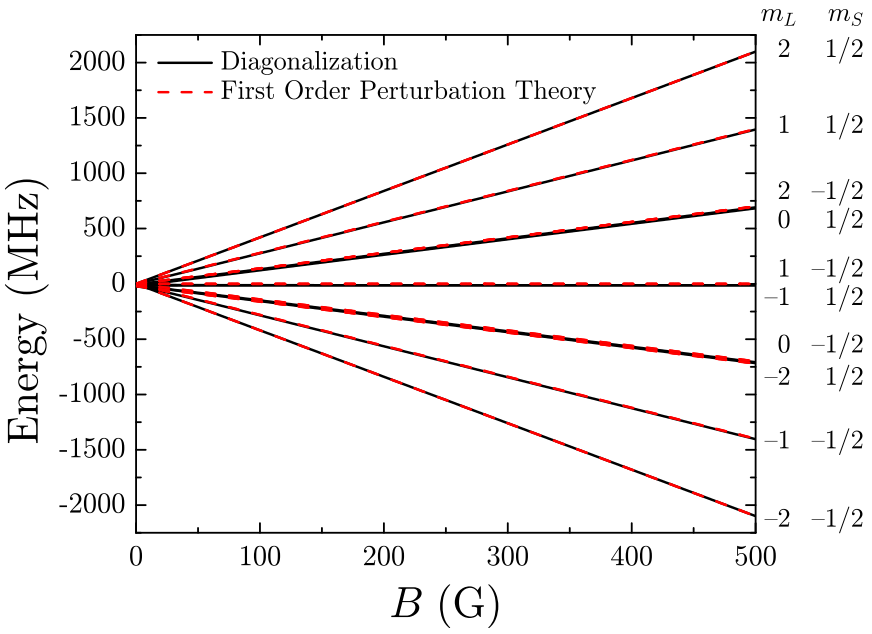

Figure A.4: Plot of the energy levels of the $81D$ state in the Paschen-Back regime.

A.2 Rydberg Atoms in an Electric Field

A.2.1 Hamiltonian and Basis

The interaction between an electric field $\vec{E}$ and an atom is described by the electric dipole Hamiltonian,

$$H_E = -\vec{\mu} \cdot \vec{E}, \tag{A.20}$$

where $\vec{\mu} = e\vec{r}$ is the electric dipole moment. From second order perturbation theory the Stark shift is

$$\Delta E = -\frac{1}{2}\alpha E^2, \tag{A.21}$$

where α is the polarizability. The approximation holds when the energy shifts are small. As shown in Fig. 1.1b the polarizability of the ground state of $5S_{1/2}$

of Rb is $\sim 10^9$ times smaller than the polarizability of the $60S_{1/2}$ state. Since the polarizability of Rydberg states are orders of magnitude higher that of the ground state, second order perturbation theory breaks down at a much smaller electric field. Similarly to the B field calculations, the Stark shift calculations are carried out in the $|Jm_J\rangle$ basis.

A.2.2 Matrix Elements

The matrix elements of H_E are

$$H_{E_{ij}} = E\mu_{ij}. \tag{A.22}$$

The transition dipole moments can be separated into angular and radial parts, $\mu_{ij} = \mu_{r_{ij}} \times \mu_{a_{ij}}$. The radial part only depends on the radial wave functions,

$$\mu_{r_{ij}} = \int_0^\infty R_{n,L}(r) r R_{n'L'}(r) r^2 dr. \tag{A.23}$$

The angular part of the transition dipole moment is,

$$\mu_{a_{ij}} = \sum_{q=-1}^{+1} A_q \langle nLJm_J|\epsilon_q|n'L'J'm'_J\rangle \tag{A.24}$$

The values of A_q depend on the relative angle β between $\vec{E}$ and the quantization axis along $\vec{z}$ as shown in Fig. A.1. $\vec{E}$ is decomposed into $\vec{x}$ and $\vec{z}$ components following Table 3.2,

$$\begin{aligned} A_{-1} &= \frac{1}{\sqrt{2}} \sin\beta \\ A_0 &= \cos\beta \\ A_{+1} &= -\frac{1}{\sqrt{2}} \sin\beta. \end{aligned} \tag{A.25}$$

Similarly to the matrix elements for the magnetic dipole Hamiltonian, the values for $\langle \epsilon_q \rangle$ can be evaluated using the Wigner-Eckart theorem,

$$\langle nLSJm_J|\epsilon_q|n'L'S'J'm'_J\rangle = (-1)^{J-m_J} \begin{pmatrix} J & 1 & J' \\ -m_J & q & m'_J \end{pmatrix} \langle nLSJ||\epsilon||n'L'S'J'\rangle, \tag{A.26}$$

and,

$$\begin{aligned} \langle nLSJ||\epsilon||n'L'S'J'\rangle =& (-1)^{L+S+J'+1}\delta_{SS'}\sqrt{(2J+1)(2J'+1)} \\ & \times \begin{Bmatrix} J & 1 & J' \\ L' & S & L \end{Bmatrix} \langle nL||\epsilon||n'L'\rangle, \end{aligned} \tag{A.27}$$

and [172],

$$\langle nL||\epsilon||n'L'\rangle = (-1)^L \sqrt{(2L+1)(2L'+1)} \begin{pmatrix} L & 1 & L' \\ 0 & 0 & 0 \end{pmatrix}. \tag{A.28}$$

Combining terms the $\mu_{a_{ij}}$ becomes,

$$\begin{aligned} \mu_{a_{ij}} = & \sum_{q=-1}^{+1} A_q (-1)^{J+J'+S+1-m_J} \delta_{SS'} \sqrt{(2J+1)(2J'+1)(2L+1)(2L'+1)} \\ & \times \begin{pmatrix} J & 1 & J' \\ -m_J & q & m'_J \end{pmatrix} \begin{Bmatrix} J & 1 & J' \\ L' & S & L \end{Bmatrix} \begin{pmatrix} L & 1 & L' \\ 0 & 0 & 0 \end{pmatrix}. \end{aligned} \tag{A.29}$$

Following a similar process calculations can be carried out in the $|Fm_F\rangle$. The difference is in the angular matrix elements,

$$\begin{aligned} \mu_{a_{ij}} = & \sum_{q=-1}^{+1} A_q (-1)^{F+F'+J+J'+I+S-m_F} \delta_{II'} \delta_{SS'} \\ & \times \sqrt{(2F+1)(2F'+1)(2J+1)(2J'+1)(2L+1)(2L'+1)} \\ & \times \begin{pmatrix} F & 1 & F' \\ -m_F & q & m'_F \end{pmatrix} \begin{Bmatrix} F & 1 & F' \\ J' & I & J \end{Bmatrix} \begin{Bmatrix} J & 1 & J' \\ L' & S & L \end{Bmatrix} \begin{pmatrix} L & 1 & L' \\ 0 & 0 & 0 \end{pmatrix}. \end{aligned} \tag{A.30}$$

The transition dipole moments used in Chapter 3 are calculated using Eq. A.23 and A.30.

Table A.2: List of selection rules for electric dipole (E1) transitions in two different bases.

	$\|Jm_J\rangle$	$\|Fm_F\rangle$
ΔL	± 1	± 1
ΔJ	$\pm 1, 0 (0 \nleftrightarrow 0)$	$\pm 1, 0 (0 \nleftrightarrow 0)$
Δm_J	$\pm 1, 0 (0 \nleftrightarrow 0$ if $\Delta J = 0)$	-
ΔF	-	$\pm 1, 0 (0 \nleftrightarrow 0)$
Δm_F	-	$\pm 1, 0 (0 \nleftrightarrow 0$ if $\Delta F = 0)$

A.2.3 Results

There is a separate set of selection rules for electric dipole transitions listed in Table A.2. There is no restriction on Δn, so many nearby states need to be included in the calculation. For example when calculating the Stark shift for a nS or nD state, states from $n \pm 4$, $(L = 0 - 3)$ and $n - 4$ to n $(L = 4 - 13)$ are used. All states with $|m_J| \leq 9/2$ are included in the calculation, resulting in 1278 states. The matrix is too large for Mathematica to diagonalize algebraically, so the calculation is done numerically for each value of the electric field. The results of the calculation for the $81D_{5/2}$ state is shown in Fig. A.5. Only three curves are shown because the $\pm m_J$ states are degenerate. At low electric field the curves can be fit to Eq. A.21 to obtain a polarizability. As the electric field increases mixing from nearby states becomes large and the shifts no longer obey Eq. A.21.

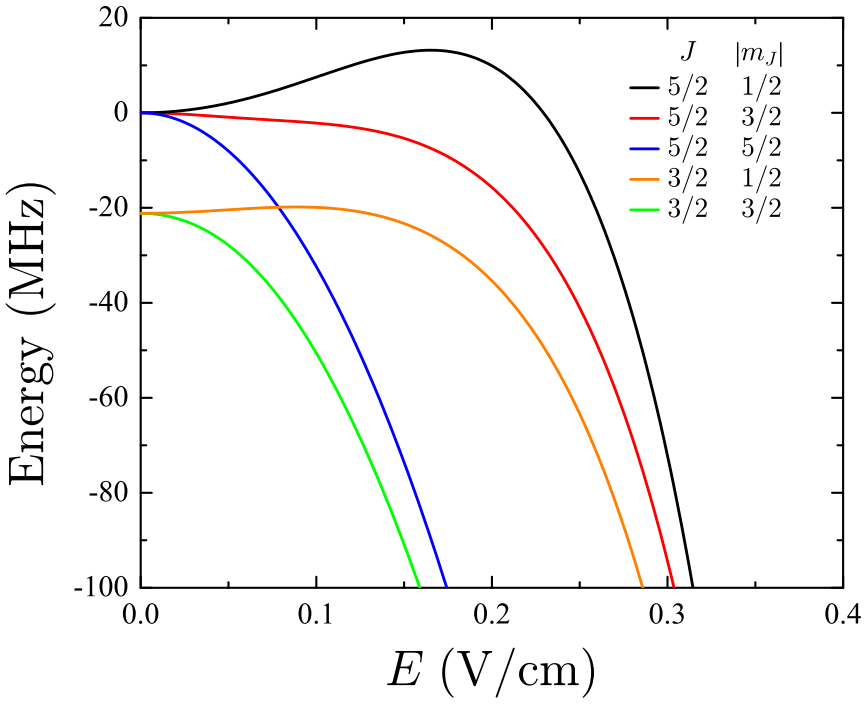

Figure A.5: Stark shift calculation for $81D$ with $\vec{E} \parallel \vec{z}$ ($\beta = 0$).

A.3 Magnetic and Electric Fields

In Chapters 5 and 6 experiments are carried out in both $\vec{B}$ and $\vec{E}$ fields. In this case $H_{\text{atom-field}} = H_B + H_E$ and H is diagonalized. In the calculations, B is considered to be aligned along the $\vec{z}$ axis with $\alpha = 0$. Changing β, the angle of $\vec{E}$ dramatically changes the energy levels of the Rydberg states. As an example, Fig. A.6 shows the results of calculations of the $81D$ state with $B = 14.3\,\text{G}$ with $\vec{E} \parallel \vec{B}$ in Fig. A.6(a) and $\vec{E} \perp \vec{B}$ in Fig. A.6(b). The states are labeled in terms of magnetic quantum number. The presence of the magnetic field breaks the degeneracy of m_J.

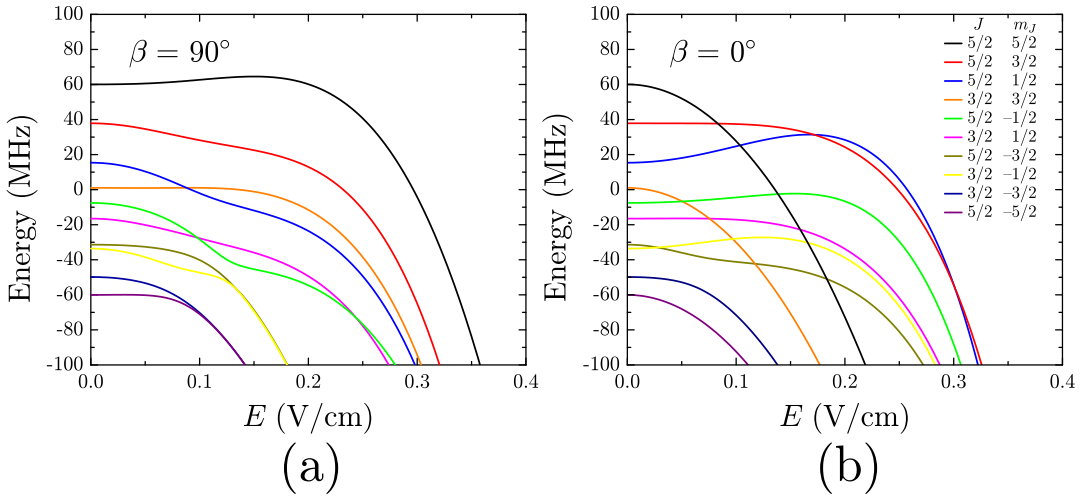

Figure A.6: Calculation of the shift of $81D$ states for two different cases with $B = 14.3\,\mathrm{G}$. (a) $\vec{E}$ and $\vec{B}$ are perpendicular. (b) $\vec{E}$ and $\vec{B}$ are parallel.

Appendix B

Alignment of the Bow-tie cavity

The following is the procedure used for the alignment of the bow-tie cavity. The procedure follows the nomenclature and orientation of the cavity in Fig. 4.19a.

B.1 Alignment Procedure

1. The center the mirrors should be at the same height as each other as well as at the height of the crystal. Place the mirrors roughly in the calculated positions for the desired cavity.

2. Align the input beam so that it is centered on M_1 and M_2

3. Remove M_1 and adjust M_2 so that the beam is centered on M_3.

4. Adjust M_3 to get the maximum single pass blue power by measuring the blue light passing through M_4. If the beam is clipping or off center while passing through the crystal, steps 2-4 should be repeated as many times as necessary. The single pass efficiency should be around 1% for input powers of $800\,\mathrm{mW} - 1\,\mathrm{W}$. If the single pass efficiency is low then the output of the bow-tie cavity will be low. If the alignment looks good, but the blue power is low, then lens L_1 may need to be moved, or the temperature of the crystal adjusted.

5. After the single pass efficiency is maximized, put M_1 back in place. This will change the pointing of the input beam slightly, so make small adjustments to M_2 and M_3 to again maximize the single pass power. Now that the single

pass is peaked up, mirrors M_2 or M_3 should not be adjusted for the rest of the procedure. The rest of the alignment will be done by adjusting M_1 and M_4.

6. The idea is to overlap the circulating beam with the input beam that is aligned correctly and has a high conversion efficiency. A small amount of blue light will be reflected by M_4. Make sure this is passing through M_1. Using an IR card, adjust M_4 so that blue spot is overlapped with the reflected beam close to M_1. Then adjust M_1 so that the blue spot and reflected IR beam are overlapped far away from M_1. Perform several iterations of adjusting M_4 and M_1, soon the beams will start to overlap and the cavity will start to flicker. The cavity is resonant with many TEM modes, and when the cavity is flickering it is switching between being resonant with many spatial modes. The air currents in the room cause the optical path length inside the cavity to change, thus changing the resonant frequency of the cavity and the TEM mode supported.

7. Put a box around the cavity to shield it from most of the air currents. Look at the blue output modes of the cavity on an index card. Iteratively adjust M_4 and M_1 to minimize the spatial extent of the modes. After this is done, the brightest mode should be the desired TEM_{00} mode.

8. Put the cover on. While measuring the blue power after M_4 and scanning across the TEM_{00} mode with the piezo, make fine adjustments to the input mirrors to maximize the output power.

Appendix C

Publications and Presentations

C.1 List of Publications

Below is a list of peer-reviewed publications in which I was either author or co-author. The list is in reverse chronological order.

9. J. A. Sedlacek, E. Kim, S. T. Rittenhouse, P. F. Weck, H. R. Sadeghpour and J. P. Shaffer, "Electric field cancellation on quartz: a Rb adsorbate induced negative electron affinity surface," Phys. Rev. Lett. **116**, 133201 (2016).

8. S. Kumar, J. Sheng, J. A. Sedlacek, H. Fan, and J. P. Shaffer, "Collective state synthesis in an optical cavity using Rydberg atom dipole blockade," J. Phys. B: At. Mol. Opt. Phys. **49**, 064014 (2016).

7. Y. Chao, J. Sheng, J. A. Sedlacek, and J. P. Shaffer, "Surface phonon polaritons on anisotropic piezoelectric superlattices," Phys. Rev. B **93**, 045419 (2016).

6. H. Fan, S. Kumar, J. Sedlacek, H. Kübler, S. Karimkashi, and J. P. Shaffer, "Atom based RF electric field sensing," J. Phys. B: At. Mol. Opt. Phys. **48**, 202001 (2015).

5. H. Kübler, D. Booth, J. Sedlacek, P. Zabawa, and J. P. Shaffer, "Exploiting the coupling between a Rydberg atom and a surface phonon polariton for single-photon subtraction ," Phys. Rev. A **88**, 043810 (2013).

4. J. A. Sedlacek, A. Schwettmann, H. Kübler, and J. P. Shaffer, "Atom-Based Vector Microwave Electrometry Using Rubidium Rydberg Atoms in a Vapor Cell," Phys. Rev. Lett. **111**, 063001 (2013).

3. J. A. Sedlacek, A. Schwettmann, H. Kübler, R. Löw, T. Pfau, and J. P. Shaffer, "Microwave electrometry with Rydberg atoms in a vapour cell using bright atomic resonances," Nat. Phys. **8**, 819-824 (2012).

2. A. Schwettmann, J. Sedlacek, and J. P. Shaffer, "FPGA-based locking circuit for external cavity diode laser frequency stabilization," Rev. Sci. Inst. **82**, 103103 (2011).

1. J. S. Cabral, J. M. Kondo, L. F. Gonçalves, V. A. Nascimento, L. G. Marcassa, D. Booth, J. Tallant, A. Schwettmann, K. R. Overstreet, J. Sedlacek and J. P. Shaffer, "Effects of electric fields on ultracold Rydberg atom interactions," J. Phys. B: At. Mol. Opt. Phys. **44**, 184007 (2011).

C.2 Presentations

Below is a list of the presentations that I have either presented or been co-author of the presentation.

16. J. Sedlacek, Y. Chao and J. P. Shaffer, ""Neutralization of Rb Surface Adsorbate Electric Fields by Slow Electron Attachment," DAMOP, Columbus, OH (2015). (Talk)
15. S. Kumar, J. Sheng, J. Sedlacek, H. Fan and J. P. Shaffer, "Interacting Rydberg atoms in an optical cavity to synthesize coherent collective states using dipole blockade," DAMOP, Columbus, OH (2015). (Talk)
14. J.Sheng, S. Kumar, J. Sedlacek and J. P. Shaffer, "Rydberg-blockaded medium inside a high-finesse optical cavity," DAMOP, Columbus, OH (2015). (Poster)
13. Y. Chao, J. Sedlacek and J. P. Shaffer, "Atom-surface studies with Rb Rydberg atoms," DAMOP, Columbus, OH (2015). (Poster)
12. J. Sedlacek and J. P. Shaffer, "Probing Atom-Surface Interactions Using Rb Rydberg Atoms," Second International Workshop on Ultracold Rydberg Physics, Recife, Brazil (2014). (Talk)
11. J. Sedlacek, H. Kübler, C. Ewel and J. P. Shaffer, "Probing Atom-Surface Interactions Using Rb Rydberg Atoms," DAMOP, Madison, WI (2014). (Talk)
10. H. Fan, S. Kumar, R. Dashner, H. Kübler, J. Sedlacek and J. P. Shaffer, "Quantum-Assisted Electrometry using Electromagnetically Induced Transparency with Rydberg Atoms in a Vapor Cell," DAMOP, Madison, WI (2014). (Poster)
9. S. Kumar, C. Ewel, J. Sedlacek and J. P. Shaffer, "Coherent manipulation by adiabatic passage of interacting Rydberg atoms inside a cavity," DAMOP, Madison, WI (2014). (Poster)

8. J. Sedlacek, H. Kübler, and J. P. Shaffer, "Vector Electrometry using Rydberg Atom Electromagnetically Induced Transparency," DAMOP, Quebec City, Canada (2013). (Talk)

7. J. Sedlacek, H. Fan, R. Daschner, C. Ewel, H. Kübler, and J.P. Shaffer "Using Rydberg Atom Electromagnetically Induced Transparency for Microwave Electrometry Applications," DAMOP Quebec City, Canada (2013). (Poster)

6. J. Sedlacek, A. Schwettmann, H. Kübler, and J. P. Shaffer, "Quantum Assisted Sensing Using Rydberg Atoms," FiO/LS, Rochester, NY (2012). (Talk)

5. J. Sedlacek, A. Schwettmann, H. Fan, and J. P. Shaffer, "Polarization Dependent Dark Resonances in Electromagnetically Induced Transparency with Rydberg Atoms," DAMOP, Anaheim, CA (2012). (Talk)

4. J. Sedlacek, A. Schwettmann, H. Fan, J. P. Shaffer, H. Kübler, and T. Pfau, "Quantum Assisted Sensing Using Rydberg Atom Electromagnetically Induced Transparency," DAMOP, Anaheim, CA (2012). (Poster)

3. J. Sedlacek, A. Schwettmann, and J. P. Shaffer, "Generation of 480nm cw light for Rydberg excitation of Rb," DAMOP, Atlanta, GA (2011). (Poster)

2. A. Schwettman, J. Sedlacek, C. Gentry, and J. P. Shaffer, "Probing RF electric fields with Rydberg atoms," DAMOP, Atlanta, GA (2011). (Talk)

1. A. Schwettmann, J. Sedlacek, L. Trafford, and J. P. Shaffer, "Atom-chip trap for Rydberg atom experiments," DAMOP, Houston, TX (2010). (Poster)